Spatio-temporal dynamics and disintegration of a fan liquid sheet

M. Broumand[a], A. Asgarian[a,b], M. Bussmann[a*], K. Chattopadhyay[a,b], and M. J. Thomson[a]

[a]Department of Mechanical and Industrial Engineering, University of Toronto, 5 King's College Road, M5S 3G8, Toronto, Ontario, Canada
[b]Department of Materials Science and Engineering, University of Toronto, 184 College Street, M5S 3E4, Toronto, Ontario, Canada

Abstract

The dynamic behaviour and disintegration mechanisms of a fan liquid sheet in a quiescent atmosphere are investigated over a broad range of differential injection pressures up to $\Delta p \approx 70$ bar through experiments, Proper Orthogonal Decomposition (POD) and spectral analyses, and linear stability analysis (LSA). By fan liquid sheet, we mean a diverging and attenuating liquid stream emanating from a flat fan nozzle with high velocity. High spatio-temporal resolution backlit images reveal the formation-growth-fragmentation process of bag-like structures along the fan liquid sheets, which we predict to be responsible for the overall breakup of the sheets through a mechanism known as 'wavy corridor'. Therefore, we propose a conjugate model based on LSA to take into account the role of different shear and surface tension driven instabilities in defining the liquid sheet intact radius and primary droplet sizes. The predictions of LSA from the dynamic features of the liquid sheets, which mainly depend on the sheet Weber number (We), are consistent with the quantitative results obtained from the POD and spectral analyses of the images. While the Strouhal number (St) and the intact radius (R) of the fan liquid sheets reduce like $We^{-1/3}$ with increasing We, the volume median diameter of primary droplets decreases like $We^{-11/12}$. An Image Feature Consolidation Technique (IFCT) along with a machine-learning technique, Receiver Operating Characteristic (ROC) curve analysis, was used to estimate the mean diameter of spray droplets with a large range of sizes.

*Corresponding author; E-mail addresses: bussmann@mie.utoronto.ca

1. Introduction

Dispersed droplets in a spray are commonly generated by the disintegration of a cohesive liquid sheet or jet when disrupting forces overwhelm consolidating ones, which is called atomization [1]–[3]. When a liquid stream is pressurized through a flat fan nozzle, it emerges into a quiescent atmosphere in a topological shape of a diverging flat sheet whose thickness attenuates to satisfy continuity. At a sufficiently high injection pressure or sheet velocity, the attenuating liquid sheet becomes unstable and begins to flap like a flag with relatively high intensity in the downstream regions far from the nozzle exit [4], [5]. The attenuating flapping liquid sheet then disintegrates into ligaments and droplets, with a size distribution correlated to the instability wavelengths of the sheet [6], that largely depend on nozzle design, liquid properties, and test/operating conditions [7], [8].

While the liquid sheet atomization mechanism has been successfully exploited in, for example, splash plate and impinging jet nozzles for generating flat-shaped sprays, and in pressure-swirl and prefilming air-blast nozzles for making conical spray patterns, the focus of the present study is on flat fan sprays. This is motivated by the simple experimental setup and the small number of controlling parameters involved in generating fan liquid sheets, where the evolution from sheet to ligaments and droplets can be easily explored and extended to the other types of nozzles that exploit the sheet atomization mechanism. A detailed study on fan liquid sheets is also important for practical applications including the atomization of molten metal into droplets (e.g. [9]–[11]), the agricultural spraying of pesticides (e.g. [12], [13]), and the injection of fuel into small-scale annular combustors (e.g. [1], [14]).

Fan sprays were widely investigated in the mid-twentieth century by Dombrowski and co-workers in several theoretical and experimental (photographic) studies [15]–[17]. They correlated the fan liquid sheet undulations to the relative velocity with the surrounding atmosphere using the theoretical analysis based on a shear-driven (Kelvin–Helmholtz (KH) type [18]) instability developed by Squire [19], York et al. [20], and Hagerty and Shea [21]. The most unstable/amplified wave was then assumed to break up the

sheet at half wavelength intervals into ligaments parallel to the free edge of the sheet and droplets subsequently resulted from the disintegration of these ligaments, similar to the early analysis of Weber on the breakup of round liquid jets [5]. Similar spanwise ligaments parallel to the sheet free edge were later observed in the context of air-blast liquid sheets when disintegrating in the so-called 'cellular' breakup regime, see e.g., [22], [23].

More physical phenomena were later incorporated into the classical stability analyses on a liquid sheet, see e.g. [24]–[26]. Dombrowski and Johns [27] included liquid viscosity and sheet thickness in their theoretical study. Crapper et al. [28] performed a spatial stability analysis on Newtonian and non-Newtonian liquid sheets by accounting for the viscosity of both liquid and gas phases. Li and Tankin [29] conducted a temporal instability analysis on a viscous liquid sheet in an inviscid gas and proposed a viscosity-enhanced instability mode in addition to the shear-driven instabilities. Kooij et al. [30] and Majumdar and Tirumkudulu [31] then studied the effects of the thickness of a liquid sheet, spraying parameters and liquid properties on its instabilities, breakup, and subsequent droplet size distributions. These studies were expanded by Senecal et al. [32], Deshpande et al. [33], and Zandian et al. [34] to model the instabilities and breakup of liquid sheets via numerical simulations. Most recently, direct numerical simulation along with stability analysis were used to perform detailed studies of the dynamics of low- and high-speed liquid sheets [35]–[38]. The stability analyses on a liquid sheet in a quiescent atmosphere were also extended to air-blast liquid sheets by taking into account the controlling effects of gas vorticity layer thickness on the sheet undulations through theoretical studies, see e.g. [39]–[41], and numerical simulations, see e.g. [42], [43].

Another common method for generating a liquid sheet spray is the impingement of a liquid jet on a solid surface (e.g., [44]–[46]) or on a similar jet (e.g., [47]–[49]), inspired by the pioneering studies of Savart [50]. Villermaux and Clanet [51] performed a systematic investigation on the droplet formation

process from a flapping liquid sheet formed by the impact of a round liquid jet on a flat disc. They reported that the shear (KH) instability gave the liquid sheet a flapping motion (similar to fan liquid sheets) which then triggered a Rayleigh-Taylor (RT) instability (Rayleigh [52] and Taylor [53]) and subsequently generated indentations at the sheet free edge. As a result, ligaments emerged perpendicularly from the edge, similar to the so-called 'stretched streamwise ligament' breakup regime observed in air-blast liquid sheets (e.g., [22], [23]), and ultimately disintegrated into droplets. However, the observed streamwise ligaments differ from the spanwise ligaments of the fan liquid sheets observed by Dombrowski and co-workers, see e.g. Fraser et. al. [16].

The present study aims at advancing the long-standing experimental and theoretical studies on fan sprays. In support of Rayleigh's pure speculation on the applications of photography in science [54], enhancements in optical systems allowed us to observe (through the backlight imaging technique) the formation-growth-fragmentation process of bag-like structures along a liquid sheet in a quiescent atmosphere which we purport to be responsible for the overall sheet breakup through a mechanism known as 'wavy corridor' [8]. Furthermore, while (similar to Fraser et. al. [16] and Kooij et al. [30]) the present experiments show that the ligaments disintegrate parallel to the sheet free edge originated from KH-type instabilities, we also observe spanwise RT-type instabilities on the sheet (through studying the sprays at injection pressures beyond the range considered by [16] and [30]) which support the findings of Villermaux and Clanet [51]. To elucidate these phenomena, an approach based on linear stability analysis (LSA) considering both KH-type and RT-type instabilities, Proper Orthogonal Decomposition (POD) analysis, and spectral analysis is followed in the present study, which was not used in the above-mentioned studies. As a result, we propose a conjugate model based on both KH-type and RT-type instabilities to predict the fan liquid sheet characteristics including the intact radius and primary droplet sizes.

In order to quantify our observations and compare them with the results of LSA, we apply a POD analysis along with a spectral analysis to the high-speed images acquired in the present experiments. This analysis helps to identify the most amplified waves of the liquid sheets, as well as quantitatively determine the corresponding dynamic features such as amplitude, wavelength, and frequency. POD is an optimal statistical method for describing multi-dimensional datasets with a reduced number of dimensions [55]. In the context of fluid mechanics, applying POD to a turbulent velocity (i.e., vector) field for the identification of the dominant orthogonal modes (or coherent structures) is well established [56], [57]. There also exist some other methods for the analysis of such datasets, such as Dynamic Mode Decomposition (DMD) [58] and Spectral Proper Orthogonal Decomposition (SPOD) [59], [60] techniques. Interestingly, POD has been recently applied to a scalar field (i.e., pixel intensity/illumination of images) for the characterization of undulating liquid streams. Arienti and Soteriou [61] and Herrmann et al. [62] applied POD to their, respectively, experimental and numerical results along with an analysis in the frequency domain to study the dynamics of a transverse liquid jet. A similar approach was later employed by Broumand et al. [63] to study the dynamic evolution of a liquid jet in a turbulent cross-airflow and by Charalampous et al. [64], [65] and Kumar and Sahu [66] for the dynamic characterization of a liquid jet in a co-axial airflow. POD was also used for the morphological analysis of a conical liquid sheet injected form a pressure-swirl nozzle (see e.g., [67], [68]).

In the following, the experimental methodology followed by the flow parameters and test conditions adopted in the present study are introduced in Section 2. The nature of fan liquid sheet instabilities and the mechanisms involved in its disintegration are phenomenologically studied in Section 3, and the analyzing approach used for the identification of the specific POD modes representing the liquid sheet spatio-temporal dynamics is elucidated. Section 4 is devoted to the presentation of our proposed conjugate model based on LSA, where the theoretical results associated with the features of fan liquid sheets are

compared with experiment results. A summary of major findings and conclusions is provided in Section 5.

2. Experimental methodology

2.1. Apparatus and diagnostics

The main components of the experimental apparatus consist of a high-pressure spraying system and a backlight imaging system (Figure 1a). The spraying system includes a high-pressure pump, a tank, a nozzle, and associated piping and instrumentation. The nozzle is mounted at the top center of the tank to spray vertically downward. The test liquid is tap water at room temperature, pressurized by means of a positive displacement plunger pump. Such pumps operate at a fixed flowrate regardless of the discharge pressure. A needle valve is installed upstream of the nozzle to control the flow through the nozzle, and the pump discharge is equipped with an unloader valve to divert excess water flow into the tank. This provides flexibility in spraying at different flowrates/pressures. The nozzle (1/4 MEG 2504) belongs to a family of fan atomizers produced by Spraying Systems Co., see Figure 1b and 1c. The orifice geometry of the nozzle corresponds to the intersection of a transverse curved slit and a semi-ellipsoidal end of the internal passage, resulting in an oval-shaped orifice with large and small diameters of 1.77 mm and 0.97 mm, respectively.

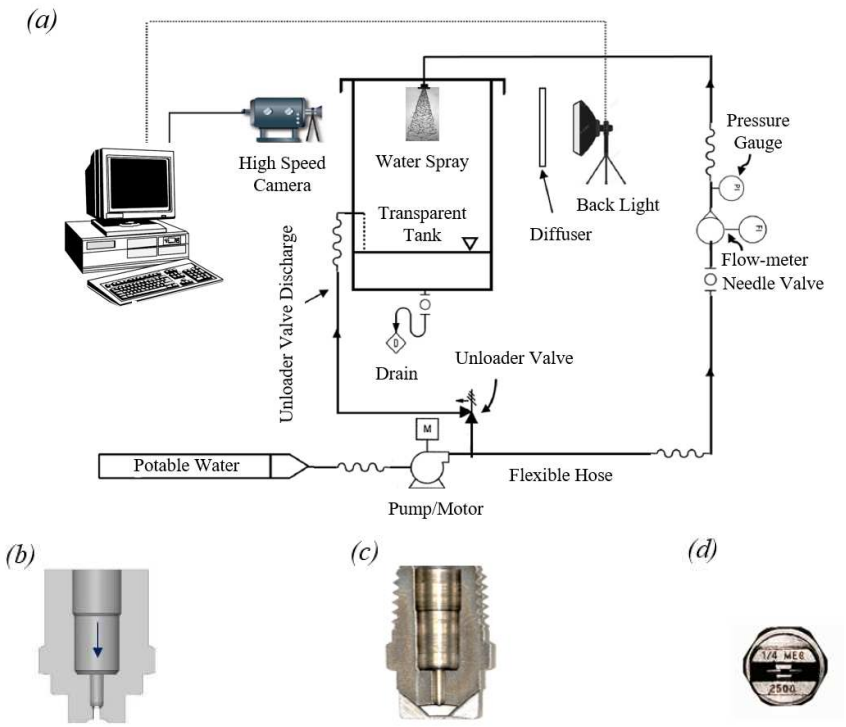

FIGURE 1. Schematic diagram of **(a)** the experimental spray test set-up and the arrangement of backlighting technique for visualization and **(b)** nozzle flow direction, along with real images of the **(c)** nozzle cross section parallel to its slit and **(d)** nozzle exit with dimensions of 0.97 mm×1.77 mm.

The optical system for the imaging consists of a high-speed camera with a high precision lens, and a back light and a diffuser which are located on opposite sides of the spray. The exposure time of the camera was set fast enough to freeze ligaments/droplets with no blurring, with a satisfactory background brightness level. For the images to be used in POD analysis, the optical system was operated at the highest frame rates of the camera in order to resolve the sheet spatio-temporal features up to the highest injection pressures of the experiments. As a result, the images acquired for the POD analysis are of lower spatial resolution than those of the spray sizing experiments, which is somehow favorable for reducing the POD analysis costs. In the spray sizing experiments, on the other hand, a high spatial resolution optic is

necessary for resolving the small diameter droplets within the sprays. Therefore, two optics with different depths of field and resolutions were employed for measuring the large range of size of the droplets within the fan sprays at different injection pressures. More information on the optical setups can be found in Table 1.

TABLE 1. Optical setups specifications

	POD analysis		**Spray Sizing**	
Point of View, POV	Side-view	Front-view	Front-view	Front-view
Camera Model and Specifications	Phantom Miro LAB 320 by Vision Research: 1,380 fps at 1920 × 1200			Drop Sizer: a commercial spray imaging system with a high-resolution micro-lens by Mazlite (http:// www.mazlite.com/)
Lens Model and Specifications	Milvus 2/100M by ZEISS: Aperture range: f/2.0 – f/22 Focusing range: 0.44 - ∞ (m)			-
Working Distance (mm)	850	850	440	62
Depth of Field (μm)	26650	26650	6250	900
Resolution (μm/pixel)	68.5	66.7	19.8	2.4
Aperture	f/19	f/19	f/19	f/11
Field of View, FOV (pixel × pixel)	768 × 240	768 × 480	1152 × 1152	3088 × 2076
Camera Frame Rate, f_s (fps)	10000	7391	2000	58
Camera Exposure Time (μs)	1	1	1	0.05[a]
Number of Images, N	400	400	200	200

[a] Back-light flash time

2.2. Flow parameters and test conditions

There exist several non-dimensional parameters which are important for defining the dynamic behaviour and disintegration mechanisms of a fan liquid sheet: the Reynolds number, $Re = \rho u h/\mu$, Weber number, $We = \rho u^2 h/\sigma$, and Ohnesorge number, $Oh = \mu/(\rho h \sigma)^{1/2}$. In these parameters, $\rho = 1000$ kg m^{-3}, $\mu = 1 \times 10^{-3}$ Pa s, and $\sigma = 72 \times 10^{-3}$ N m^{-1} are the density, dynamic viscosity, and surface tension of water, respectively, and u is the liquid sheet velocity. $2h$ is the liquid sheet thickness; its value at the nozzle exit, $2h_0 = 0.69 \pm 0.02$ mm, is estimated from side-view images [Figure 2

(Multimedia view)]. The surrounding air density is $\rho_a = 1.2$ kg m^{-3}. Table 2 lists the range of these parameters in the present experiments.

TABLE 2. Experimental test conditions

Case	Injection Pressure, Δp (bar)	Sheet exit velocity, u_0 (m/s) [a]	Reynolds number based on u_0 (Re)	Weber number based on u_0 (We)	Ohnesorge number (Oh) [b]
1	2.1	18.7	6444	1677	0.0063
2	2.8	21.6	7441	2236	0.0063
3	4.8	28.6	9843	3912	0.0063
4	6.9	34.1	11765	5589	0.0063
5	20.7	59.1	20377	16767	0.0063
6	34.5	76.3	26307	27945	0.0063
7	51.7	93.5	32220	41917	0.0063
8	68.9	107.9	37204	55889	0.0063

[a] Liquid sheet mean velocity at the nozzle exit is estimated based on $u_0 = 1.3\sqrt{\Delta p(\text{kPa})}$ from [69]
[b] Viscous forces do not inhibit breakup as $Oh \sim 10^{-3}$

3. Liquid sheet disintegration: phenomenology

3.1. Observations

High-speed images of the test cases in Table 2 are qualitatively compared in order to elucidate the effect of the injection pressure on the dynamical behavior and disintegration mechanisms of a fan liquid sheet injected into a quiescent atmosphere. At low injection pressures (or We), in agreement with the literature, longitudinal shear-induced (KH-type) waves which grow in amplitude with distance from the nozzle exit are evident from the side-view images [Figure 2a (Multimedia view)]. The crests and troughs of these longitudinal undulations are also recognizable from the dark and bright regions on the sheet front-view, see Figure 2c (Multimedia view). When the liquid travels through the longitudinal waves, it is periodically accelerated upwards and downwards perpendicular to the sheet plane, initiating a secondary (RT-type) instability responsible for the spanwise corrugations of the sheet. This mechanism, which is known as 'wavy corridor' [8], plays an important role in the breakup of air-blast liquid jets [70] and undulating Savart liquid sheets [71]. An example of the sheet transverse waves is illustrated in Figure 2c (Multimedia view). Fan liquid sheets generate two distinct types of ligaments which are trackable from

the front-view images, see e.g. Figure 2c (Multimedia view). The first one is a sheet ligament which disintegrates parallel to the sheet free edge with corrugations similar to the upstream disturbances. The other one is a rim ligament formed along the two diverging sides of the sheet, where disintegration results in large droplets of different size from those of the sheet ligament [72]. The characteristics of the rim ligaments have been studied by Bush and Hasha [48], and Bremond and Villermaux [49] for a sheet produced by impinging liquid jets.

At higher injection pressures, these instabilities and ligaments appear much earlier on the liquid sheets [Figure 2b and 2d (Multimedia view)], but are less perceptible because of, first, a decrease in the spatio-temporal scales of the sheet features with increasing We, and second, the blockage effects of the small-size droplets generated through surface stripping. The formation mechanism of such surface droplets [Figure 2b (Multimedia view)], the onset of which moves toward the nozzle exit with increasing injection pressure, has been widely investigated in the context of liquid sheets and mixing layers (e.g., [73]–[75]) and air-blast liquid jets (e.g., [70], [76]).

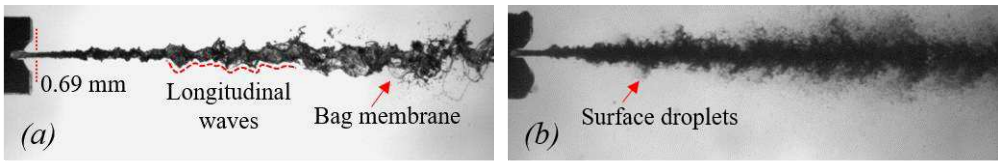

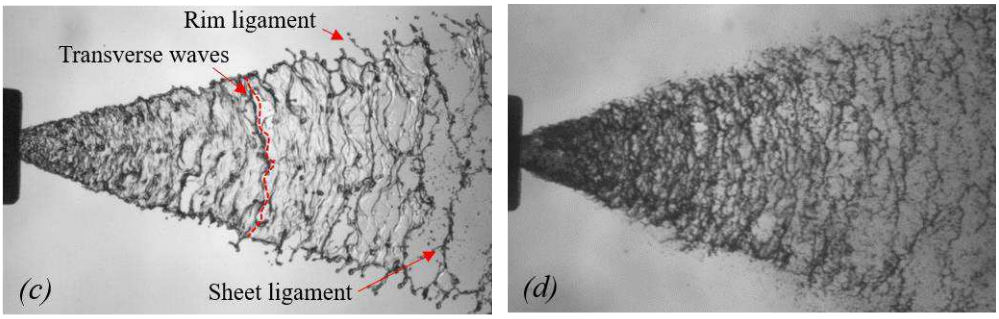

FIGURE 2. Instantaneous images of the fan liquid sheets injected at $\Delta p = 4.8$ bar (case No. 3) **(a)** side-view and **(c)** front-view, and injected at $\Delta p = 51.7$ bar (case No. 7) **(b)** side-view and **(d)** front-view. The features of the fan liquid sheets are identified by red arrows. (Multimedia view)

Side-view images also reveal the presence of bag membranes along the liquid sheet which are more recognizable at low injection pressures, since the formed bags have enough time to grow and the spray shrouding the sheet is dilute [Figure 2a (Multimedia view)]. These travelling bags originate from the spanwise modulation of the liquid sheet thickness caused by the transverse (RT-type) instabilities. With distance from the nozzle, the thickness modulations grow with amplification of RT instability because of an increase in the acceleration induced by longitudinal waves (see Section 4.1). The bag membranes ultimately burst into very small droplets with a mechanism similar to the bursting of a thin liquid film [77], which is also observed in the secondary bag breakup of a droplet (e.g., [78], [79]), the membrane breakup regime in an air-blast liquid jet (e.g., [80], [81]), and the bag breakup regime in a transverse liquid jet (e.g., [82]–[85]). As a result, perforations form downstream within the liquid sheet, which subsequently break the sheet into spanwise ligaments because of their expansion (by capillary recession) and coalescence. This process is observable from the sheet front-view images, e.g., Figure 2c and 2d (Multimedia view). The formation-growth-fragmentation process of one of these bags along the liquid sheet is shown in Figure 3 (Multimedia view).

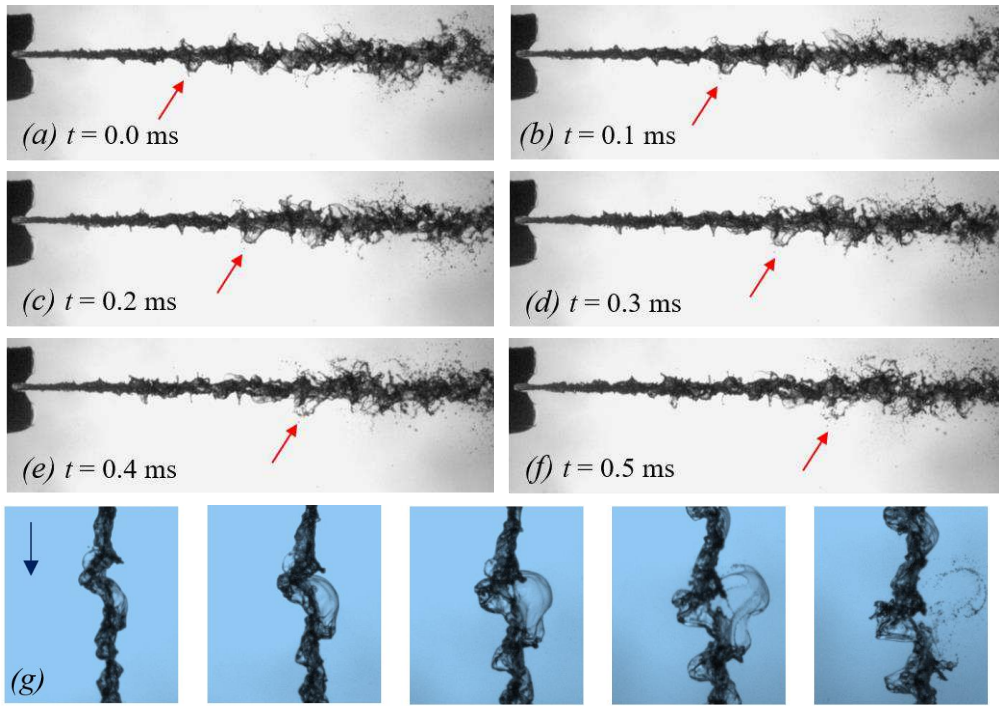

FIGURE 3. (a-f) Formation-growth-fragmentation process of a bag (identified by red arrows) travelling along the fan liquid sheet injected at $\Delta p = 6.9$ bar (case No. 4), and **(g)** magnified views of a bag at $\Delta p = 2.8$ bar (case No. 2) and 200 μs per frame. The blue arrow in **(g)** indicates the liquid sheet flow direction. (Multimedia view)

In these experiments, however, not all the sheet perforations are observed close to the overall sheet breakup location (i.e., far from the nozzle exit). We observe the arbitrary nucleation of some early holes which expand further with travelling along the liquid sheets, see e.g. Figure 4 (Multimedia view). Previous studies on a single-phase liquid sheet (e.g., [16], [69]), an emulsion-based liquid sheet (e.g., [86], [87]), and a bubbly two-phase liquid sheet [88] suggest that the growing rate of the hole radius is correlated with the Taylor-Culick velocity ([89], [90]). The formation mechanism of such near-nozzle perforations in a liquid sheet is still not well understood, particularly for homogenous ones [91]. For example, Fraser et al. [16] observed holes in a water liquid sheet under vacuum conditions (i.e., a smooth fan liquid sheet) and

proposed possible mechanisms including the release of in-nozzle bubbles (from dissolved gas or cavitation), the arbitrary impingement of droplets (generated by nozzle imperfections or surrounding recirculated droplets) on the sheet surface, and upstream noise (from an imperfect nozzle or nozzle vibrations).

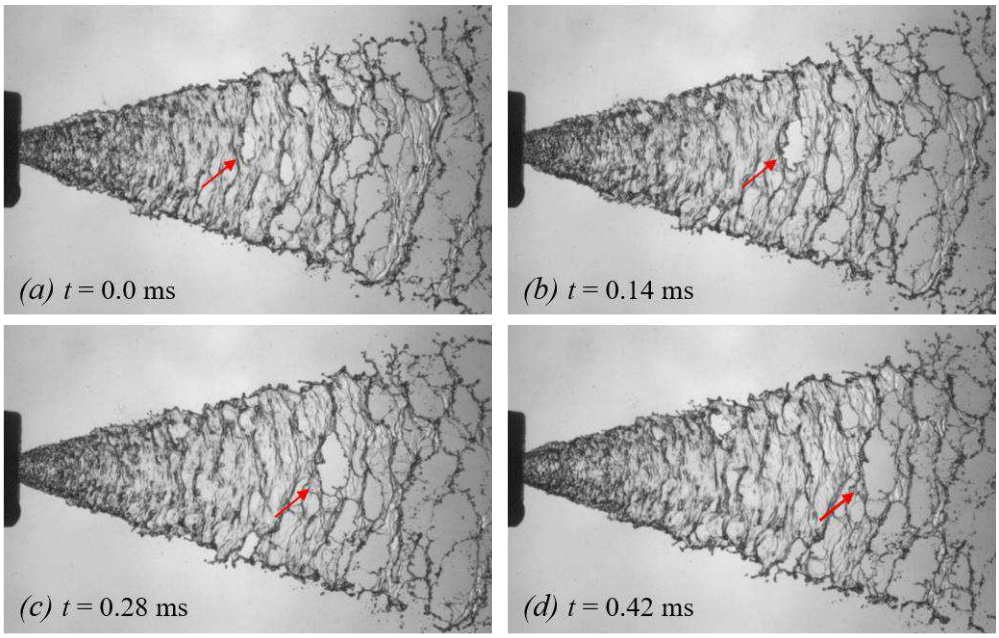

FIGURE 4. (a-d) Expansion of a perforation (identified by red arrows) as travelling along the fan liquid sheet injected at $\Delta p = 6.9$ bar (case No. 4). (Multimedia view)

3.2. Liquid sheet dynamics

A POD analysis along with an analysis in the frequency domain was applied to both the side- and front-view series of high-speed images of the test cases in Table 2, to identify the spatially evolving coherent structures on a liquid sheet, as well as quantitatively determine the corresponding spatio-temporal features. In the present study, POD was applied to a dataset of N images with a field of view of $m \times n$ pixels (see Table 1). Using an in-house MATLAB code, the information in each pixel was translated to a grey scale intensity (from 0 to 255), assembled into a column vector for each instantaneous image, and

the vectors assembled into a single matrix of size $mn \times N$ for all time steps. The so-called 'snapshot POD' proposed by Sirovich [57] was then used for the orthogonal decomposition of the obtained matrix based on a Singular Value Decomposition (SVD) technique [92]. A description of the algorithm can be found in Meyer et al. [93]. As a result, the orthonormal basis functions (spatial modes) ϕ_r and time-dependent orthonormal amplitude coefficients (temporal coefficients) $a_{r,i}$ are extracted so that a reconstructed image with the first $M \leq N$ modes at time t_i, $i = 1,2,\dots,N$, using Eq. (1), is optimal when the least squares truncation error is minimized.

$$Z_i = \sum_{r=0}^{M} a_{r,i}\phi_r \tag{1}$$

The dynamic correlation of the spatial modes is quantified with an analysis in the frequency domain by calculating the power spectral density (PSD) and cross-power spectral density (CPSD) of the POD temporal coefficients using Eqs. (2a) and (2b) [94].

$$\mathrm{PSD} = \frac{1}{N}\left|\sum_{i=0}^{N-1} a_i \exp\left(-j\frac{2\pi f_s i}{N}\right)\right|^2 \tag{2a}$$

$$\mathrm{CPSD} = \frac{1}{N}\sum_{i=0}^{N-1} a_i b_i \exp\left(-j\frac{2\pi f_s i}{N}\right) \tag{2b}$$

where $j^2 = -1$, a and b are temporal coefficinets, and f_s is the sampling frequency of the images (see camera frame rate in Table 1).

From a physical point of view, POD decouples the large flow structures from small ones so that the first (most energetic) modes represent the mean flow, followed by modes that correspond to the coherent structures of the flow. Finally, there exist higher-order modes with distributed patterns, with temporal coefficients that appear as noise in the frequency domain. As demonstrated by Rempfer and Fasel [95], two modes of similar energy can show identical, but shifted, spatio-temporal features. Arienti and Soteriou

[61] later elucidated that a traveling wave on a liquid jet is a superposition of two standing waves (or two orthogonal modes) with half a wavelength delay, with temporal coefficients approximately periodic at the same frequency with a phase difference of ±90 deg. Accordingly, to identify the first pair of such coupled modes describing the most amplified waves of a liquid sheet, the following approach was adopted in the present study.

a) Search for two modes with almost identical temporal characteristics (PSD) starting from the first mode,
b) confirm the CPSD amplitude of the two modes peaks where the CPSD phase is near ±90°,
c) inspect if the spatial structures of the two modes display a similar pattern with half a wavelength delay, and
d) check whether the reconstructed sheet image using the two modes at a specific time step is sufficient to describe the spatial coherent structures of the original sheet image at the same time step.

Following these steps, we were able to find the first coupled modes within the first 20 modes of each dataset, where the orders (indices) of the selected modes shifted to larger numbers for a sheet with smaller spatio-temporal scales, as when injected at a higher pressure. In all the analyses, as expected, the first spatial mode always exhibited the bulk motion of the sheet with no undulations, representing the average side- and front-angle of the fan spray.

3.2.1. Side-view wave characteristics

Figure 5 shows the results obtained from the side-view analysis of case No. 3 in Table 2. In this case, the second and third POD modes are the first coupled ones. The consecutive positive and negative regions in their spatial modes (ϕ_2 and ϕ_3), shown by the blue and red patches in Figure 5a, indicate a sinusoidal behaviour with half a wavelength difference. The dimensions of these structures progressively grow until reaching a plateau at a specific distance from the nozzle, which is attributed to the saturation of instability

growth in an attenuating liquid sheet [51], [71]. The image obtained from the reconstruction of these two coupled modes, $a_2(i)\phi_2 + a_3(i)\phi_3$, at a specific time step (i =100), as well as the original image of the liquid sheet at the same time step are depicted in Figure 5b for comparison. The identical PSDs of the temporal coefficients of these two coupled modes, a_2 and a_3, are shown in Figure 5c. Their corresponding CPSD amplitude also has a strong maximum at a frequency of 3.733 kHz (Figure 5d), where the CPSD phase difference is about +90° (Figure 5e).

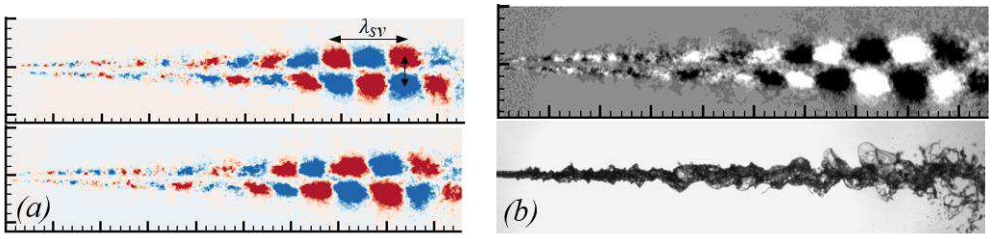

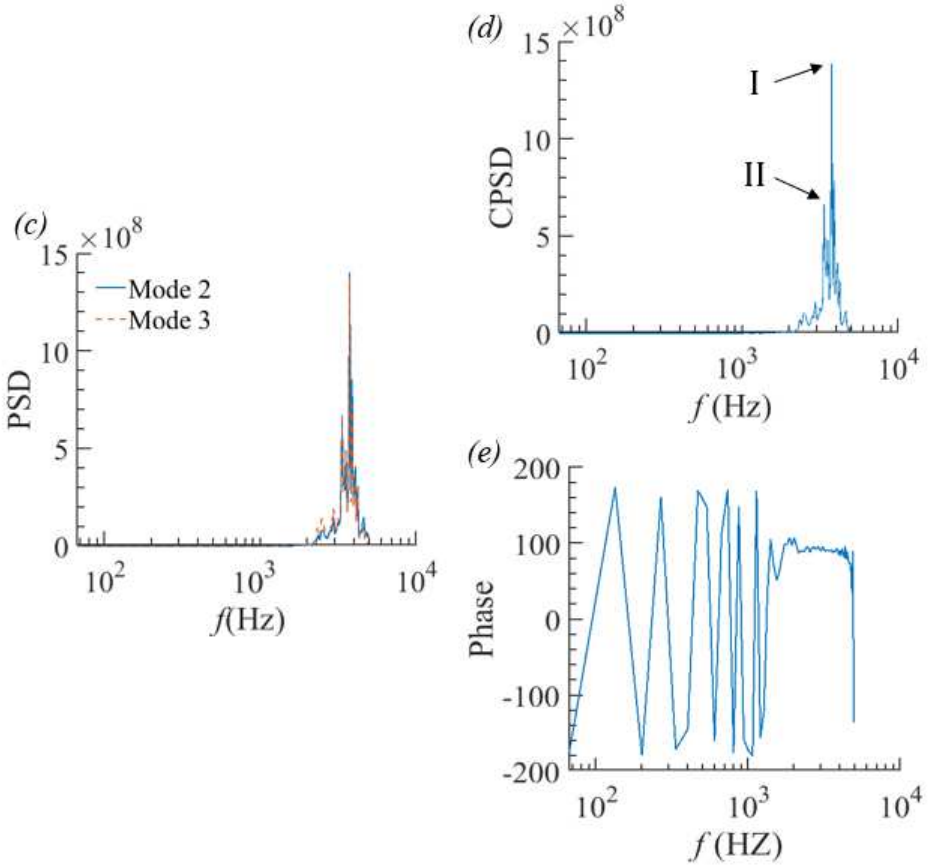

FIGURE 5. POD analysis of the side-view images of case No. 3; **(a)** the first coupled spatial modes (ϕ_2 and ϕ_3), **(b)** a comparison of the reconstruction of ϕ_2 and ϕ_3 and the original image of the liquid sheet at t_i =100, **(c)** a comparison of the PSDs of the temporal coefficients of the two coupled modes (a_2 and a_3), **(d)** CPSD amplitude of a_2 and a_3, and **(e)** CPSD phase of a_2 and a_3. The numerical value of the colormap in **(a)** and **(b)** is normalized by the respective maximum value to fit the scale range from −1 to 1. The arrows in **(d)** show the first and second non-harmonic peak in the CPSD diagram.

Applying the same approach to the side-view waves of a sheet injected at a higher injection pressure results in the same dynamic behaviour as case No. 3 (Figure 5), albeit partially hidden by the surface droplets. For example, Figure 6 shows the results obtained from the analysis of case No. 7 in Table 2.

While the sinusoidal structures observed in this case are barely recognizable from the POD spatial modes (Figure 6a), it is still possible to find the first coupled modes of the sheet by performing a spectral analysis on the POD temporal coefficients. The PSDs of the first two coupled modes at this condition, a_5 and a_8, are noisier and broader (Figure 6c) compared to those of case No. 3 (Figure 5c). The corresponding CPSD amplitude peaks at 3.516 kHz (Figure 6d) where the CPSD phase difference is about -90° (Figure 6e). Similar to case No. 3, an instability growth is also observable in the spatial modes of this case, ϕ_5 and ϕ_8 (Figure 6a), though it reaches the saturation condition much closer to the nozzle exit. The reconstructed image of these two coupled modes, $a_5(100)\phi_5 + a_8(100)\phi_8$, and the original image of the liquid sheet at the same time step (t_i =100), are shown in Figure 6b.

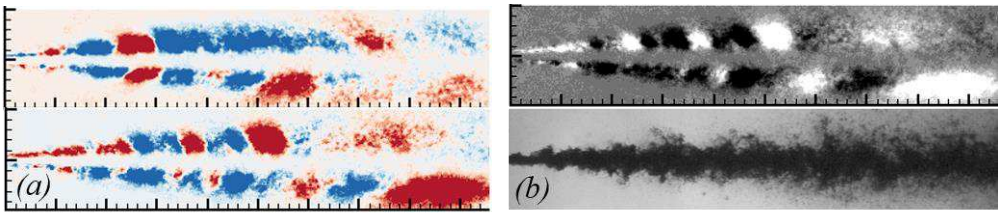

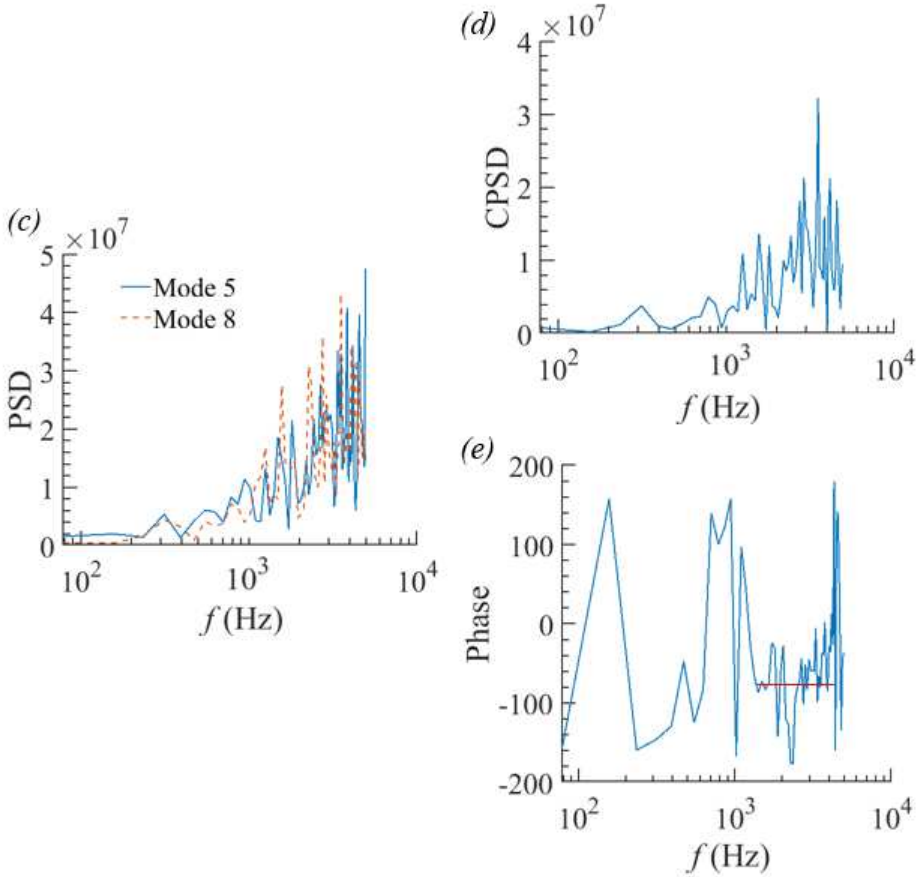

FIGURE 6. POD analysis of the side-view images of case No. 7; **(a)** the first coupled spatial modes (ϕ_5 and ϕ_8), **(b)** a comparison of the reconstruction of ϕ_5 and ϕ_8 and the original image of the liquid sheet at t_i =100, **(c)** a comparison of the PSDs of the temporal coefficients of the two coupled modes (a_5 and a_8), **(d)** CPSD amplitude of a_5 and a_8, and **(e)** CPSD phase of a_5 and a_8. The numerical value of the colormap in **(a)** and **(b)** is normalized by the respective maximum value to fit the scale range from −1 to 1. The red solid line in **(e)** highlight the frequencies in which the CPSD phase difference is about -90°.

The peak observed in the CPSD amplitude diagram of the side-view images is correlated to the dominant frequency of the most amplified waves, f_{sv}, along the liquid sheet. In addition, as shown in Figure 5a, the vertical distance between the centers of the sheet structures and the horizontal distance

between consecutive positive peaks (or negative peaks) correspond to the amplitude, ξ, and side-view wavelength, λ_{sv}, of the most amplified waves along the liquid sheet, respectively. As can be seen from Figures 5a and 6a, the spatial coherent structures along a liquid sheet become less perceptible at a certain distance from the nozzle (after reaching the saturation condition). This distance is tentatively linked to the liquid sheet intact radius (R), which we later confirmed from direct observations of the front-view images. These features obtained by the analysis of the side-view images at all test conditions (Table 2) are listed in Table 3.

TABLE 3. Liquid sheet characteristics obtained from the side-view wave analysis

Case	f_{sv} (kHz)	λ_{sv} (mm) [a]	ξ (mm) [a]	R (mm)
1	2.266	6.5	1.8	56
2	2.344	7.2	2.3	51
3	3.733	7.0	2.5	45
4	3.203	7.5	2.6	38
5	3.828	7.6	3.0	28
6	3.125	6.2	2.9	25
7	3.516	5.6	3.1	21
8	3.125	4.1	3.1	18

[a] λ_{sv} and ξ are the averaged values estimated at the region close to R

3.2.2. Front-view wave characteristics

Unlike the side-view images, the front-view datasets are not hidden beneath the surface droplets at high injection pressures. For example, Figure 7 shows the results obtained from the front-view analysis of case No. 4 in Table 2. In this case, the sixth and seventh modes are the first coupled ones, as shown in Figure 7a. The image obtained from the reconstruction of these two coupled modes, $a_6(100)\phi_6 + a_7(100)\phi_7$, as well as the original image of the liquid sheet at the same time step (t_i =100), are depicted in Figure 7b. Figure 7c shows the almost identical PSDs of the temporal coefficients of these two coupled modes. The corresponding CPSD amplitude has a peak at 2.656 kHz (Figure 7d) where the CPSD phase difference is about +90° (Figure 7e).

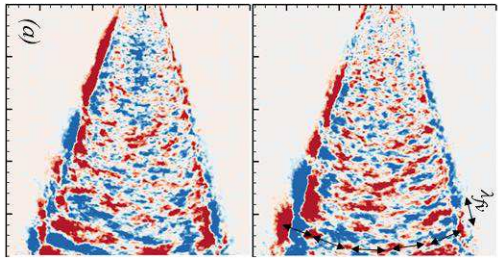

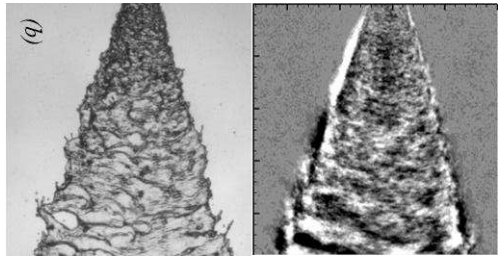

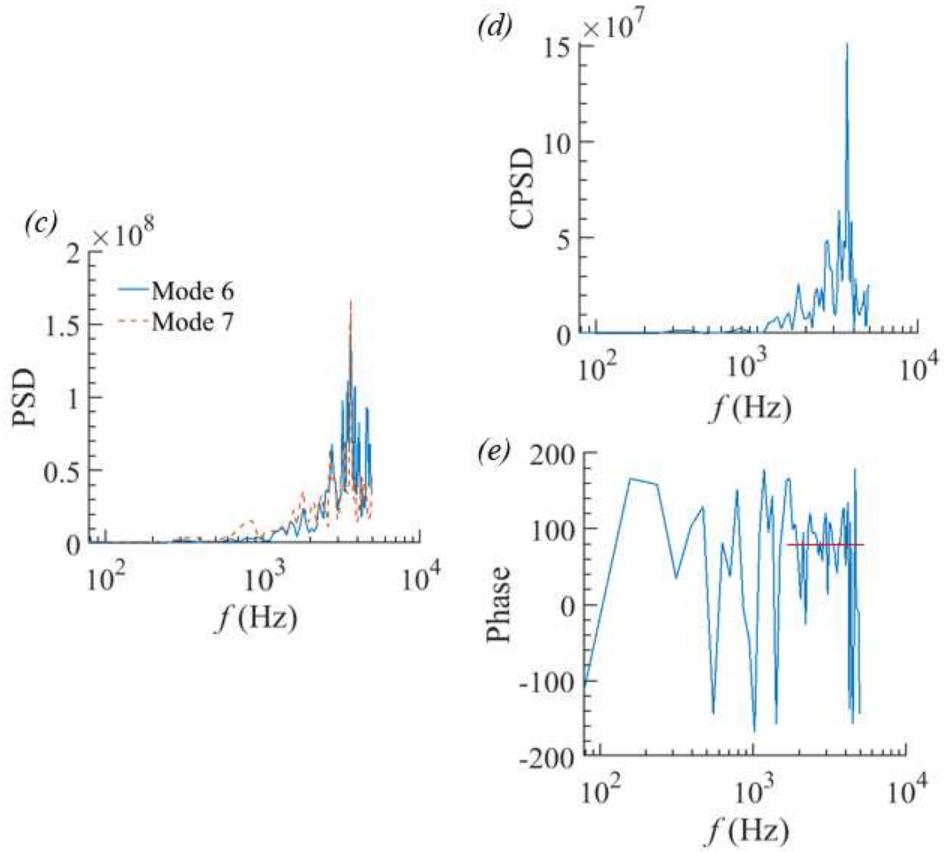

FIGURE 7. POD analysis of the front-view images of case No. 4; **(a)** the first coupled spatial modes (ϕ_6 and ϕ_7), **(b)** a comparison of the reconstruction of ϕ_6 and ϕ_7 and the original image of the liquid sheet at t_i =100, **(c)** a comparison of the PSDs of the temporal coefficients of the two coupled modes (a_6 and a_7), **(d)** CPSD amplitude of a_6 and a_7, and **(e)** CPSD phase of a_6 and a_7. The numerical value of the colormap in **(a)** and **(b)** is normalized by the respective maximum value to fit the scale range from −1 to 1. The red solid line in **(e)** highlight the frequencies in which the CPSD phase difference is about +90°.

The peak identified in the sheet CPSD amplitude diagram in this section is correlated to the dominant frequency of the most amplified waves observable on the sheet front-view, f_{fv}. As is evident from Figure 7a, in addition to the streamwise consecutive positive and negative regions (indicating the longitudinal

waves previously observed in the side-view images), there exist spanwise structures with similar patterns which represent the transverse waves [see Figure 2c (Multimedia view)]. The streamwise and spanwise distances between the consecutive positive peaks (or negative peaks) correspond to the front-view wavelength, λ_{fv}, and transverse wavelength, $\lambda_{\perp}$, respectively, of the most amplified waves observable on the sheet front-view. It should be emphasized that the nature of λ_{fv} and λ_{sv} are the same and both represent longitudinal waves, but from two different point of views. Comparing Tables 3 and 4, it is clear that $\lambda_{fv} \approx 0.5\lambda_{sv}$. This is because, in the front-view images, each of the crests and troughs of the waves produce one dark (or high intensity) region, whereas, in the side-view images, the region between two troughs (which also includes one crest) represents a single dark region. The features obtained by the analyses of the front-view images at all test conditions (Table 2) are listed in Table 4.

TABLE 4. Liquid sheet characteristics obtained from the front-view wave analysis

Case	f_{fv} (kHz)	λ_{fv} (mm) [a]	$\lambda_{\perp}$ (mm) [a]
1	1.617	3.6	6.1
2	2.079	3.2	5.4
3	3.060	3.1	2.8
4	2.656	3.3	3.4
5	2.541	3.8	2.4
6	3.233	3.4	2.3
7	2.252	3.0	2.0
8	2.541	2.1	1.6

[a] λ_{fv} and $\lambda_{\perp}$ are the averaged values estimated at the region close to *R*

Overall, both the side- and front-view frequencies of the sheets in the present study exhibit similar trends with increasing injection pressure, albeit with slightly smaller values for the latter. Figure 8a shows a plot of f_{sv} (solid circles) and f_{fv} (solid squares) as a function of the sheet exit velocity, u_0 (Table 2). It can be observed that the frequency initially increases and then fluctuates around a constant value with increasing u_0. This is consistent with a study on the longitudinal instabilities in an air-blast liquid sheet by Lozano et al. [96], who reported that at a fixed velocity of co-flowing air, the liquid sheet frequency is independent of the sheet velocity. The dimensionless presentation of the parameters in Figure 8a is shown

in Figure 8b by using We and Strouhal number, $St = fh/u$, calculated based on f_{sv} or f_{fv}, the sheet exit velocity, u_0, and exit thickness, h_0. With increasing We, St decreases like $We^{-1/3}$ and approaches St~0.01, which is close to the value observed for an air-blast liquid sheet in the experiments of Lozano et al. [96]. However, analogous to other flows in fluid dynamics, such as vortex shedding behind a solid cylinder for which St~0.2 [97], this value is much smaller because of the flexible nature of a liquid sheet. Interestingly, at almost all the test conditions in the present study, a second non-harmonic peak was observed above the noise level in the CPSD diagrams (see e.g., Figure 5d), implying a contribution to the dynamics of the sheet. The corresponding frequencies of these second peaks (open symbols in Figure 8a) do not follow a defined trend relative to the dominant peaks (solid symbols) at each test condition. Similar dual dynamic behaviour was also reported for a conical liquid sheet [68], and for vortex shedding behind a solid cylinder [97].

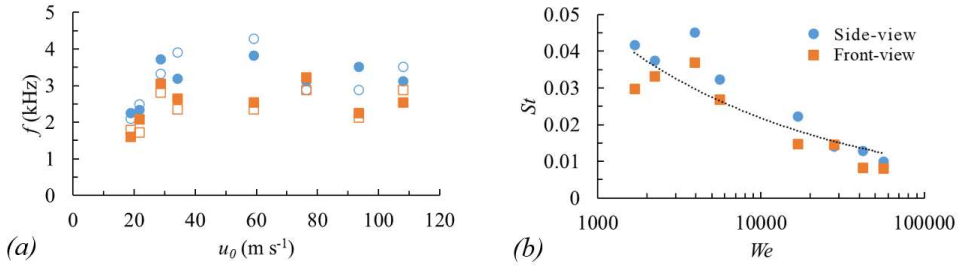

FIGURE 8. A plot of **(a)** f_{sv} (solid circles) and f_{fv} (solid squares) as a function of u_0, and **(b)** dimensionless presentation of the parameters in **(a)** based on We and St. Open symbols in **(a)** are the frequencies of the second non-harmonic peaks in the corresponding CPSD diagrams. The dotted line in **(b)** highlights the decay of St with $We^{-1/3}$.

4. Results and discussion

4.1. Linear stability analysis

The findings of our previous investigations suggest that the disintegration of fan liquid sheets is governed by a succession of instabilities rather than merely the shear KH instability. Therefore, we propose a conjugate model based on LSA, following the stability analysis on an undulating Savart liquid

sheet by Bremond et al. [71], to predict the fan liquid sheet characteristics such as intact radius (Section 4.2) and primary droplet sizes (Section 4.3). In the present model, the primary longitudinal KH instability developed along the liquid sheet initiates a secondary transverse RT instability which is responsible for its breakup. As a result, ligaments form parallel to the sheet free edge, of size governed by the preceding KH and RT instabilities. Following the sheet–ligament–droplet transition paradigm, the ligaments then disintegrate into droplets through a tertiary Plateau-Rayleigh (PR) instability driven by surface tension [4]. A schematic of the fan liquid sheet disintegration is illustrated in Figure 9a, where the underlying physics of the instabilities involved in the fan liquid sheet will be discussed in the following subsections.

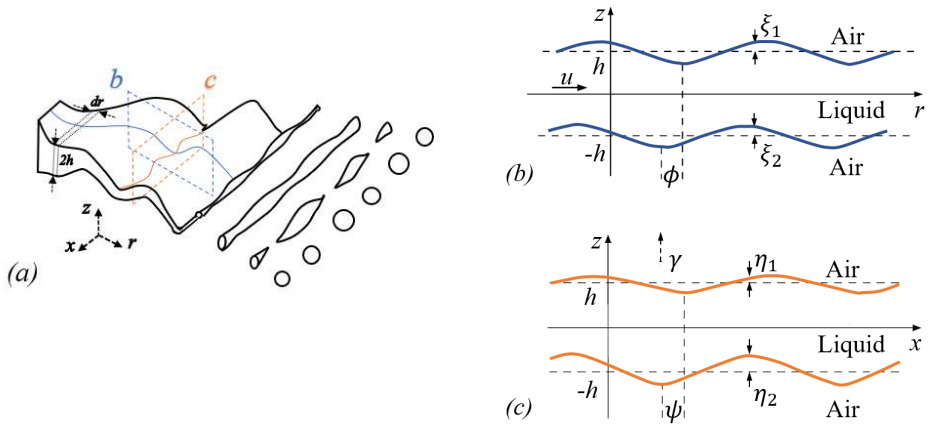

FIGURE 9. Schematic of the **(a)** fan liquid sheet, ligaments and droplets, **(b)** longitudinal instability, corresponding to plane *b* in **(a)**, and **(c)** transverse instability, corresponding to plane *c* in **(a)**.

4.1.1. Longitudinal (streamwise) instabilities

Figure (9b) is a schematic of a KH-type instability that has developed along a thin liquid sheet of density ρ and thickness $2h$, which moves with a uniform velocity u in quiescent air of density ρ_a. The position of both upper and lower interfaces is disturbed by small perturbations, $\xi_1 = \xi_0 \exp(\mathrm{i}kr - \mathrm{i}\omega t)$ and $\xi_2 = \xi_0 \exp(\mathrm{i}kr - \mathrm{i}\omega t + \phi)$, respectively. The dispersion relation of this sheet, which relates the

wavenumber, k, of the disturbance to the frequency, ω, has been developed by Squire [19] for the sinuous mode ($\phi = 0$) as

$$\omega = \frac{uk\tanh(kh/2)}{\tanh(kh/2)+\rho_a/\rho} \pm \frac{(\sigma k^3(\tanh(kh/2)+\rho_a/\rho)/\rho - \rho_a u^2 k^2 \tanh(kh/2)/\rho)^{1/2}}{\tanh(kh/2)+\rho_a/\rho}. \quad (3)$$

In the present study, based on the continuity of a diverging flat sheet and similar to Dombrowski et al. [98], we assume the thickness of the sheet attenuates inversely proportional to the radial distance from the nozzle exit as $2h(r) = c_d^2/r$, where c_d is a dimensional constant and is fixed for a given flow rate (or We) and nozzle design/geometry. We also choose the characteristic scales as half of the liquid sheet thickness at the nozzle exit, h_0, and the liquid velocity of the sheet, u (which is assumed to be constant and equal to its value at the nozzle exit, u_0 [69]), and thus the time scale as h_0/u_0. Therefore, the dimensionless variables, designated by tilde, are as follows.

$$\tilde{\omega} = \frac{\omega h_0}{u_0}, \tilde{k} = kh_0, \tilde{r} = \frac{r}{h_0}, \alpha = \frac{\rho_a}{\rho}, We = \frac{\rho h_0 u_0^2}{\sigma} \quad (4)$$

Accordingly, Eq. (3), in the long-wave approximation ($kh \ll 1$), reduces to its non-dimensional form as a function of $\tilde{r}$ and $\tilde{k}$ as

$$\tilde{\omega} = \frac{\tilde{k}}{1+\beta\alpha\tilde{r}/\tilde{k}} \left\{1 \pm \left[\beta\tilde{r}\left(1+\beta\alpha\tilde{r}/\tilde{k}\right)/We - \beta\alpha\tilde{r}/\tilde{k}\right]^{1/2}\right\}, \quad (5)$$

where $\beta = 4h_0^2/c_d^2$. The sheet is unstable when the sign of the term under the square root is negative, and the sign before this term defines whether a perturbation will grow or decay exponentially with time. Therefore, $\tilde{\omega}$ is split into an imaginary part, $\tilde{\omega}_i$, indicating the temporal growth rate, and a real part $\tilde{\omega}_r$, as follows.

$$\begin{cases} \widetilde{\omega}_i(\tilde{r},\tilde{k}) = \dfrac{(\beta\alpha\tilde{r}\tilde{k})^{1/2}}{1+\beta\alpha\tilde{r}/\tilde{k}}\left(1-\beta\tilde{r}\left(1+\tilde{k}/\beta\alpha\tilde{r}\right)/We\right)^{1/2} \\ \widetilde{\omega}_r(\tilde{r},\tilde{k}) = \dfrac{\tilde{k}}{1+\beta\alpha\tilde{r}/\tilde{k}} \end{cases} \tag{6}$$

Since $\widetilde{\omega}_i$ is a function of the radial location $\tilde{r}$, the overall history of the amplification, which has an exponential behaviour, must be integrated when the waves propagate towards the sheet free edge [51]. Hence, a net gain $G(\tilde{r},\tilde{k})$ can be defined as

$$G(\tilde{r},\tilde{k}) = \ln\left(\frac{\xi(\tilde{r},\tilde{k})}{\xi(0,\tilde{k})}\right) = \int_0^{\tilde{t}} \widetilde{\omega}_i \mathrm{d}\tilde{t} = \int_0^{\tilde{r}} \frac{\widetilde{\omega}_i}{\tilde{c}_g}\mathrm{d}\tilde{r} = \int_0^{\tilde{r}} q\mathrm{d}\tilde{r}\,, \tag{7}$$

where $\tilde{c}_g = \partial\widetilde{\omega}_r/\partial\tilde{k}$ is obtained from Eq. (6), and accordingly q is derived as

$$q(\tilde{r},\tilde{k}) = \frac{1+\beta\alpha\tilde{r}/\tilde{k}}{1+2\beta\alpha\tilde{r}/\tilde{k}}\left(\beta\alpha\tilde{r}\tilde{k}\right)^{1/2}\left(1-\beta\tilde{r}/We-\tilde{k}/\alpha We\right)^{1/2}. \tag{8}$$

As shown by the Squire analysis [19], the most amplified wavenumber of the sheet in its non-dimensional form is expressed as

$$\tilde{k}_m = \frac{\alpha We}{2}. \tag{9}$$

Substituting Eq. (9) into Eq. (8) and then (7) yields an estimate of the amplitude of the most amplified waves of the sheet as a function of $\tilde{r}$:

$$\xi_m(\tilde{r}) = \xi_0 \exp\left(G_m(\tilde{r})\right), \tag{10}$$

where G_m is the corresponding amplification gain which increases with r, and is assumed to reach a constant value of 12 for liquid sheets [16], [17], similar to the findings of Weber for liquid jets [5]. Accordingly, at each We (or injection pressure), we found a value for the unknown parameter c_d such that G_m reaches 12 with distance from the nozzle. As shown in Figure 10a, this condition occurs closer to the

nozzle exit with increasing We, while c_d decreases like $c_d \sim We^{-1}$ (see the inset of Figure 10a). Figure 10b depicts the variation of the amplitude of the most amplified waves with r, up to the sheet breakup location, using Eq. (10). In doing so, we assume the initial values of amplitude, ξ_0, are on the order of molecular dimensions, i.e. 10^{-8} m [99]. As expected from Section 3.2.1, when the waves propagate towards the sheet free edge, their amplitude initially grows exponentially and then oscillates with approximately a constant value, corresponding to the saturation condition of an attenuating liquid sheet [51], [71]. This condition occurs much earlier for the sheets with higher We, which is associated with the region where G_m reaches 12 in Figure 10a.

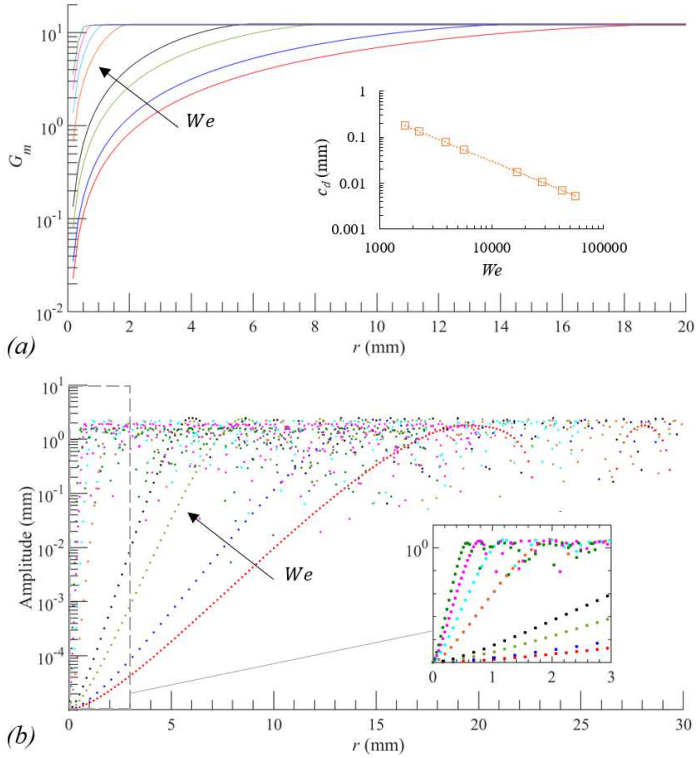

FIGURE 10. Variations of **(a)** amplification gain and **(b)** the amplitude of the most amplified waves with distance from the nozzle at different We mentioned in Table 2. The inset in **(a)** shows the

variation of c_d as a function of We, with We^{-1} plotted as a dotted line. The black arrows show the direction of increasing We and the inset in **(b)** is a zoomed in plot of the high We region.

Figure 11a compares the amplitude of the most amplified waves, obtained by analyzing the side-view images (Table 3) and the present LSA (Eq. (10)) for two different test conditions, cases No. 3 and 7. At low We (case No. 3), the experimental results associated with the saturation region of the sheet up to its breakup location well match the LSA ones, while for case No. 7 at high We, the LSA results underpredict the experimental ones. This could be due to the presence of surface droplets on the periphery of the sheets at high injection pressures [Figure 2b (Multimedia view)] which causes the higher estimates of the sheet amplitude from the experiments. Comparing the maximum amplification of the waves at all test conditions, given by Eq. (10) and Table 3, shows a similar underprediction of LSA results for the sheets at high Weber numbers, see Figure 11b. For $We \gtrsim 10000$, an interesting feature is observed in the results obtained from LSA, where the maximum amplification of the waves is gradually reduced with increasing We. This decrease is attributed to the higher attenuation rate of the sheet at large We, which causes the sheet to reach the saturation condition earlier.

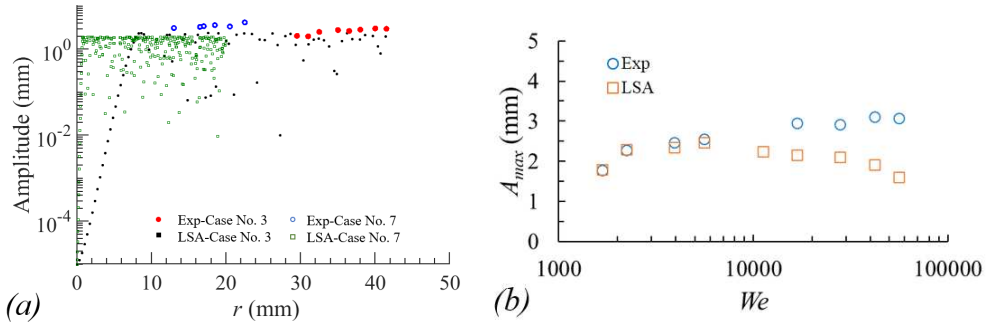

FIGURE 11. A comparison of the LSA predicted values and corresponding experimental results for **(a)** the amplitude of the most amplified waves with distance from the nozzle for case No. 3 (open circle and solid square) and case No. 7 (open triangle and open square) and **(b)** the maximum amplification, A_{max}, of the waves as a function of We.

4.1.2. Transverse (spanwise) instabilities

A schematic of a RT-type instability is depicted in Figure (9c), in which a liquid sheet of density ρ, surface tension σ, and thickness $2h$ is subjected to a constant acceleration γ initially perpendicular to its surfaces. The initial perturbations of the interface positions are proportional to $\eta_1 = \eta_0 \exp(\mathrm{i}kx - \mathrm{i}\omega t)$ and $\eta_2 = \eta_0 \exp(\mathrm{i}kx - \mathrm{i}\omega t + \psi)$ for the upper and lower interfaces, respectively. The dispersion relation of this sheet was developed by Keller and Kolodner [100], neglecting the density of the gas phase surrounding the sheet, as

$$\omega^2 = \frac{\sigma k^3}{\rho}\coth(2kh)\left\{1 \pm [1 - (1 - (k_{ca}/\,k)^4)\tanh^2(kh)]^{1/2}\right\}, \tag{11}$$

where $k_{ca} = \sqrt{\rho\gamma/\sigma}$ is the capillary wavenumber. Equation (4.9) with the minus sign has an unstable range of wavenumbers for $0 < k < k_{ca}$ [77]. For a weak acceleration exerted on a thin layer ($2hk_{ca} \leq 1$), the growth rate of the secondary RT instability is approximated by

$$\omega_m = \left(\frac{\rho(2h)\gamma^2}{2\sigma}\right)^{1/2}, \tag{12}$$

where the most amplified wavenumber can be expressed as

$$k_m = \frac{1}{6^{1/6}}k_{ca}^{4/3}(2h)^{1/3}. \tag{13}$$

An expression for the maximum centripetal acceleration γ, induced by the primary KH instability, can be derived using Eq. (10) as

$$\gamma = \frac{\partial^2\xi_m}{\partial t^2} = \frac{u^2}{h_0^2}\frac{\partial^2\xi_m}{\partial\tilde{r}^2} = \frac{u^2\xi_m}{h_0^2}\left(\frac{\partial q}{\partial\tilde{r}} + q^2\right), \tag{14}$$

where u is again assumed to be constant and equal to u_0. Therefore, the wavelength of the transverse instability, $\lambda_\perp = 2\pi/k_m$, can be estimated using Eq. (13) and the definition of k_{ca} by finding γ from Eq. (14).

Figure 12 compares the values of $\lambda_\perp$ obtained by analyzing the front-view images (Table 4) and the present LSA at the region close to the sheet breakup location. As can be seen from the both the LSA and experimental results, while $\lambda_\perp$ is on the order of the sheet longitudinal wavelength (i.e., λ_{sv} in Table 3) at low We, it decreases like $We^{-2/3}$ with increasing We, because of a larger value of γ at a high Weber number.

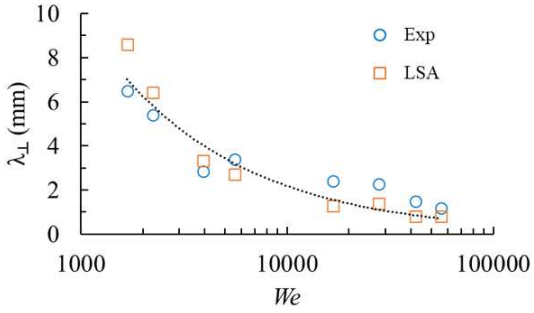

FIGURE 12. A comparison of the LSA values of the transverse instability wavelengths, $\lambda_\perp$, and the corresponding experimental results as a function of We. The dotted line highlights the decay of $\lambda_\perp$ with $We^{-2/3}$.

4.2. Liquid sheet intact radius

Given the role of a secondary RT-type instability in the breakup of a fan liquid sheet into ligaments (Section 3.1), the radial location at which the breakup occurs is estimated by determining the time when the growth time of the RT instability, ω_m^{-1}, is of the order of the travel time along the liquid sheet, τ_c, that is

$$\tau_c = \omega_m^{-1}. \tag{15}$$

The convective timescale of the liquid sheet is estimated as $\tau_c = R/u_0$, where R is the sheet intact radius. The growth rate of the secondary RT instability, ω_m, which includes the effect of the primary KH

instability, is obtained from Eq. (12). To determine γ, the local sheet velocity is estimated using the information in Table 3 as $u = \lambda_{sv} \times f_{sv}$.

Figure 13a compares the values of R estimated by the present LSA (Eq. (15)) for two different test conditions, cases No. 3 and 7. It clearly shows how the larger growth rate of the instabilities for the case with higher We case (No. 7) shortens the intact radius of the liquid sheet. The experimental values of R obtained by analyzing the side-view images (Table 3) and the estimated ones from Eq. (15) are compared for all test conditions in Figure 13b. It is found that R decreases like $We^{-1/3}$ with increasing We, consistent with results reported for Savart liquid sheets [51], because of the higher growth rate of the sheet instabilities at high Weber number.

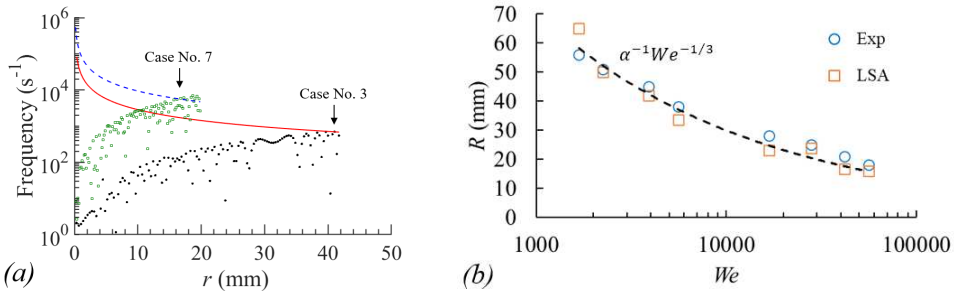

FIGURE 13. A comparison **(a)** of the values of R for cases No. 3 and 7, estimated by Eq. (15) using ω_m (solid and open squares) and $1/\tau_c$ (solid and dashed lines), and **(b)** of the LSA-predicted values of R, estimated by $\alpha^{-1}We^{-1/3}$ (dashed line), and the corresponding experimental results, as a function of We.

4.3. Primary droplet formation

The primary breakup of a liquid sheet results in a spray where small droplets (from the bag fragmentation and/or surface stripping) and large droplets (from ligament breakup) coexist, as shown in Figure 14. The large range of size of the droplets exacerbates the out-of-focus and resolution issues which are inherent in the optical imaging of sprays. As proposed by Asgarian et al. [101], this challenge can be addressed by using an Image Feature Consolidation Technique (IFCT), which consolidates the droplet

size datasets obtained from two sets of backlit images, captured by two different optical setups with different depths of fields (DOF) and resolutions. In the present work, this technique was employed for spray sizing in the region just beyond the sheet breakup (100 mm below the nozzle), using two optical setups: a Phantom Miro LAB 320 with a deep DOF and a low resolution to capture 'High-DOF' images, and Drop Sizer with a shallow DOF and a high resolution to capture 'High-Res' images. The High-DOF images, e.g. Figure 14a, have a DOF of 6250 µm that bring large droplets (diameter ≥ 200 µm) into focus; however, due to the low resolution of 19.8 µm/pixel, smaller droplets are not resolved. On the other hand, High-Res images, e.g. Figure 14b, with a DOF of 900 µm and a resolution of 1.2 – 2.4 µm/pixel, clearly resolve small and medium size droplets (10 µm ≤ diameter < 200 µm); however, larger droplets appear partially out-of-focus and are thus subject to rejection during image processing. The images were analyzed in batches with the open-source image processing software ImageJ, version 1.52a. Each set of images underwent a series of image processing steps including cropping, bandpass filtering, adjusting the threshold, removing outliers, and particle analyzing, the details of which can be found in [101]. An important feature of IFCT is a graphical machine learning method, the Receiver Operating Characteristic (ROC) curve, that chooses an optimal threshold value for binary classification of images based on the light intensity. As a result, the thresholding error when estimating the diameter of an individual droplet is less than 5%.

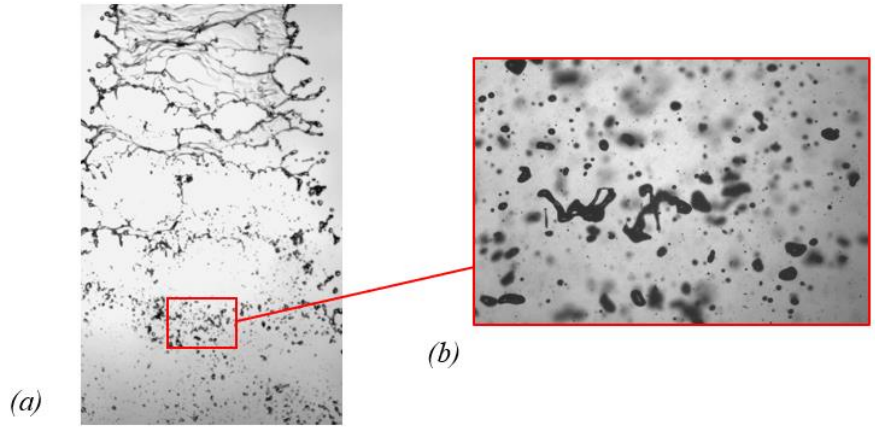

FIGURE 14. Images of a water spray at $\Delta p = 20.7$ bar (case No. 5), captured by **(a)** Phantom Miro LAB 320 and **(b)** Drop Sizer (see spray sizing information in Table 1). The centers of these images are100 mm below the nozzle.

Histograms of droplet size distribution (DSD) were acquired by independently processing 200 High-DOF and 200 High-Res images, as shown in Figures15a and b. More than 16000 droplets were captured in the 200 images, ensuring that the DSD is independent of the sample size.

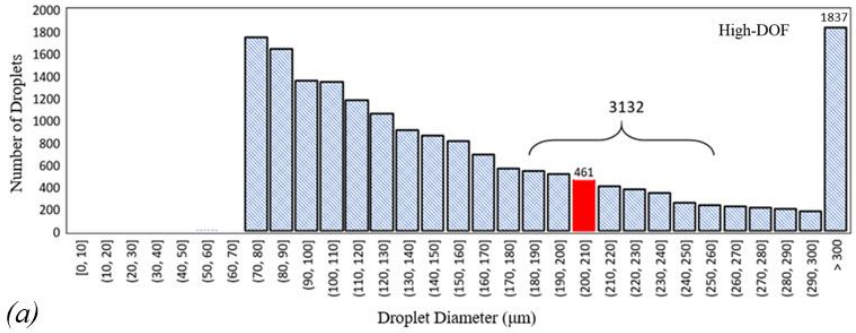

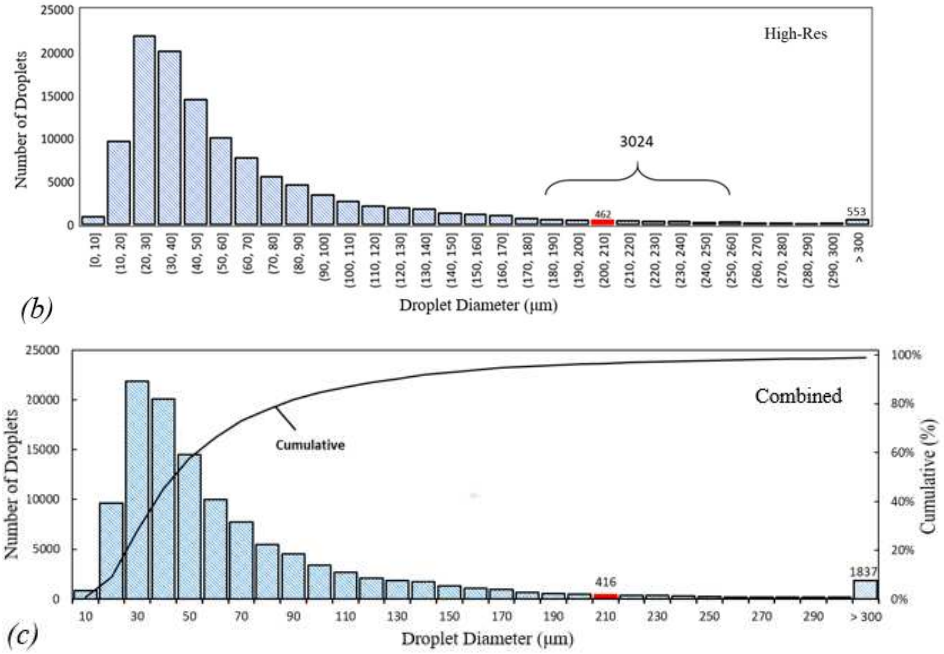

FIGURE 15. Histograms of droplet size distribution for the water spray at $\Delta p = 20.7$ bar (case No. 5) at 100 mm below the nozzle, obtained **(a)** from High-DOF images, **(b)** from High-Res images, and **(c)** by combining **(a)** and **(b)**.

As seen in Figures 15a and b, the two histograms almost agree on the droplet count in the range 180 – 260 μm, and yield almost the same count for the 200 – 210 μm bin. The High-DOF and the High-Res histograms exhibit dramatic drops in droplet count below the 180 μm and beyond the 260 μm bins, respectively. To obtain a single histogram, data from the two histograms was consolidated; the droplet counts for the larger droplets (diameter ≥ 200 μm) were adopted from the High-DOF histogram, and the droplet counts for the smaller droplets (10 μm ≤ diameter < 200 μm) from the High-Res histogram, yielding the combined histogram shown in Figure 15c. The same process was repeated for sprays at different injection pressures Δp, and mean diameters were calculated as listed in Table 5.

TABLE 5. Results of spray sizing at different pressures Δp

Case	Injection Pressure, Δp (bar)	Arithmetic mean diameter, D_{10} (μm)	Sauter mean diameter, D_{32} (μm)	Droplet median diameter (by count), D_{50} (μm)	Droplet median diameter (by volume), $D_{0.5}$ (μm)
2	2.8	67	342	57	474
5	20.7	65	266	41	397
6	34.5	59	239	40	352
7	51.7	57	225	37	335
new[a]	103.4	51	202	33	302
new[a]	117.2	49	198	32	297

[a] Based on the data supplied by the nozzle manufacturer for extrapolating the measured droplet sizes in Figure 16

Following the study of Fraser et al. [16] on fan liquid sheets, we consider that at the sheet overall breakup location (see Figure 14a), a liquid strip of width $\lambda_{sv}{\sim}We^{-1/6}$ (from Table 3) and thickness $h = c_d^2/2R \sim We^{-5/3}$ (since $c_d{\sim}We^{-1}$ and $R{\sim}We^{-1/3}$) detaches from the sheet and generates a cylindrical ligament, the radius of which is estimated from a mass balance then destabilized through a surface tension-driven PR-type instability whose wavelength is proportional to the ligament radius. Then the average size of droplets formed by the ligament disintegration can be scaled as Eq. (16), which is close to the study of Villermaux and Clanet [51] on Savart liquid sheets at high Weber numbers.

$$D_{0.5}{\sim}\sqrt{\lambda_{sv}h} \sim We^{-11/12}. \tag{16}$$

Note that Kooij et al. [30] also performed a similar analysis but based on KH-type instabilities only and estimated the droplet sizes vary like $We^{-1/3}$. Their correlation, however, applies to a smaller range of pressures (1 to 5 bar) and further afield (400 mm below the nozzle).

As shown in Figure 16, while the estimated LSA trend of $D_{0.5}$ (based on Eq. 16) shows good agreement with the results of the High-Res images at high We, the diameters obtained from IFCT (Table 5) are larger. This is because of the presence of some large-volume irregular-shaped droplets/ligaments in the sampling region at high injection pressures, see Figure 16b, which significantly affects the volume median diameter of the sprays estimated by IFCT. They are, however, filtered by the High-Res method, which is sensitive to the size and sphericity of particles. On the other hand, at low We, the results of the

High-Res images underestimate the LSA results because the shallow DOF of its optical setup excludes the large but regular-shaped droplets that coexist with small ones in the sampling region, see Figure 16a. Therefore, a combination of both techniques is used to estimate the volume median diameter of the regular-shaped (near spherical) primary droplets formed over the whole range of Weber numbers investigated in the present study, as depicted by solid symbols in Figure 16c.

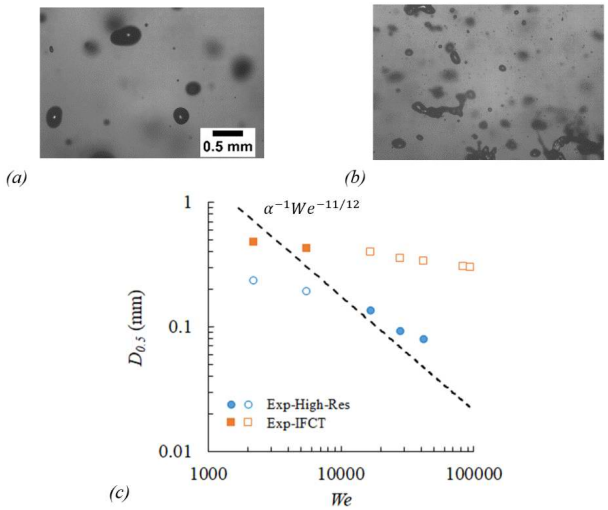

FIGURE 16. Typical images of the spray droplets captured by Drop Sizer at **(a)** $\Delta p = 2.8$ bar (case No. 2) and **(b)** $\Delta p = 34.5$ bar (case No. 6), along with **(c)** a comparison of the LSA-predicted values of the volume median diameter of the primary droplets, estimated by $\alpha^{-1}We^{-11/12}$ (dashed line), and corresponding experimental results from High-Res images and IFCT as a function of We. The primary droplet sizes obtained from the experimental results are shown by the solid symbols.

5. Summary and conclusions

The spatio-temporal dynamics and disintegration of a fan liquid sheet injected into a quiescent atmosphere at different pressures were experimentally and theoretically studied. The 'wavy corridor' mechanism was used to describe the breakup of the liquid sheets, based on the formation-growth-fragmentation process of bag-like structures along the liquid sheets that we observed in high-speed backlit images. The spatially-evolving coherent structures on the liquid sheets were analyzed using POD and

spectral methods. The predictions of our conjugate model, based on LSA of both KH and RT instabilities, are consistent with the quantitative results, which clearly shows the role of transverse instabilities (or bags) in governing the breakup of fan liquid sheets. The side-view wave analyses clearly show the growth saturation of the longitudinal instabilities because of the attenuation of the fan liquid sheet with distance from the nozzle. Interestingly, the model predicts a gradual decrease in the maximum amplification of the longitudinal waves for sheets at $We \gtrsim 10000$, which was not observable experimentally due probably to surface droplets shrouding the sheets. Considering the influence of viscosity and boundary layer thickness across the liquid-gas interface on the predictions of the LSA could reduce the discrepancies. The transverse instabilities were also characterized via front-view wave analyses. Overall, the sheet characterizations from both points of view demonstrate that the Strouhal number of the sheets reduces with increasing We, though they exhibit a dual dynamic behaviour which requires further investigation. Furthermore, this study shows that the intact radius of the fan liquid sheets and the volume median diameter of primary droplets (formed through PR instabilities) decrease as $We^{-1/3}$ and $We^{-11/12}$, respectively. Finally, the use of IFCT for droplet sizing is shown to be a suitable method when a spray consists of a multi-range droplet sizes which are a challenge to be characterized by a single optical setup.

Acknowledgments

The POD analyses were performed on the GPC supercomputer at the SciNet HPC Consortium. SciNet is funded by the Canada Foundation for Innovation under the auspices of Compute Canada, the Government of Ontario, Ontario Research Fund Research Excellence, and the University of Toronto.

References

[1] A. Lefebvre and V. McDonell, *Atomization and Sprays*, 2nd ed. Boca Raton: CRC Press, 2017.

[2] L. Bayvel and Z. Orzechowski, *Liquid Atomization*. Taylor & Francis, 1993.

[3] N. Ashgriz, *Handbook of Atomization and Sprays: Theory and Applications*. Springer Science & Business Media, 2011.

[4] Lord Rayleigh, "On The Instability Of Jets," *Proc. London Math. Soc.*, vol. s1-10, no. 1, pp. 4–13, Nov. 1878.

[5] C. WEBER, "Disintegration of liquid jets," *Z. Angew Math. Mech*, vol. 11, pp. 136–159, 1931.

[6] G. I. Taylor, "Generation of ripples by wind blowing over a viscous fluid," *Pap. Writ. Chem. Def. Res. Dep. Minist. Sci. (Reprinted Sci. Pap. Sir Geofferey Ingram Taylor, vol. 3, p. 244, Cambridge Univ. Press. 1940.)*, 1940.

[7] J. Eggers, "Nonlinear dynamics and breakup of free-surface flows," *Rev. Mod. Phys.*, vol. 69, no. 3, pp. 865–930, Jul. 1997.

[8] E. Villermaux, "Fragmentation versus Cohesion," *J. Fluid Mech.*, vol. 898, p. P1, 2020.

[9] O. D. Neikov, "Chapter 5 - Atomization and Granulation," O. D. Neikov, S. S. Naboychenko, I. V Murashova, V. G. Gopienko, I. V Frishberg, and D. V. B. T.-H. of N.-F. M. P. Lotsko, Eds. Oxford: Elsevier, 2009, pp. 102–142.

[10] J. J. Dunkley, "Metal powder atomization methods for modern manufacturing," *Johnson Matthey Technol. Rev.*, vol. 63, no. 3, pp. 226–232, 2019.

[11] A. Asgarian, Z. Tang, M. Bussmann, and K. Chattopadhyay, "Water atomisation of metal powders: effect of water spray configuration," *Powder Metall.*, vol. 63, no. 4, pp. 288–299, Aug. 2020.

[12] G. J. Dorr, A. J. Hewitt, S. W. Adkins, J. Hanan, H. Zhang, and B. Noller, "A comparison of initial spray characteristics produced by agricultural nozzles," *Crop Prot.*, vol. 53, pp. 109–117, 2013.

[13] A. Altieri, S. Cryer, and L. Acharya, "Mechanisms, experiment, and theory of liquid sheet breakup and drop size from agricultural nozzles," *At. Sprays*, vol. 24, pp. 695–721, Jan. 2014.

[14] H. Liu, *Science and Engineering of Droplets: Fundamentals and Applications*. William Andrew,

1999.

[15] N. Dombrowski, R. P. Fraser, and D. M. Newitt, "A photographic investigation into the disintegration of liquid sheets," *Philos. Trans. R. Soc. London. Ser. A, Math. Phys. Sci.*, vol. 247, no. 924, pp. 101–130, Sep. 1954.

[16] R. P. Fraser, P. Eisenklam, N. Dombrowski, and D. Hasson, "Drop formation from rapidly moving liquid sheets," *AIChE J.*, vol. 8, no. 5, pp. 672–680, Nov. 1962.

[17] N. Dombrowski and P. C. Hooper, "The effect of ambient density on drop formation in sprays," *Chem. Eng. Sci.*, vol. 17, no. 4, pp. 291–305, 1962.

[18] S. CHANDRASEKHAR, *Hydrodynamic and Hydromagnetic Stability*. Courier Corporation, 2013.

[19] H. B. Squire, "Investigation of the instability of a moving liquid film," *Br. J. Appl. Phys.*, vol. 4, no. 6, pp. 167–169, 1953.

[20] J. L. York, H. E. Stubbs, and M. R. Tek, "The mechanism of disintegration of liquid sheets," *Trans. ASME*, vol. 75, no. 7, pp. 1279–1286, 1953.

[21] W. W. Hagerty and J. F. Shea, "A study of the stability of plane fluid sheets," *J. Appl. Mech*, vol. 22, pp. 509–514, 1955.

[22] A. Mansour and N. Chigier, "Disintegration of liquid sheets," *Phys. Fluids A Fluid Dyn.*, vol. 2, no. 5, pp. 706–719, May 1990.

[23] B. E. Stapper, W. A. Sowa, and G. S. Samuelsen, "An Experimental Study of the Effects of Liquid Properties on the Breakup of a Two-Dimensional Liquid Sheet," *J. Eng. Gas Turbines Power*, vol. 114, no. 1, pp. 39–45, Jan. 1992.

[24] S. P. Lin, *Breakup of Liquid Sheets and Jets*. Cambridge: Cambridge University Press, 2003.

[25] W. A. Sirignano and C. Mehring, "Review of theory of distortion and disintegration of liquid streams," *Prog. Energy Combust. Sci.*, vol. 26, no. 4, pp. 609–655, 2000.

[26] L.-J. Liu, L.-J. Yang, and H.-Y. Ye, "Weakly nonlinear varicose-mode instability of planar liquid sheets," *Phys. Fluids*, vol. 28, no. 3, p. 34105, Mar. 2016.

[27] N. Dombrowski and W. R. Johns, "The aerodynamic instability and disintegration of viscous liquid sheets," *Chem. Eng. Sci.*, vol. 18, no. 3, pp. 203–214, 1963.

[28] G. D. Crapper, N. Dombrowski, W. P. Jepson, and M. J. Lighthill, "Wave growth on thin sheets of non-Newtonian liquids," *Proc. R. Soc. London. A. Math. Phys. Sci.*, vol. 342, no. 1629, pp. 225–236, Feb. 1975.

[29] X. Li and R. S. Tankin, "On the temporal instability of a two-dimensional viscous liquid sheet," *J. Fluid Mech.*, vol. 226, pp. 425–443, 1991.

[30] S. Kooij, R. Sijs, M. M. Denn, E. Villermaux, and D. Bonn, "What Determines the Drop Size in Sprays?," *Phys. Rev. X*, vol. 8, no. 3, p. 31019, Jul. 2018.

[31] N. Majumdar and M. S. Tirumkudulu, "Growth of sinuous waves on thin liquid sheets: Comparison of predictions with experiments," *Phys. Fluids*, vol. 28, no. 5, p. 52101, May 2016.

[32] P. K. Senecal, D. P. Schmidt, I. Nouar, C. J. Rutland, R. D. Reitz, and M. L. Corradini, "Modeling high-speed viscous liquid sheet atomization," *Int. J. Multiph. Flow*, vol. 25, no. 6, pp. 1073–1097, 1999.

[33] S. S. Deshpande, S. R. Gurjar, and M. F. Trujillo, "A computational study of an atomizing liquid sheet," *Phys. Fluids*, vol. 27, no. 8, p. 82108, Aug. 2015.

[34] A. Zandian, W. A. Sirignano, and F. Hussain, "Planar liquid jet: Early deformation and atomization cascades," *Phys. Fluids*, vol. 29, no. 6, p. 62109, Jun. 2017.

[35] A. Arote, M. Bade, and J. Banerjee, "Numerical investigations on stability of the spatially oscillating planar two-phase liquid jet in a quiescent atmosphere," *Phys. Fluids*, vol. 31, no. 11, p. 112103, Nov. 2019.

[36] S. Schmidt and K. Oberleithner, "Instability of forced planar liquid jets: mean field analysis and nonlinear simulation," *J. Fluid Mech.*, vol. 883, p. A7, 2020.

[37] A. Della Pia, M. Chiatto, and L. de Luca, "Global eigenmodes of thin liquid sheets by means of Volume-of-Fluid simulations," *Phys. Fluids*, vol. 32, no. 8, p. 82112, Aug. 2020.

[38] A. Della Pia, M. Chiatto, and L. de Luca, "Receptivity to forcing disturbances in subcritical liquid sheet flows," *Phys. Fluids*, vol. 33, no. 3, p. 32113, Mar. 2021.

[39] L. RAYNAL, J. C. VILLERMAUX, E., LASHERAS, and E. J. HOPFINGER, "Primary instability in liquid–gas shear layers," in *11th Symposium on Turbulent Shear Flows, Grenoble, France*, 1997, pp. 27.1–27.5.

[40] D. Fuster *et al.*, "Instability regimes in the primary breakup region of planar coflowing sheets," *J. Fluid Mech.*, vol. 736, pp. 150–176, 2013.

[41] D. Dasgupta, S. Nath, and D. Bhanja, "A study on dual role of viscosity on the stability of a viscous planar liquid sheet surrounded by inviscid gas streams of equal velocities, and prediction of resulting droplet distribution using maximum entropy formulation," *Phys. Fluids*, vol. 31, no. 7, p. 74103, Jul. 2019.

[42] N. Odier, G. Balarac, C. Corre, and V. Moureau, "Numerical study of a flapping liquid sheet sheared by a high-speed stream," *Int. J. Multiph. Flow*, vol. 77, pp. 196–208, 2015.

[43] G. G. Agbaglah, "Numerical study of hole formation in a thin flapping liquid sheet sheared by a fast gas stream," *Phys. Fluids*, vol. 33, no. 6, p. 62119, Jun. 2021.

[44] G. I. Taylor, "The dynamics of thin sheets of fluid. III. Disintegration of fluid sheets," *Proc. R. Soc. London. Ser. A. Math. Phys. Sci.*, vol. 253, no. 1274, pp. 313–321, Dec. 1959.

[45] C. CLANET and E. VILLERMAUX, "Life of a smooth liquid sheet," *J. Fluid Mech.*, vol. 462, pp. 307–340, 2002.

[46] M. Paramati, M. S. Tirumkudulu, and P. J. Schmid, "Stability of a moving radial liquid sheet: experiments," *J. Fluid Mech.*, vol. 770, pp. 398–423, 2015.

[47] N. Dombrowski and P. C. Hooper, "A study of the sprays formed by impinging jets in laminar and turbulent flow," *J. Fluid Mech.*, vol. 18, no. 3, pp. 392–400, 1964.

[48] J. W. M. BUSH and A. E. HASHA, "On the collision of laminar jets: fluid chains and fishbones," *J. Fluid Mech.*, vol. 511, pp. 285–310, 2004.

[49] N. BREMOND and E. VILLERMAUX, "Atomization by jet impact," *J. Fluid Mech.*, vol. 549, pp. 273–306, 2006.

[50] F. Savart, "Mémoire sur le choc d'une veine liquide lancée contre un plan circulaire," *Ann. Chim.*, vol. 54, pp. 56–87, 1833.

[51] E. VILLERMAUX and C. CLANET, "Life of a flapping liquid sheet," *J. Fluid Mech.*, vol. 462, pp. 341–363, 2002.

[52] Rayleigh, "Investigation of the Character of the Equilibrium of an Incompressible Heavy Fluid of Variable Density," *Proc. London Math. Soc.*, vol. s1-14, no. 1, pp. 170–177, Nov. 1882.

[53] G. Taylor, "The Instability of Liquid Surfaces when Accelerated in a Direction Perpendicular to their Planes. I," *Proc. R. Soc. Lond. A. Math. Phys. Sci.*, vol. 201, no. 1065, pp. 192–196, Jun. 1950.

[54] L. RAYLEIGH, "Some Applications of Photography1," *Nature*, vol. 44, no. 1133, pp. 249–254, 1891.

[55] K. Pearson, "On lines and planes of closest fit to systems of points in space," *London, Edinburgh, Dublin Philos. Mag. J. Sci.*, vol. 2, no. 11, pp. 559–572, Nov. 1901.

[56] J. L. Lumley, *Stochastic Tools in Turbulence*. Academic Press, 1970.

[57] L. Sirovich, "Turbulence and the dynamics of coherent structures. Part I. Coherent structures," *Q. Appl. Maths*, vol. 45, pp. 561–571, 1987.

[58] P. J. SCHMID, "Dynamic mode decomposition of numerical and experimental data," *J. Fluid Mech.*, vol. 656, pp. 5–28, 2010.

[59] M. Sieber, C. O. Paschereit, and K. Oberleithner, "Spectral proper orthogonal decomposition," *J. Fluid Mech.*, vol. 792, pp. 798–828, 2016.

[60] A. Towne, O. T. Schmidt, and T. Colonius, "Spectral proper orthogonal decomposition and its relationship to dynamic mode decomposition and resolvent analysis," *J. Fluid Mech.*, vol. 847, pp. 821–867, 2018.

[61] M. Arienti and M. C. Soteriou, "Time-resolved proper orthogonal decomposition of liquid jet dynamics," *Phys. Fluids*, vol. 21, no. 11, p. 112104, Nov. 2009.

[62] M. Herrmann, M. Arienti, and M. Soteriou, "The Impact of Density Ratio on the Liquid Core Dynamics of a Turbulent Liquid Jet Injected Into a Crossflow," *J. Eng. Gas Turbines Power*, vol. 133, no. 6, p. 061501, Jun. 2011.

[63] M. Broumand, M. Birouk, and S. V. Mahmoodi J., "Liquid jet primary breakup in a turbulent cross-airflow at low Weber number," *J. Fluid Mech.*, vol. 879, pp. 775–792, 2019.

[64] G. Charalampous and Y. Hardalupas, "Application of Proper Orthogonal Decomposition to the morphological analysis of confined co-axial jets of immiscible liquids with comparable densities," *Phys. Fluids*, vol. 26, no. 11, p. 113301, Nov. 2014.

[65] G. Charalampous, C. Hadjiyiannis, and Y. Hardalupas, "Proper orthogonal decomposition of primary breakup and spray in co-axial airblast atomizers," *Phys. Fluids*, vol. 31, no. 4, p. 43304, Apr. 2019.

[66] A. Kumar and S. Sahu, "Large scale instabilities in coaxial air-water jets with annular air swirl," *Phys. Fluids*, vol. 31, no. 12, p. 124103, Dec. 2019.

[67] K. Rajamanickam and S. Basu, "Insights into the dynamics of spray–swirl interactions," *J. Fluid*

Mech., vol. 810, pp. 82–126, 2017.

[68] K. Dhivyaraja, D. Gaddes, E. Freeman, S. Tadigadapa, and M. V Panchagnula, "Dynamical similarity and universality of drop size and velocity spectra in sprays," *J. Fluid Mech.*, vol. 860, pp. 510–543, 2019.

[69] A. Asgarian, M. Heinrich, R. Schwarze, M. Bussmann, and K. Chattopadhyay, "Experiments and modeling of the breakup mechanisms of an attenuating liquid sheet," *Int. J. Multiph. Flow*, vol. 130, p. 103347, 2020.

[70] P. Marmottant and E. Villermaux, "On spray formation," *J. Fluid Mech.*, vol. 498, pp. 73–111, 2004.

[71] N. BREMOND, C. CLANET, and E. VILLERMAUX, "Atomization of undulating liquid sheets," *J. Fluid Mech.*, vol. 585, pp. 421–456, 2007.

[72] F. E. J. Briffa and N. Dombrowski, "Entrainment of air into a liquid spray," *AIChE J.*, vol. 12, no. 4, pp. 708–717, Jul. 1966.

[73] P. YECKO and S. ZALESKI, "Transient growth in two-phase mixing layers," *J. Fluid Mech.*, vol. 528, pp. 43–52, 2005.

[74] L. Qin, R. Yi, and L. Yang, "Theoretical breakup model in the planar liquid sheets exposed to high-speed gas and droplet size prediction," *Int. J. Multiph. Flow*, vol. 98, pp. 158–167, 2018.

[75] C. (井上智博) Inoue and I. (前田一貫) Maeda, "On the droplet entrainment from gas-sheared liquid film," *Phys. Fluids*, vol. 33, no. 1, p. 11705, Jan. 2021.

[76] J. C. LASHERAS, E. VILLERMAUX, and E. J. HOPFINGER, "Break-up and atomization of a round water jet by a high-speed annular air jet," *J. Fluid Mech.*, vol. 357, pp. 351–379, 1998.

[77] N. BREMOND and E. VILLERMAUX, "Bursting thin liquid films," *J. Fluid Mech.*, vol. 524, pp. 121–130, 2005.

[78] W.-H. Chou and G. M. Faeth, "Temporal properties of secondary drop breakup in the bag breakup regime," *Int. J. Multiph. Flow*, vol. 24, no. 6, pp. 889–912, 1998.

[79] E. Villermaux, "Fragmentation," *Annu. Rev. Fluid Mech.*, vol. 39, no. 1, pp. 419–446, Dec. 2006.

[80] Z. Farago and N. Chigier, "Morphological classification of disintegration of round jets in a coaxial airstream," *At. Sprays*, vol. 2, no. 2, pp. 137–153, 1992.

[81] J. C. Lasheras and E. J. Hopfinger, "Liquid Jet Instability and Atomization in a Coaxial Gas Stream," *Annu. Rev. Fluid Mech.*, vol. 32, no. 1, pp. 275–308, Jan. 2000.

[82] C.-L. Ng, R. Sankarakrishnan, and K. A. Sallam, "Bag breakup of nonturbulent liquid jets in crossflow," *Int. J. Multiph. Flow*, vol. 34, no. 3, pp. 241–259, Mar. 2008.

[83] M. Broumand and M. Birouk, "Liquid jet in a subsonic gaseous crossflow: Recent progress and remaining challenges," *Prog. Energy Combust. Sci.*, vol. 57, pp. 1–29, Nov. 2016.

[84] M. Broumand and M. Birouk, "Effect of nozzle-exit conditions on the near-field characteristics of a transverse liquid jet in a subsonic uniform cross airflow," *Phys. Fluids*, vol. 29, no. 11, 2017.

[85] M. Arienti *et al.*, "Comparison of simulation and experiments for multimode aerodynamic breakup of a liquid metal column in a shock-induced cross-flow," *Phys. Fluids*, vol. 31, no. 8, p. 82110, Aug. 2019.

[86] C. Vernay, L. Ramos, and C. Ligoure, "Bursting of Dilute Emulsion-Based Liquid Sheets Driven by a Marangoni Effect," *Phys. Rev. Lett.*, vol. 115, no. 19, p. 198302, Nov. 2015.

[87] A. L. Altieri and S. A. Cryer, "Break-up of sprayed emulsions from flat-fan nozzles using a hole kinematics model," *Biosyst. Eng.*, vol. 169, pp. 104–114, 2018.

[88] H. Lhuissier and E. Villermaux, "'Effervescent' atomization in two dimensions," *J. Fluid Mech.*, vol. 714, pp. 361–392, 2013.

[89] G. I. Taylor and L. Howarth, "The dynamics of thin-sheets of fluid. I. Water bells," *Proc. R. Soc.*

London. Ser. A. Math. Phys. Sci., vol. 253, no. 1274, pp. 289–295, Dec. 1959.

[90] F. E. C. Culick, "Comments on a Ruptured Soap Film," *J. Appl. Phys.*, vol. 31, no. 6, pp. 1128–1129, Jun. 1960.

[91] B. Néel and E. Villermaux, "The spontaneous puncture of thick liquid films," *J. Fluid Mech.*, vol. 838, pp. 192–221, 2018.

[92] A. Chatterjee, "An introduction to the proper orthogonal decomposition," *Curr. Sci.*, vol. 78, no. 7, pp. 808–817, 2000.

[93] K. E. MEYER, J. M. PEDERSEN, and O. ÖZCAN, "A turbulent jet in crossflow analysed with proper orthogonal decomposition," *J. Fluid Mech.*, vol. 583, pp. 199–227, 2007.

[94] H. Nobach *et al.*, "Review of Some Fundamentals of Data Processing BT - Springer Handbook of Experimental Fluid Mechanics," C. Tropea, A. L. Yarin, and J. F. Foss, Eds. Berlin, Heidelberg: Springer Berlin Heidelberg, 2007, pp. 1337–1398.

[95] D. Rempfer and H. F. Fasel, "Evolution of three-dimensional coherent structures in a flat-plate boundary layer," *J. Fluid Mech.*, vol. 260, pp. 351–375, 1994.

[96] A. LOZANO, F. BARRERAS, G. HAUKE, and C. DOPAZO, "Longitudinal instabilities in an air-blasted liquid sheet," *J. Fluid Mech.*, vol. 437, pp. 143–173, 2001.

[97] P. W. Bearman, "On vortex shedding from a circular cylinder in the critical Reynolds number régime," *J. Fluid Mech.*, vol. 37, no. 3, pp. 577–585, 1969.

[98] N. Dombrowski, D. Hasson, and D. E. Ward, "Some aspects of liquid flow through fan spray nozzles," *Chem. Eng. Sci.*, vol. 12, no. 1, pp. 35–50, 1960.

[99] C. J. Clark, N. Dombrowski, and G. I. Taylor, "Aerodynamic instability and disintegration of inviscid liquid sheets," *Proc. R. Soc. London. A. Math. Phys. Sci.*, vol. 329, no. 1579, pp. 467–478, Sep. 1972.

[100] J. B. Keller and I. Kolodner, "Instability of Liquid Surfaces and the Formation of Drops," *J. Appl. Phys.*, vol. 25, no. 7, pp. 918–921, Jul. 1954.

[101] A. Asgarian, Z. Yang, Z. Tang, M. Bussmann, and K. Chattopadhyay, "An image feature consolidation technique (IFCT) to capture multi-range droplet size distributions in atomizing liquid sheets," *Exp. Fluids*, vol. 61, no. 1, p. 14, 2019.

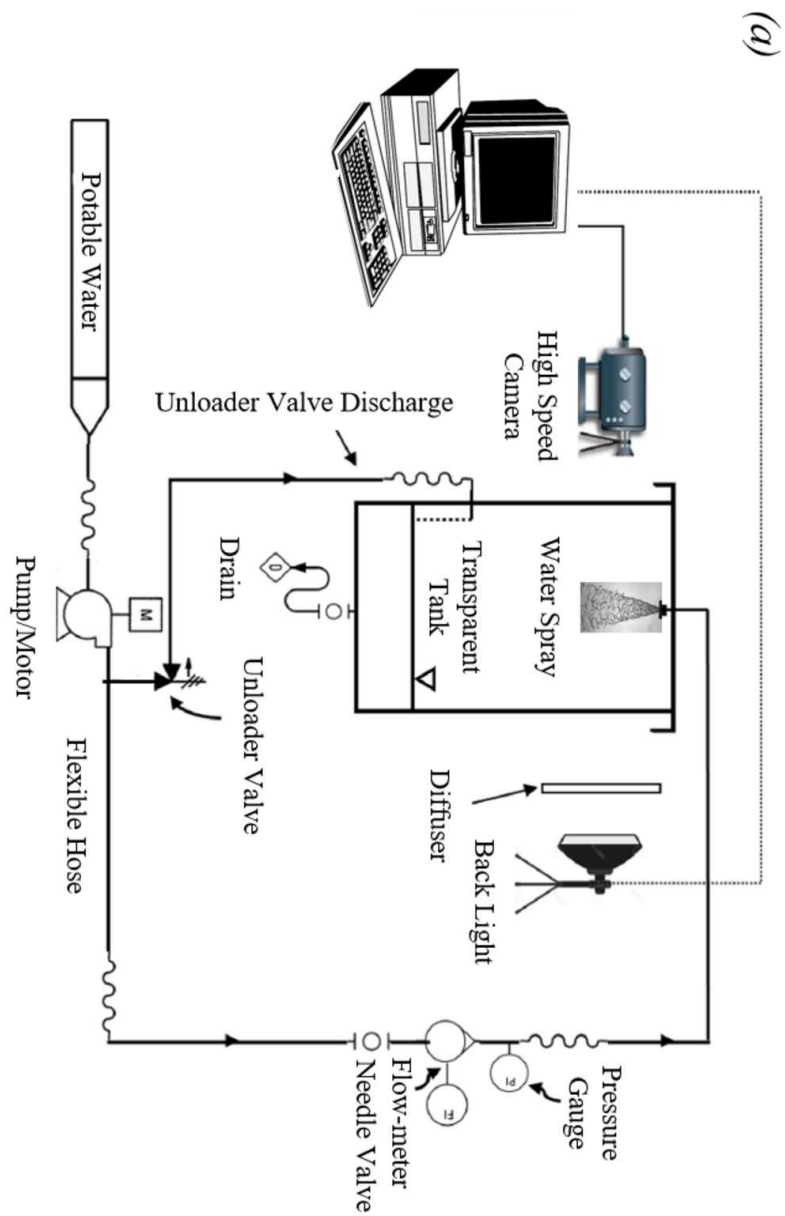

PLEASE CITE THIS ARTICLE AS DOI: 10.1063/5.0063049

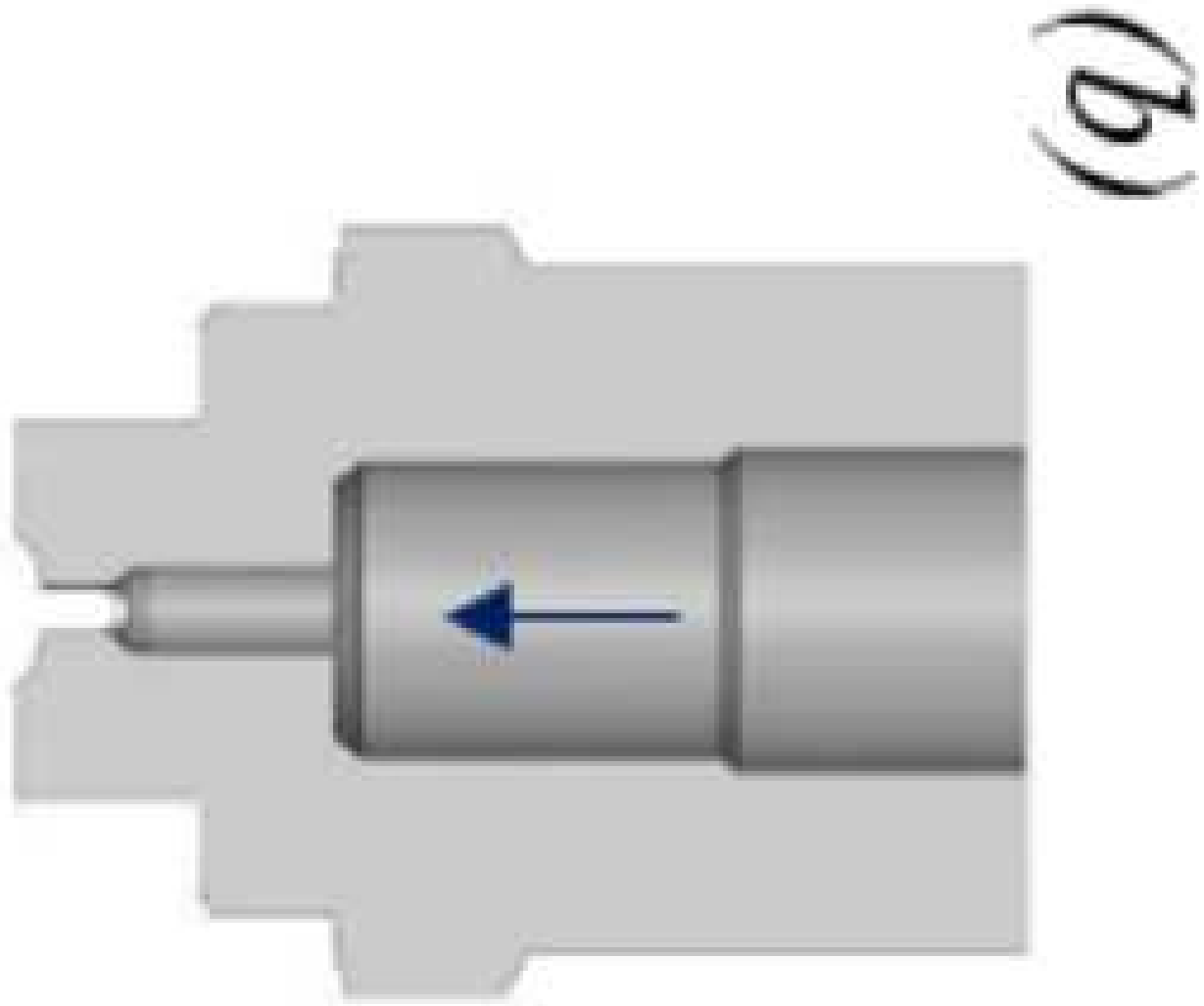

PLEASE CITE THIS ARTICLE AS DOI: 10.1063/5.0063049

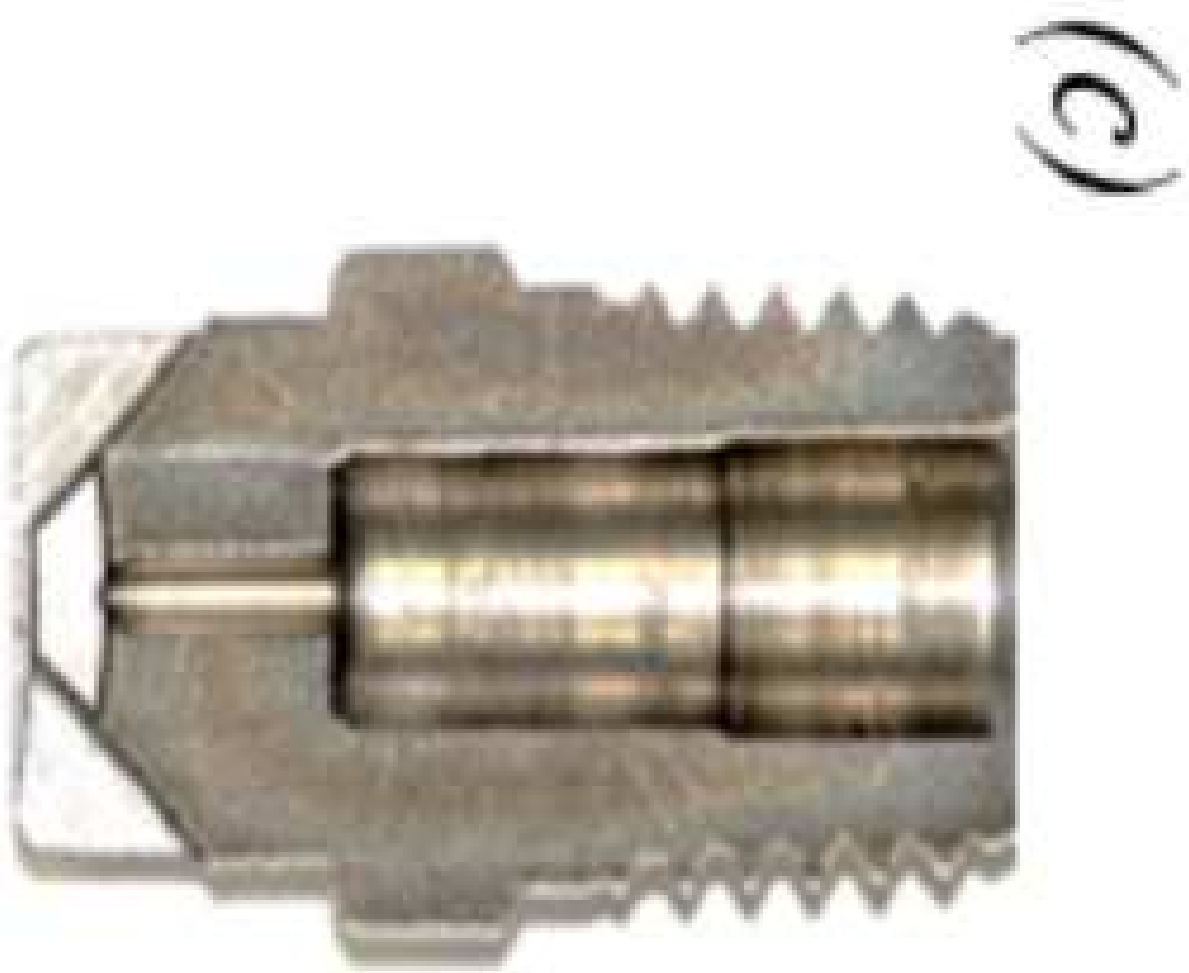

PLEASE CITE THIS ARTICLE AS DOI: 10.1063/5.0063049

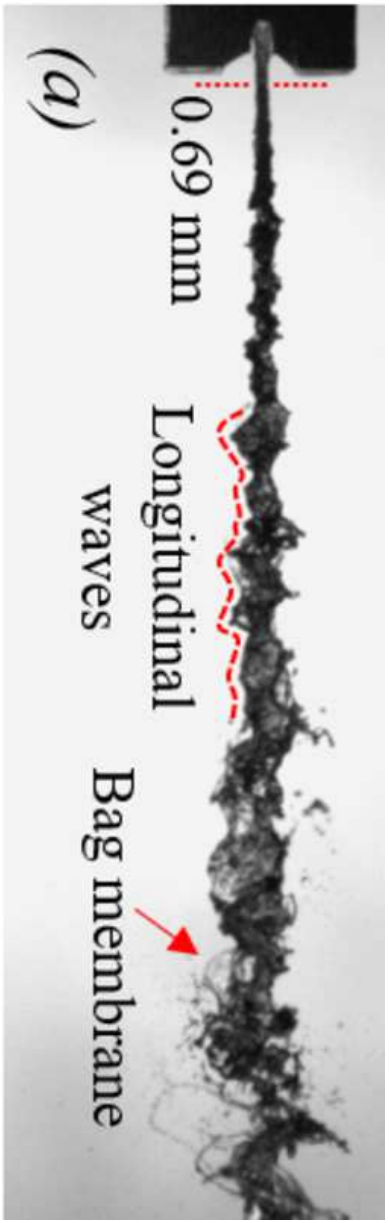

PLEASE CITE THIS ARTICLE AS DOI: 10.1063/5.0063049

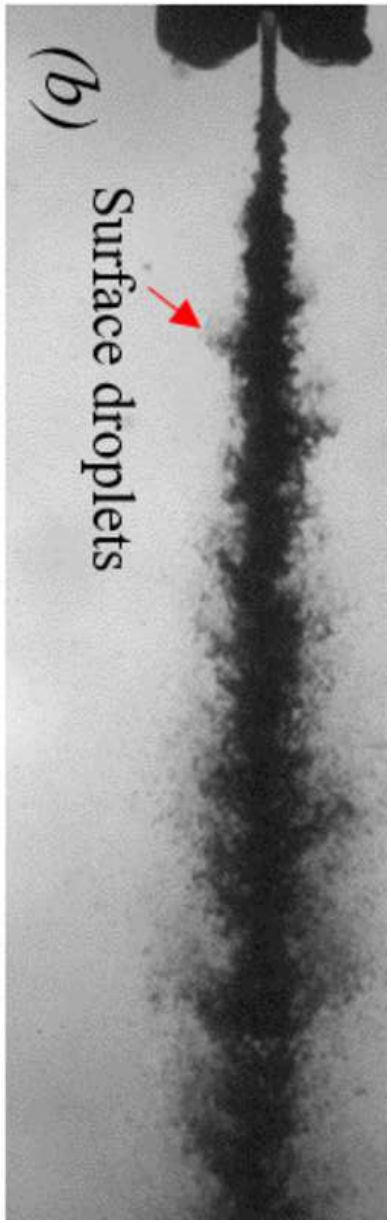

PLEASE CITE THIS ARTICLE AS DOI: 10.1063/5.0063049

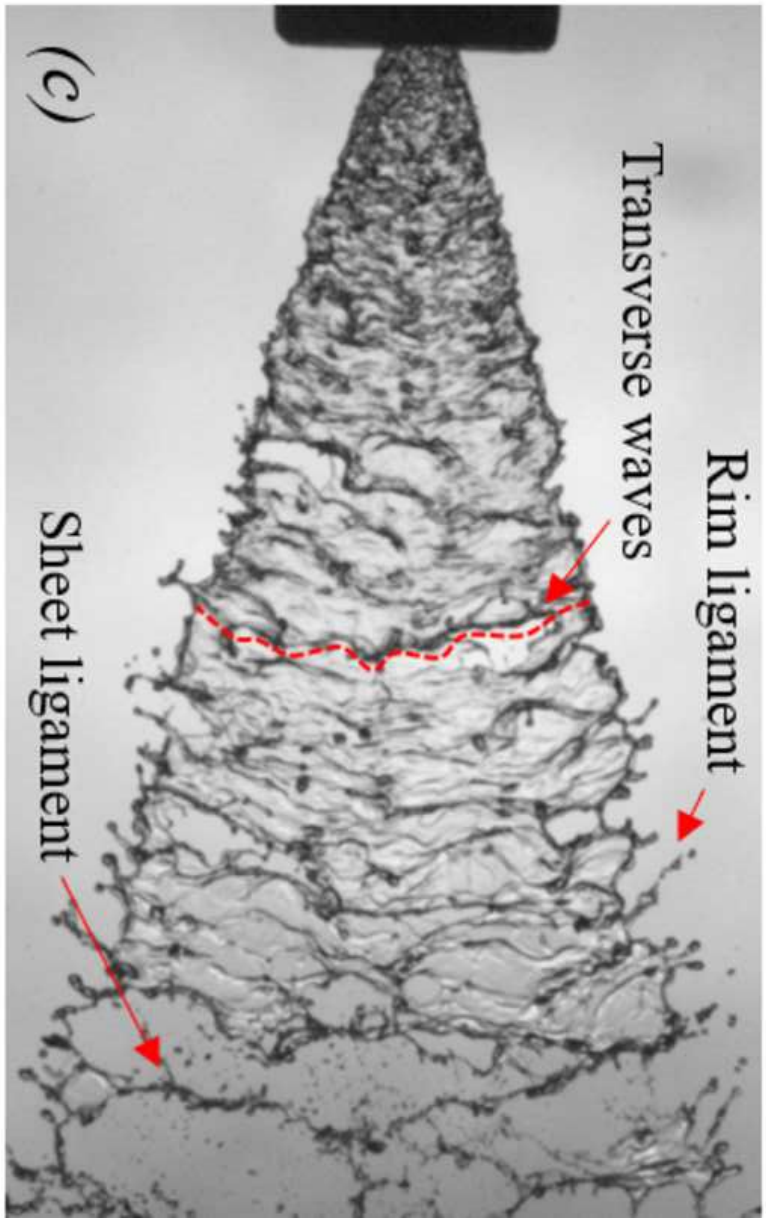

PLEASE CITE THIS ARTICLE AS DOI: 10.1063/5.0063049

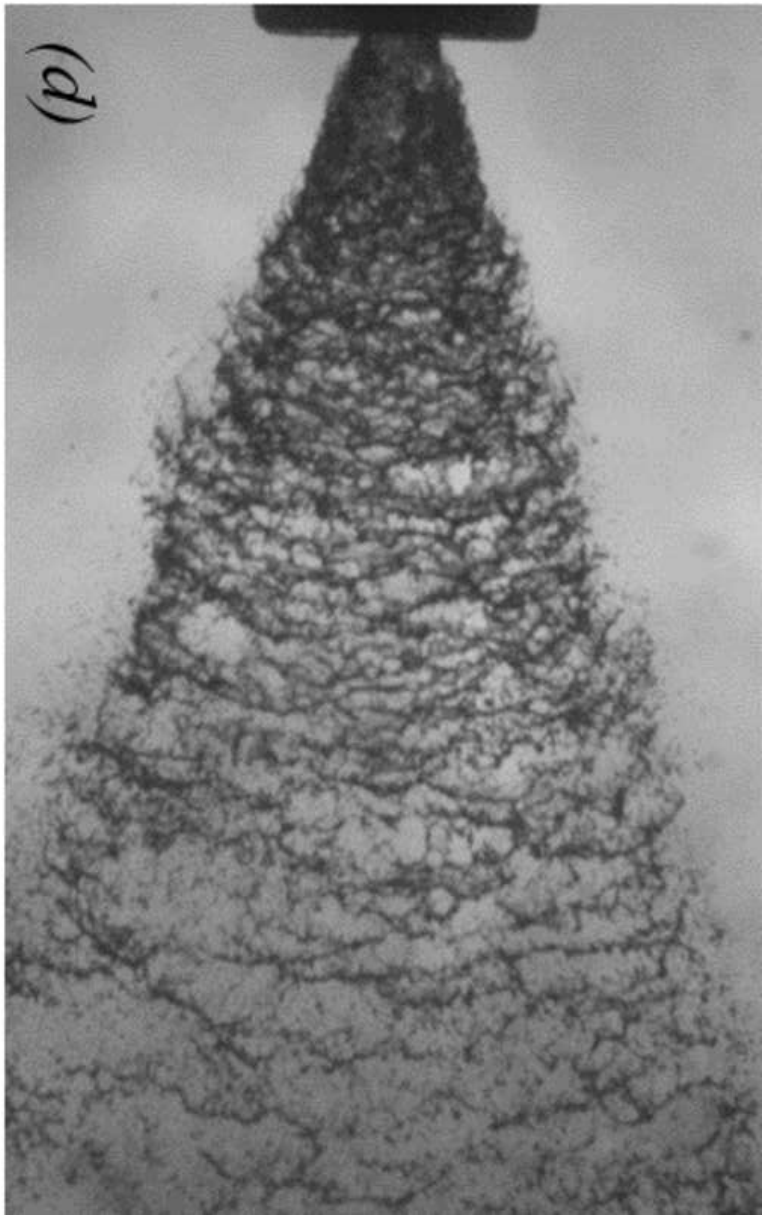

PLEASE CITE THIS ARTICLE AS DOI: 10.1063/5.0063049

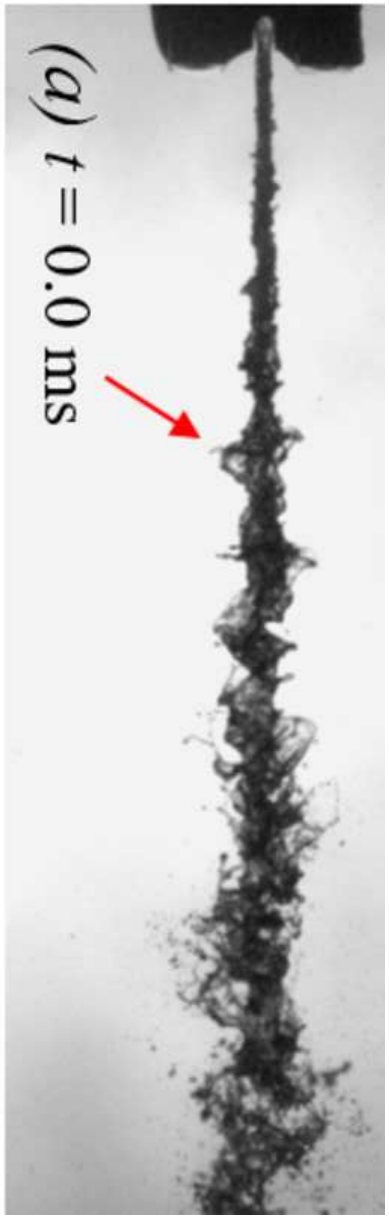

PLEASE CITE THIS ARTICLE AS DOI: 10.1063/5.0063049

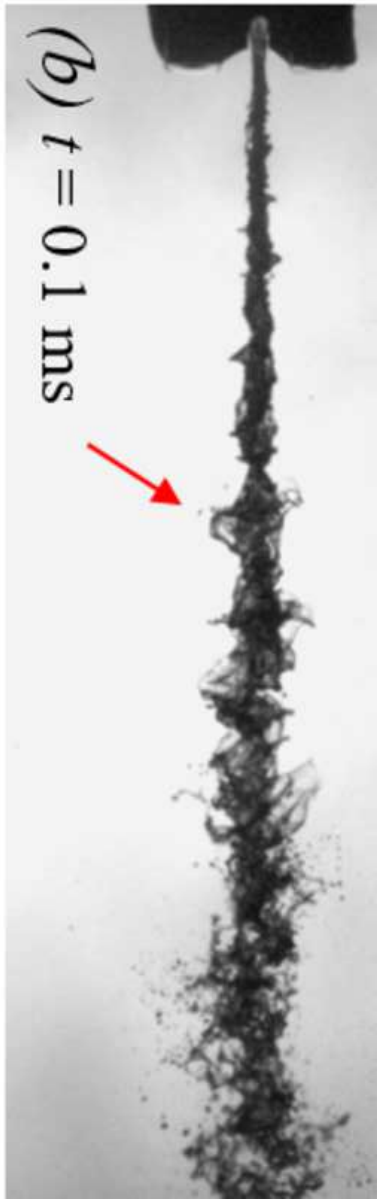

PLEASE CITE THIS ARTICLE AS DOI: 10.1063/5.0063049

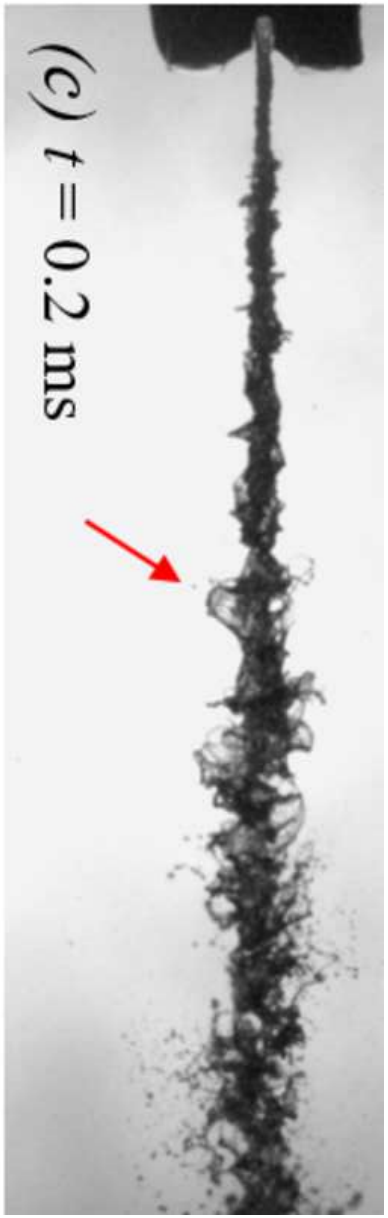

PLEASE CITE THIS ARTICLE AS DOI: 10.1063/5.0063049

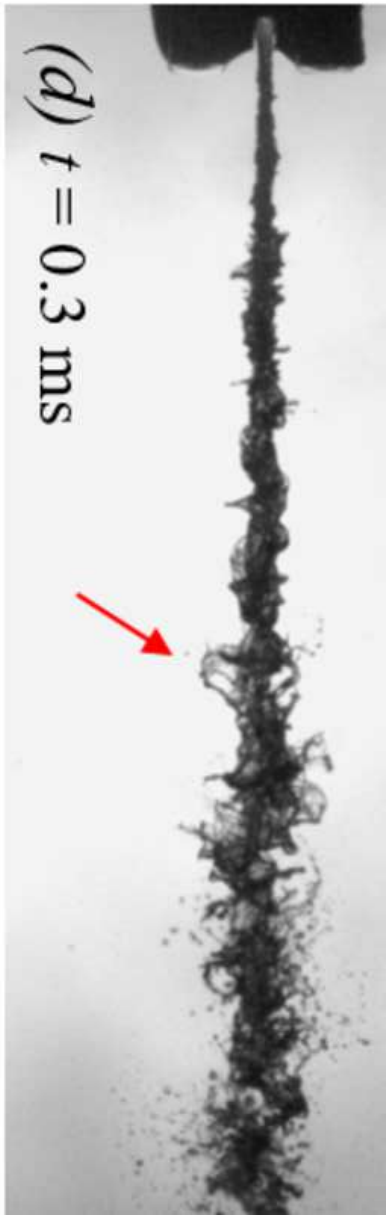

PLEASE CITE THIS ARTICLE AS DOI: 10.1063/5.0063049

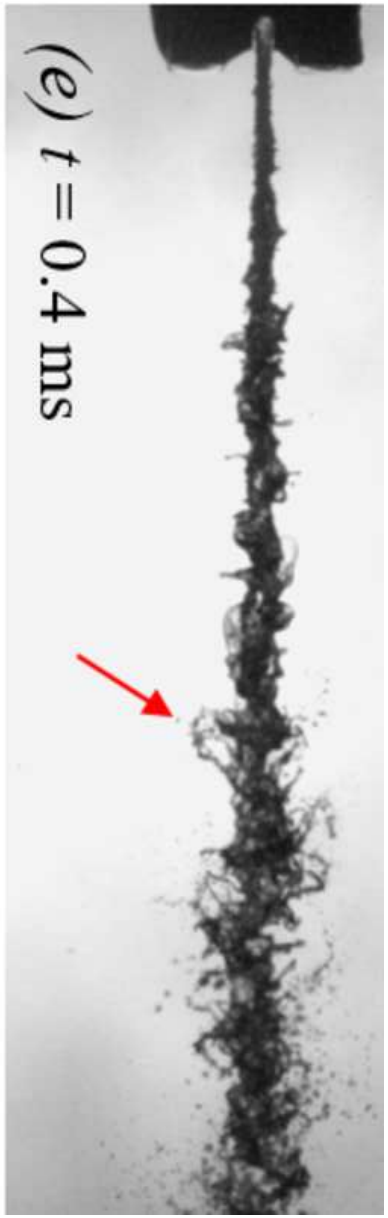

PLEASE CITE THIS ARTICLE AS DOI: 10.1063/5.0063049

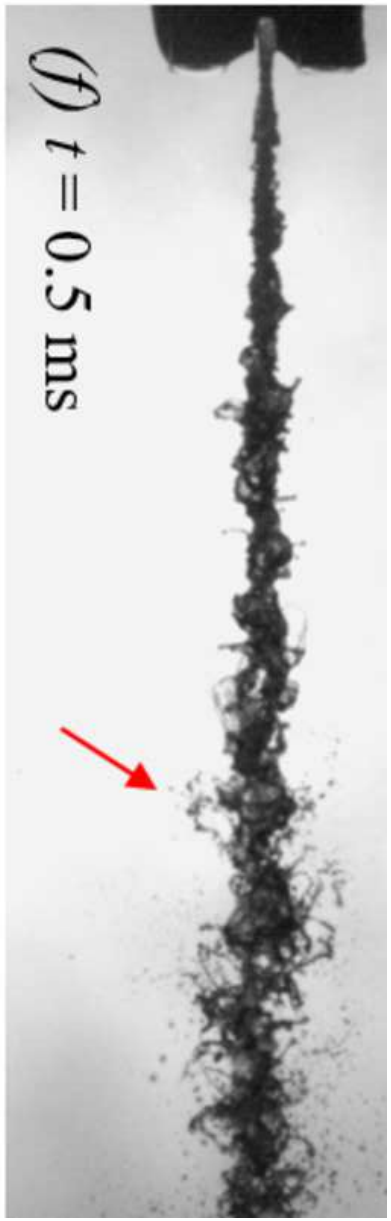

PLEASE CITE THIS ARTICLE AS DOI: 10.1063/5.0063049

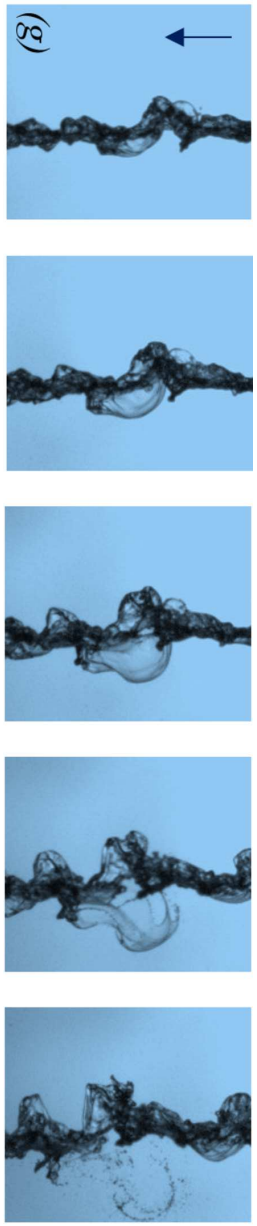

PLEASE CITE THIS ARTICLE AS DOI: 10.1063/5.0063049

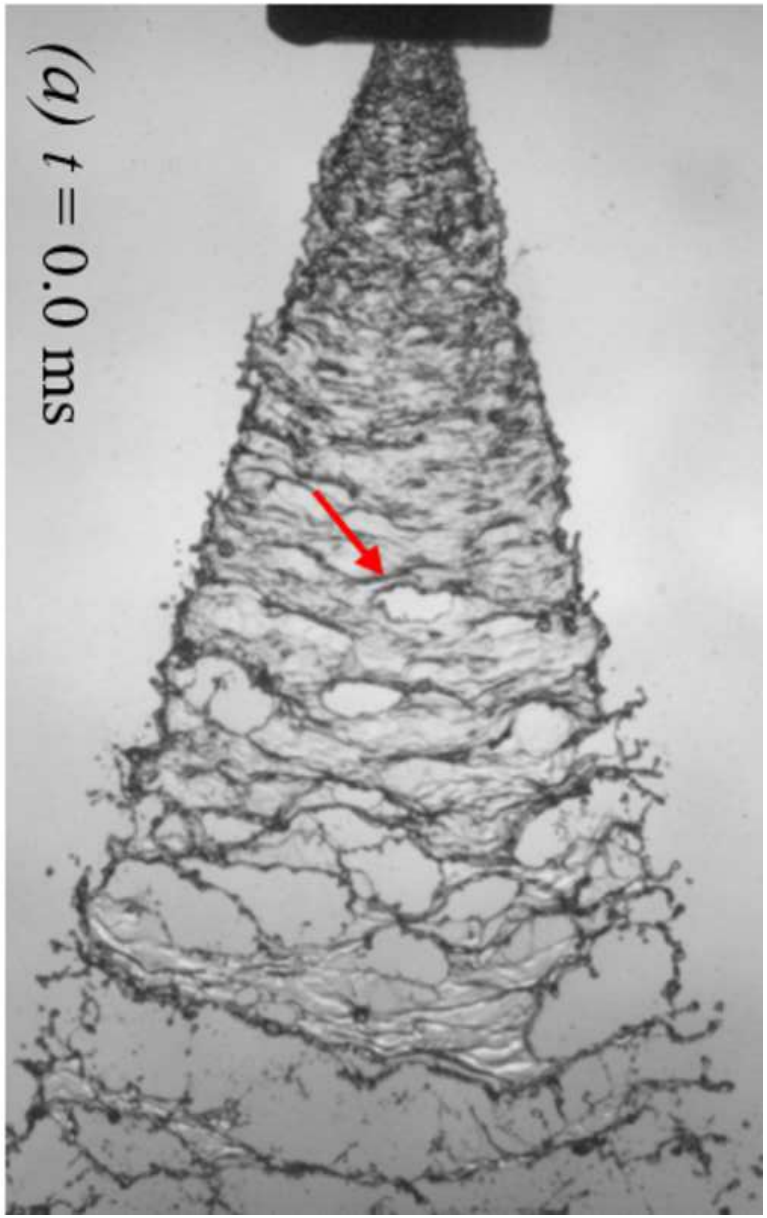

PLEASE CITE THIS ARTICLE AS DOI: 10.1063/5.0063049

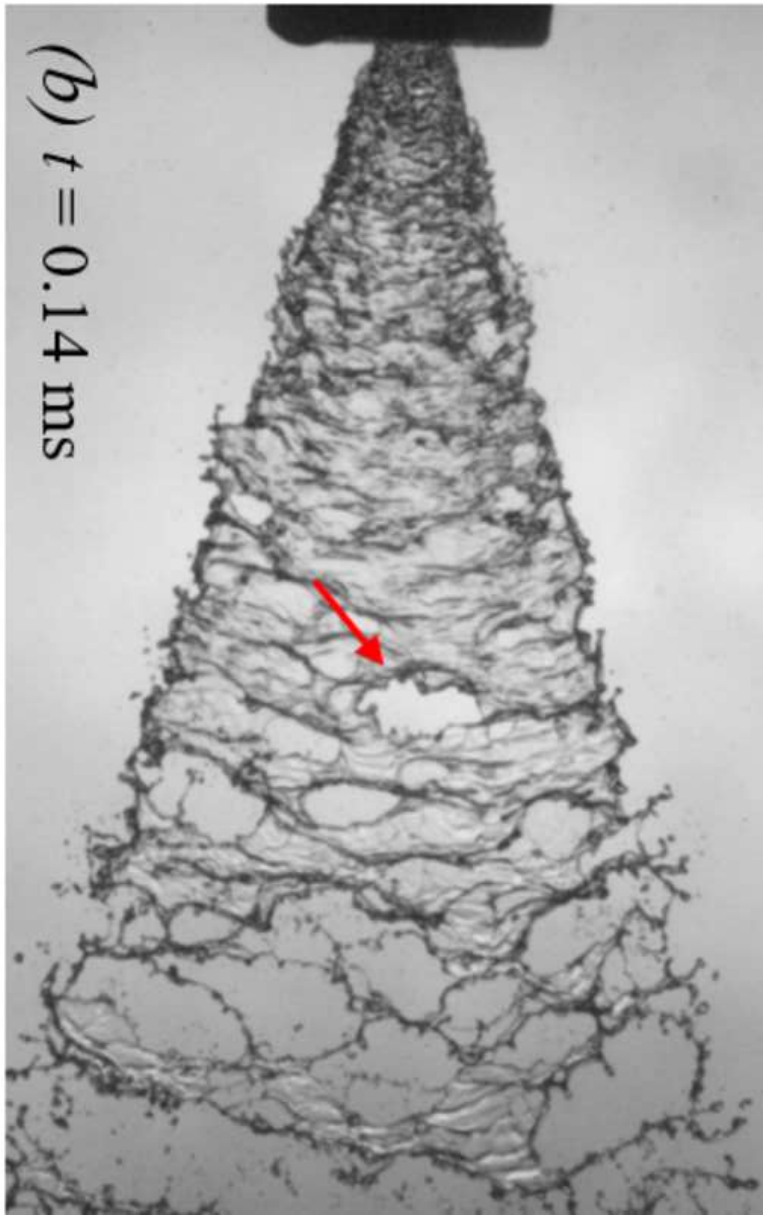

PLEASE CITE THIS ARTICLE AS DOI: 10.1063/5.0063049

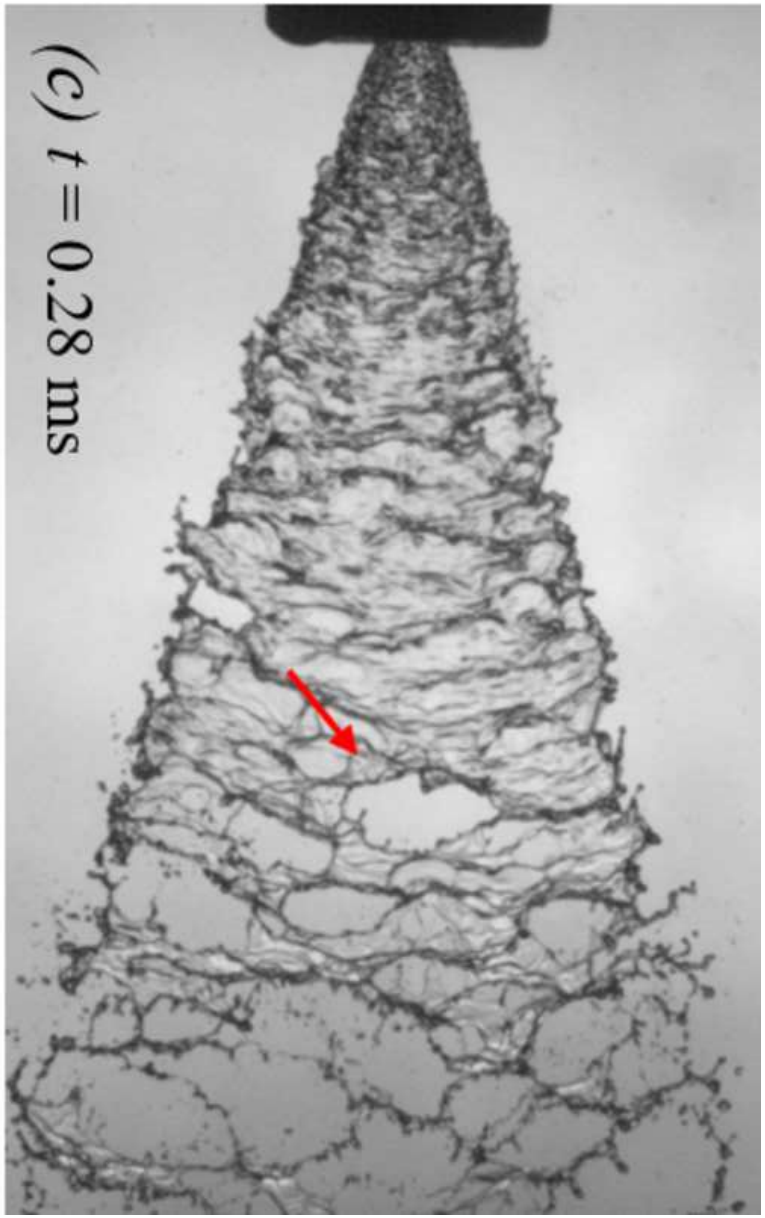

PLEASE CITE THIS ARTICLE AS DOI: 10.1063/5.0063049

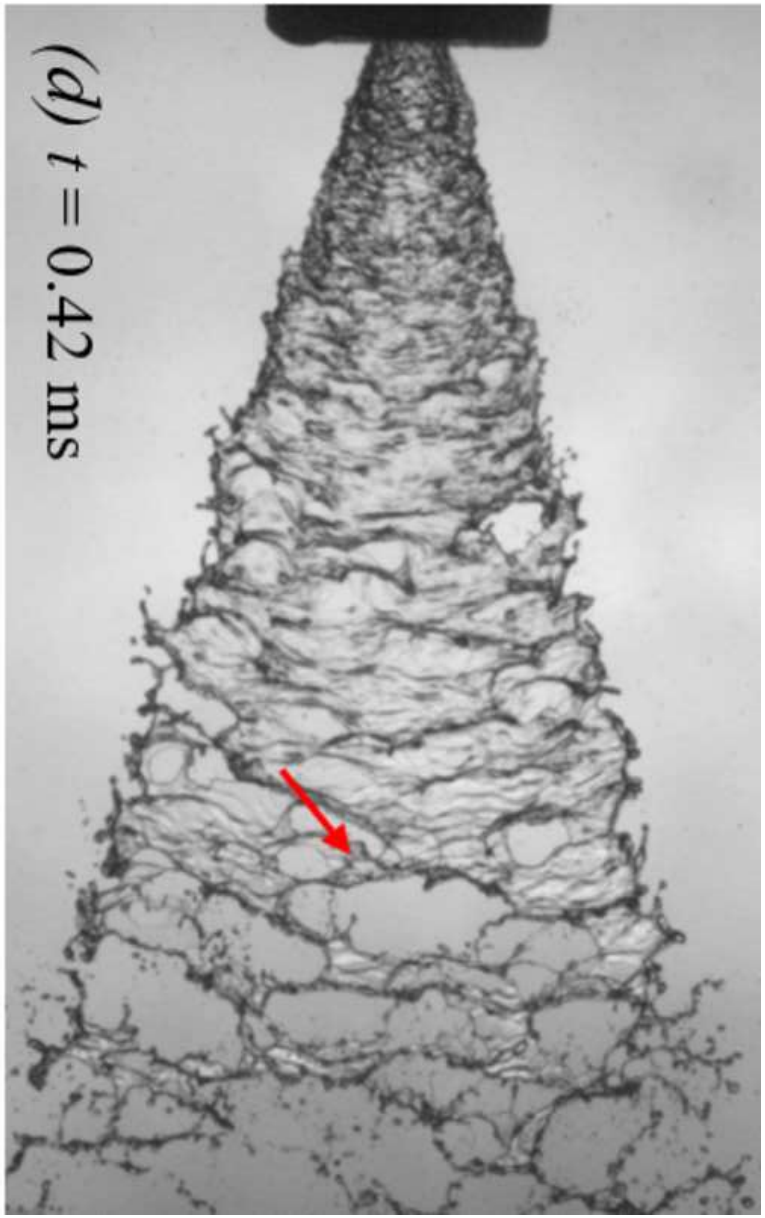

PLEASE CITE THIS ARTICLE AS DOI: 10.1063/5.0063049

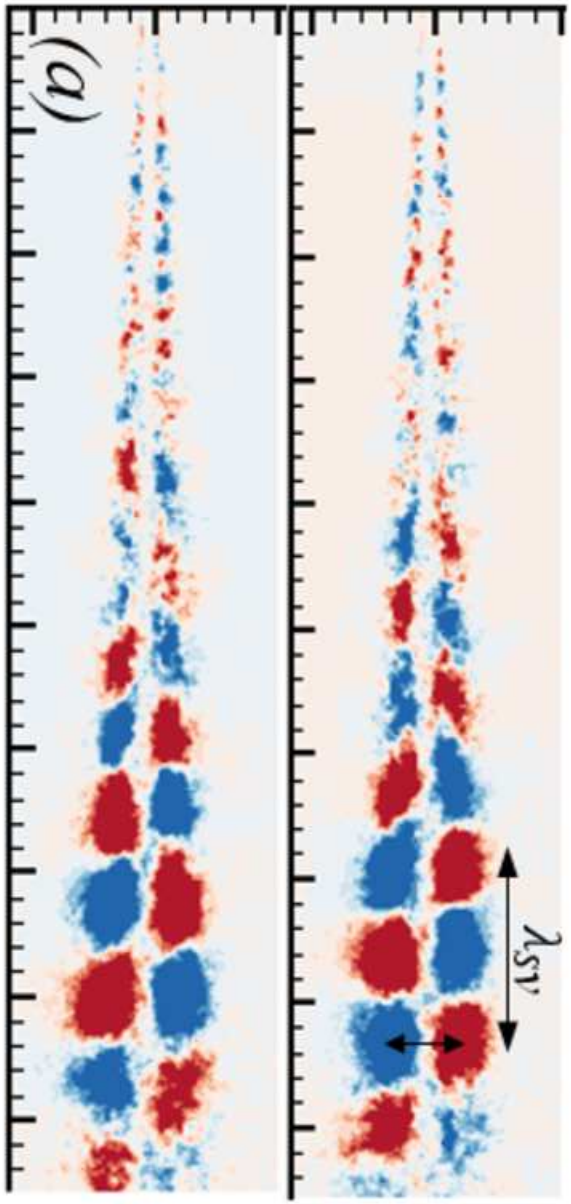

PLEASE CITE THIS ARTICLE AS DOI: 10.1063/5.0063049

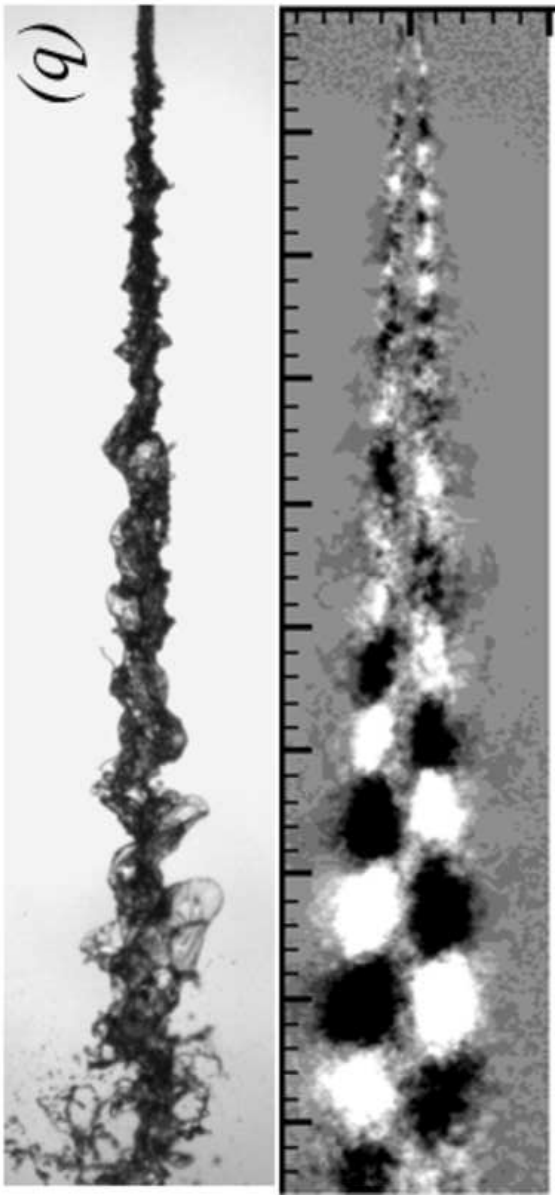

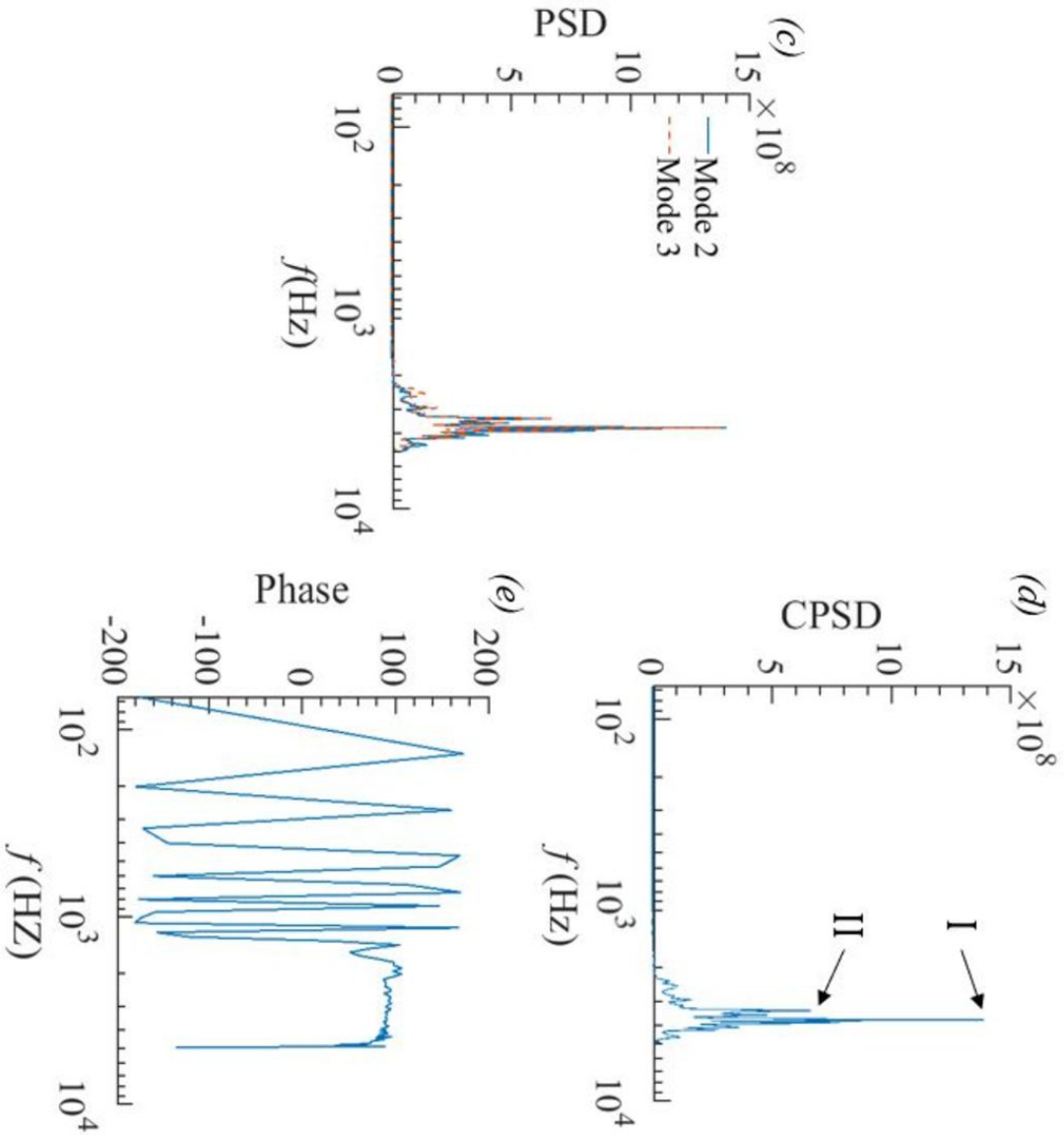

PLEASE CITE THIS ARTICLE AS DOI: 10.1063/5.0063049

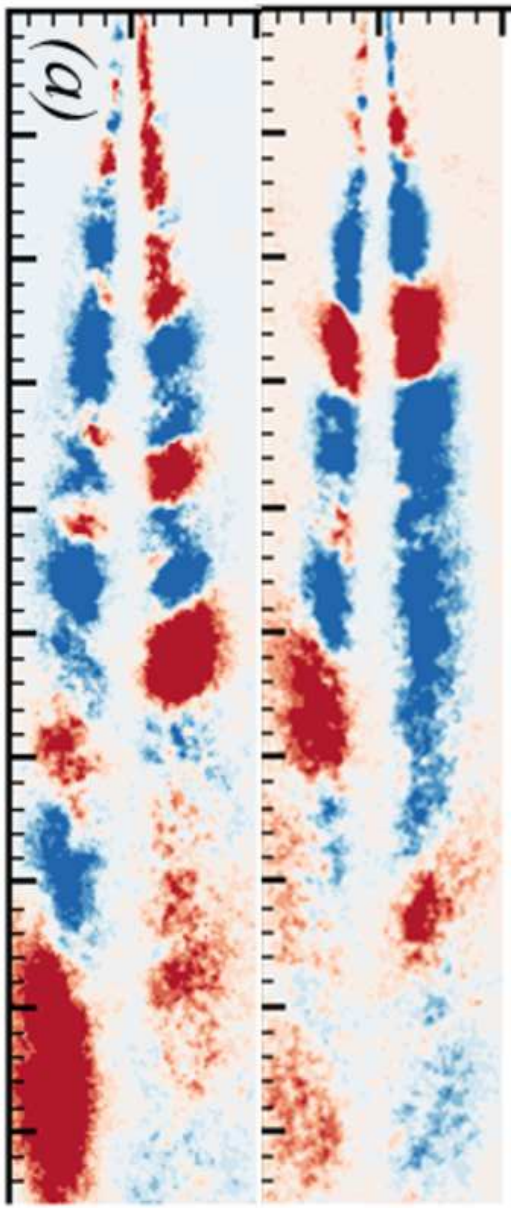

PLEASE CITE THIS ARTICLE AS DOI: 10.1063/5.0063049

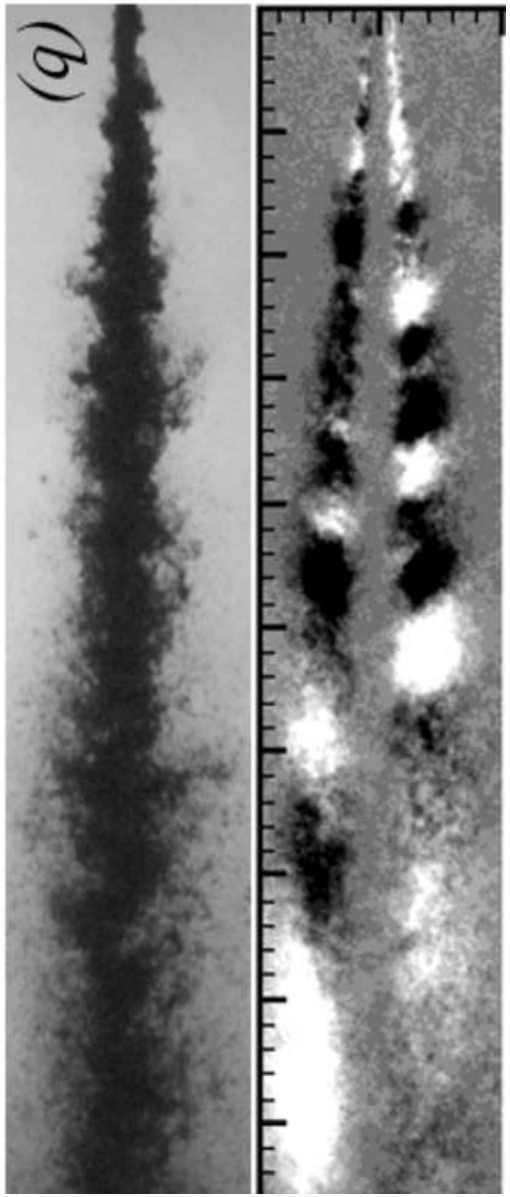

PLEASE CITE THIS ARTICLE AS DOI: 10.1063/5.0063049

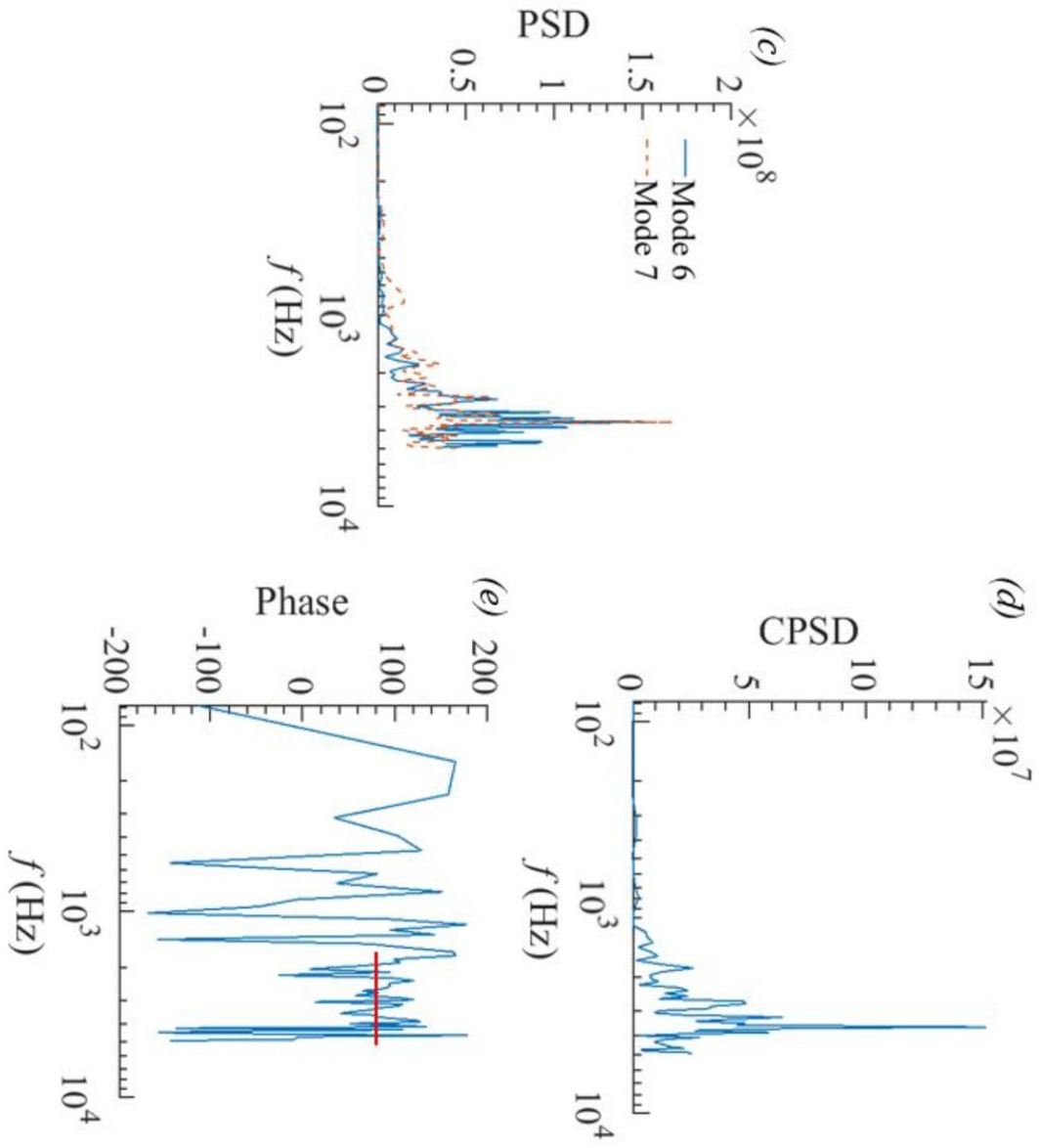

PLEASE CITE THIS ARTICLE AS DOI: 10.1063/5.0063049

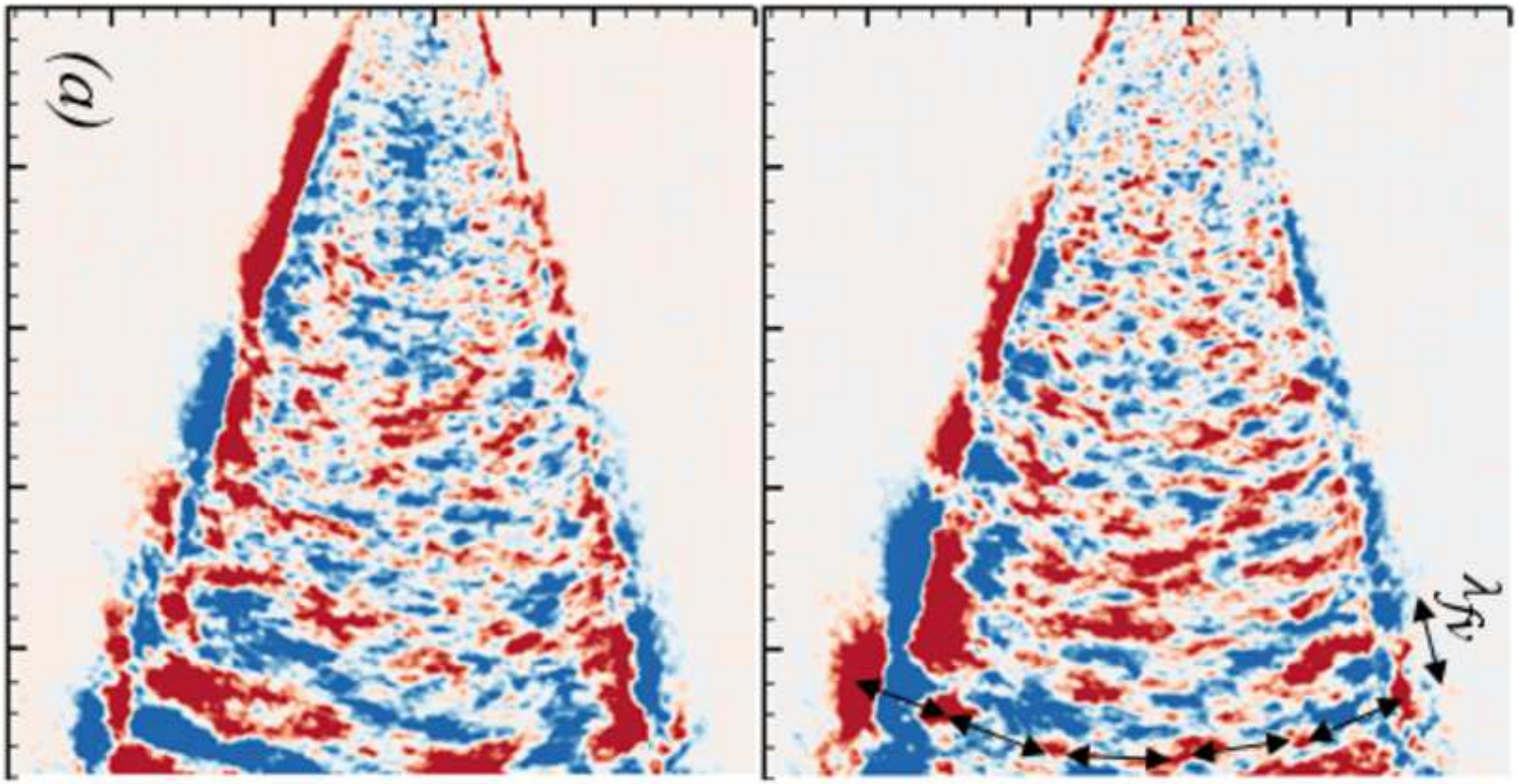

PLEASE CITE THIS ARTICLE AS DOI: 10.1063/5.0063049

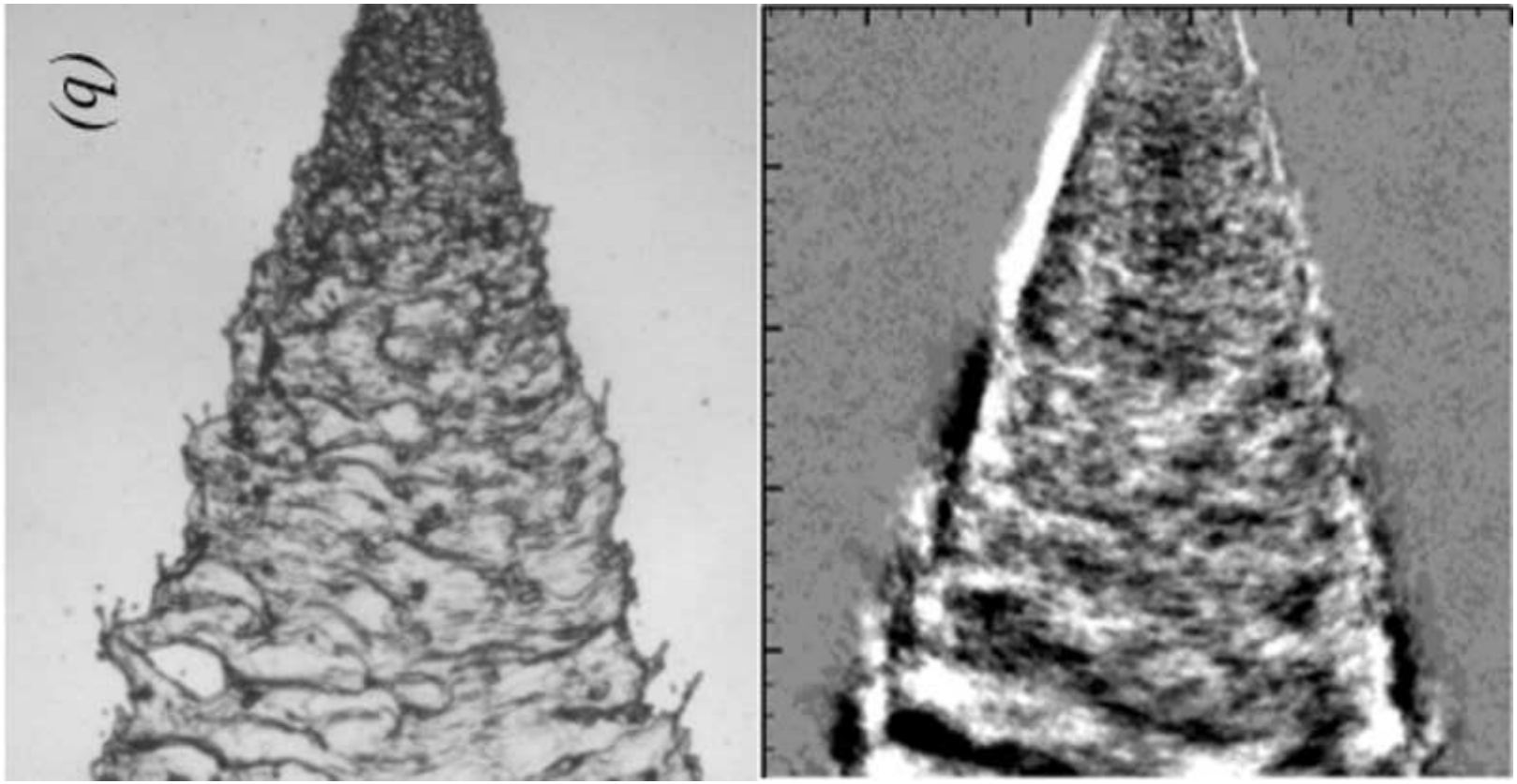

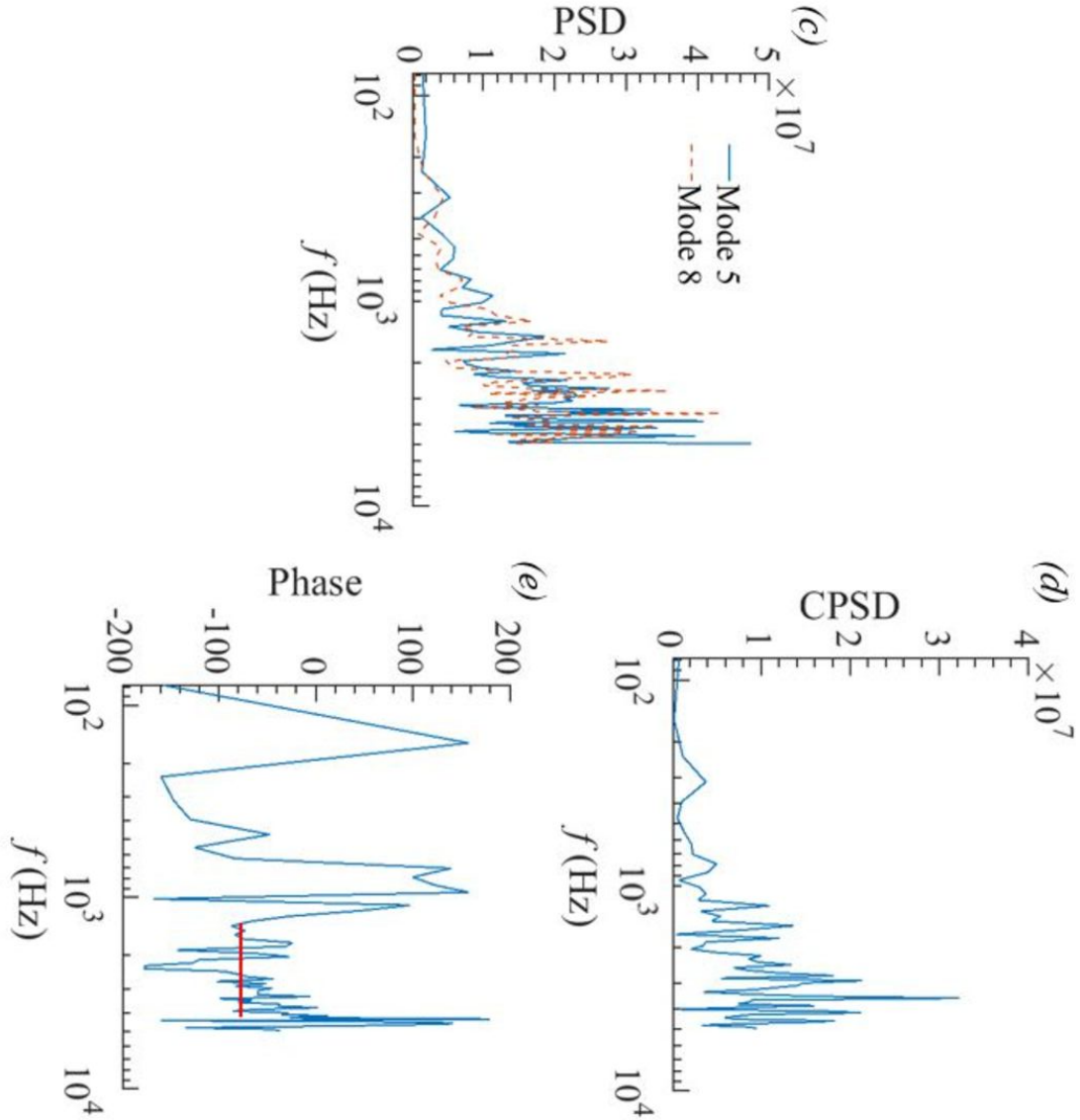

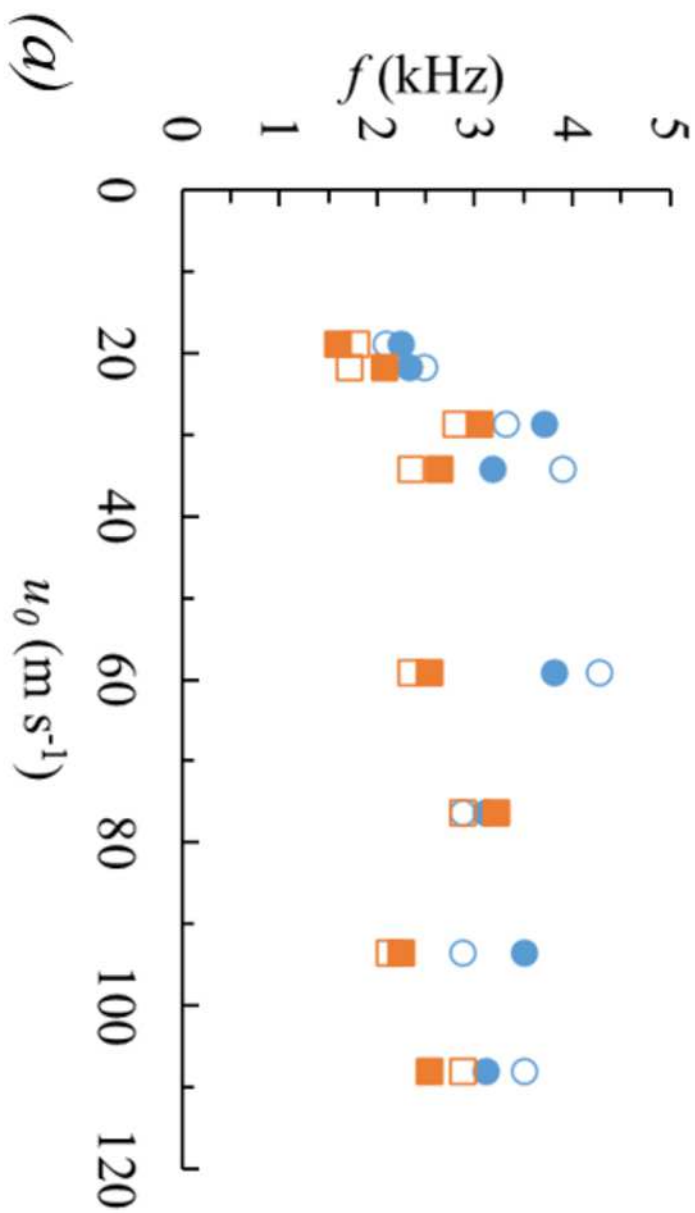

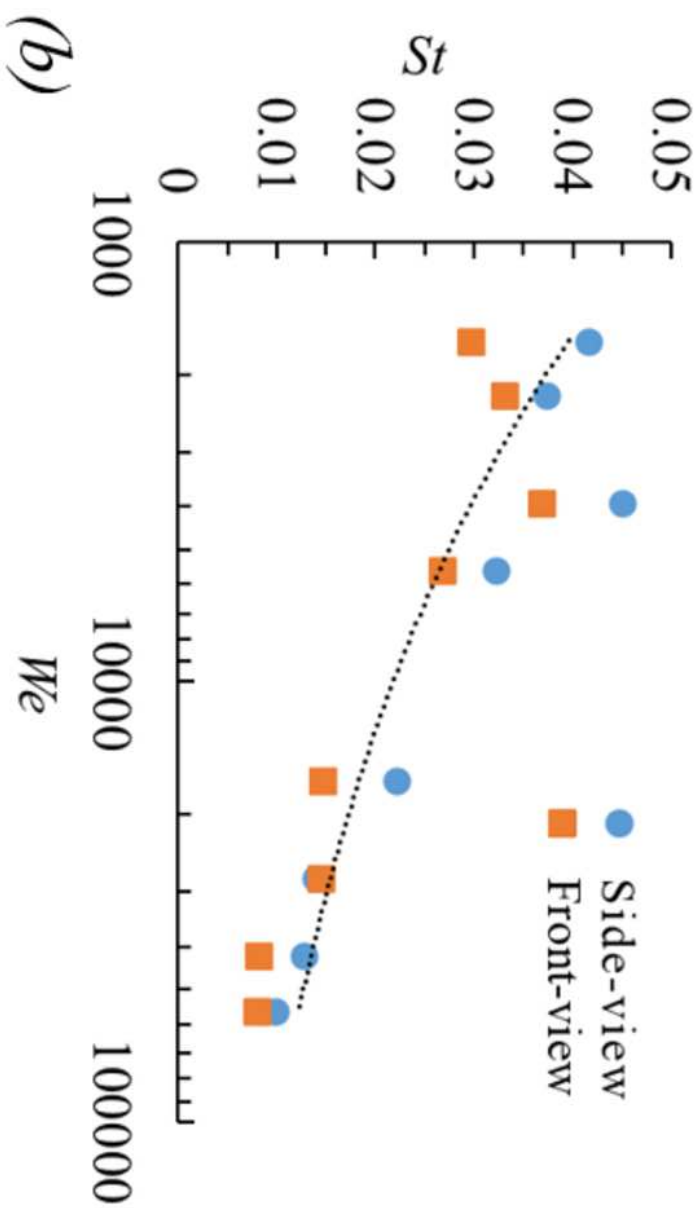

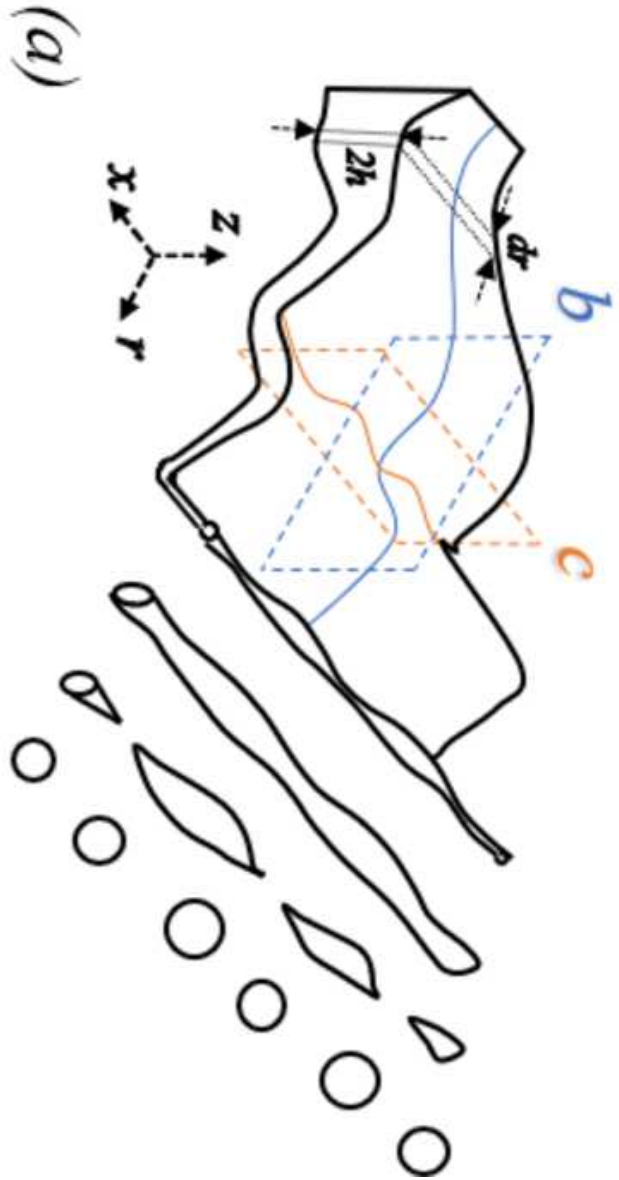

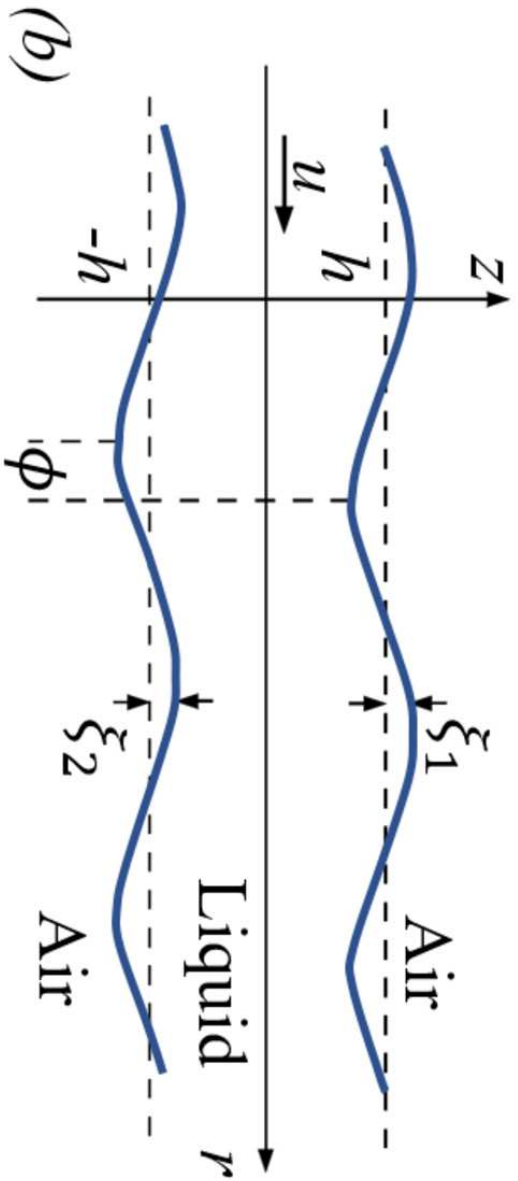

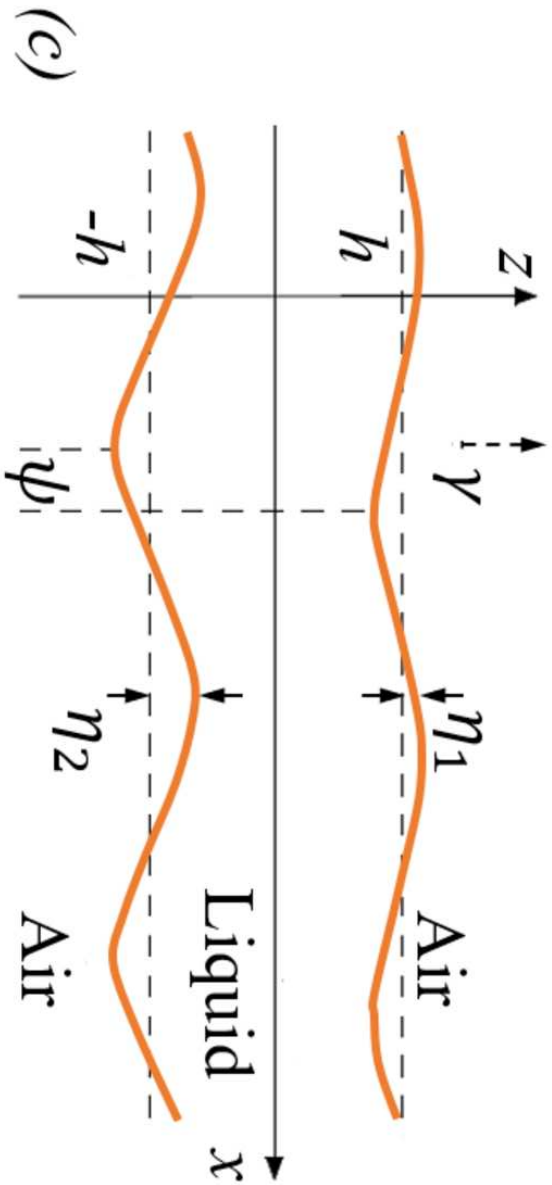

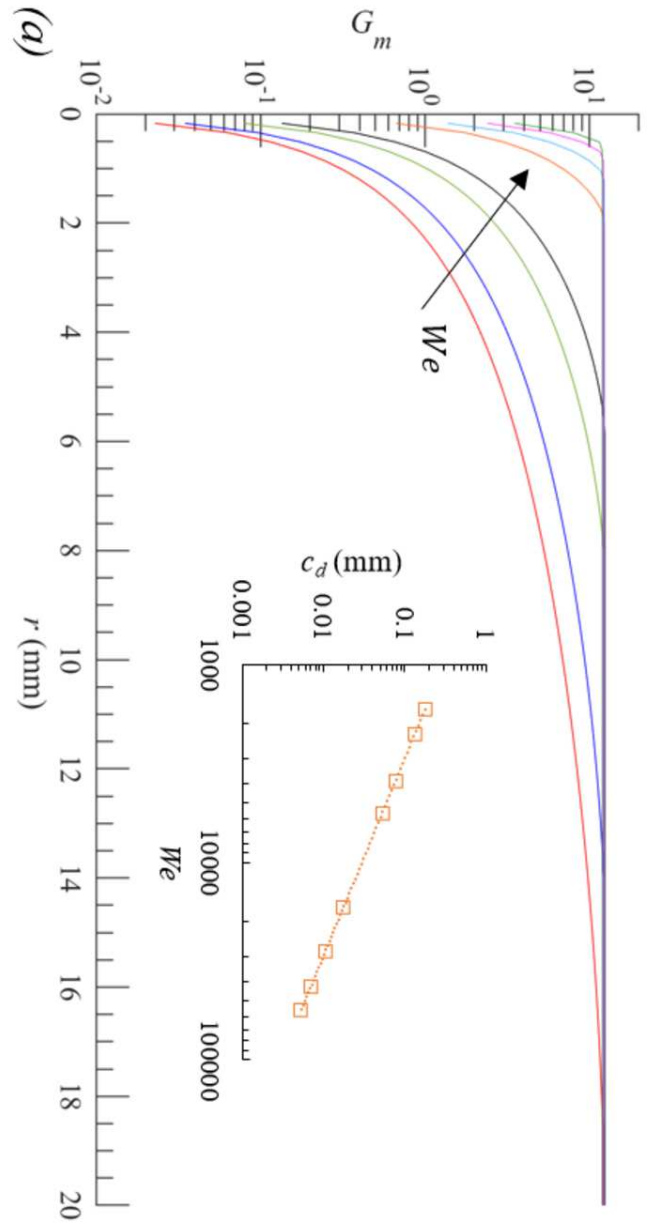

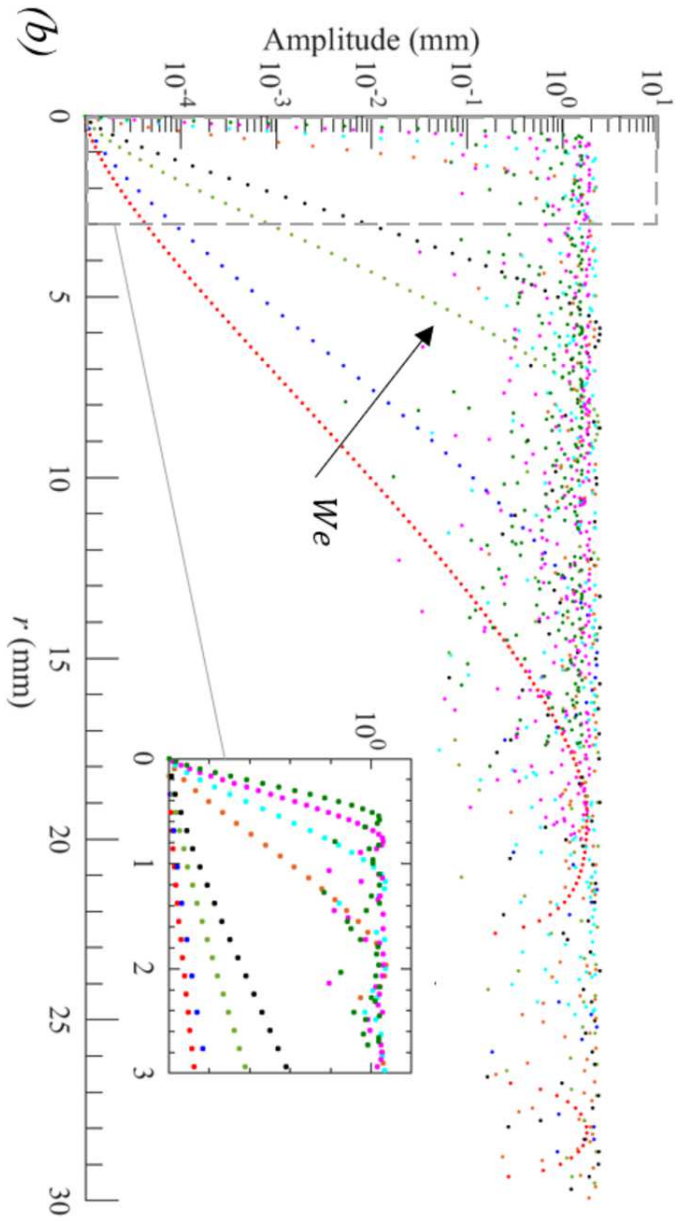

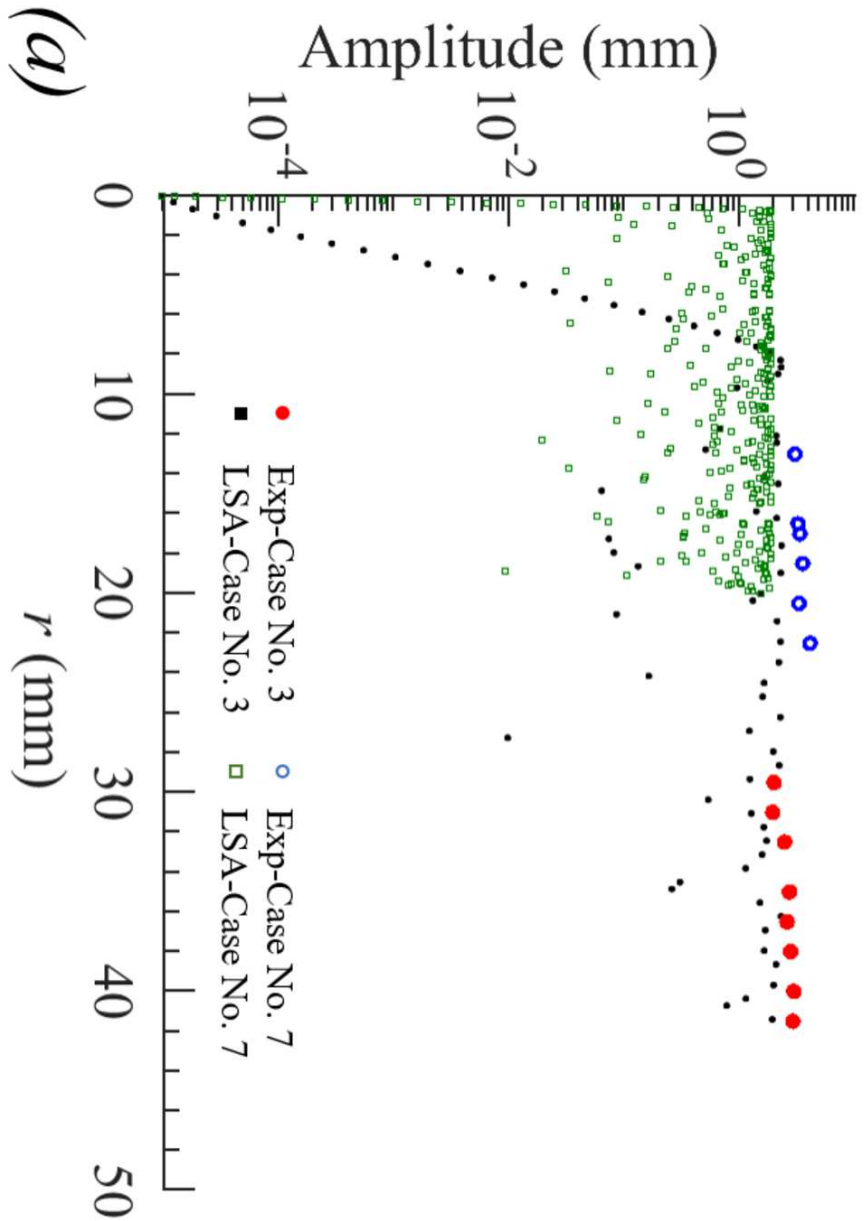

PLEASE CITE THIS ARTICLE AS DOI: 10.1063/5.0063049

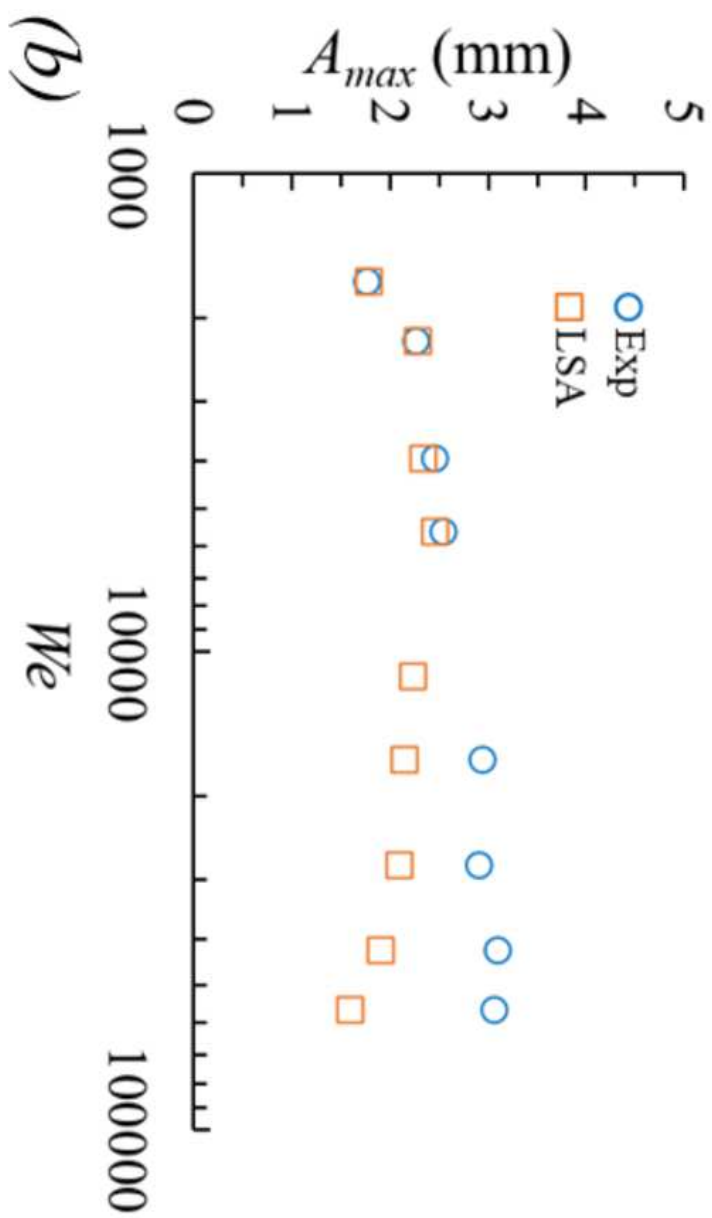

PLEASE CITE THIS ARTICLE AS DOI: 10.1063/5.0063049

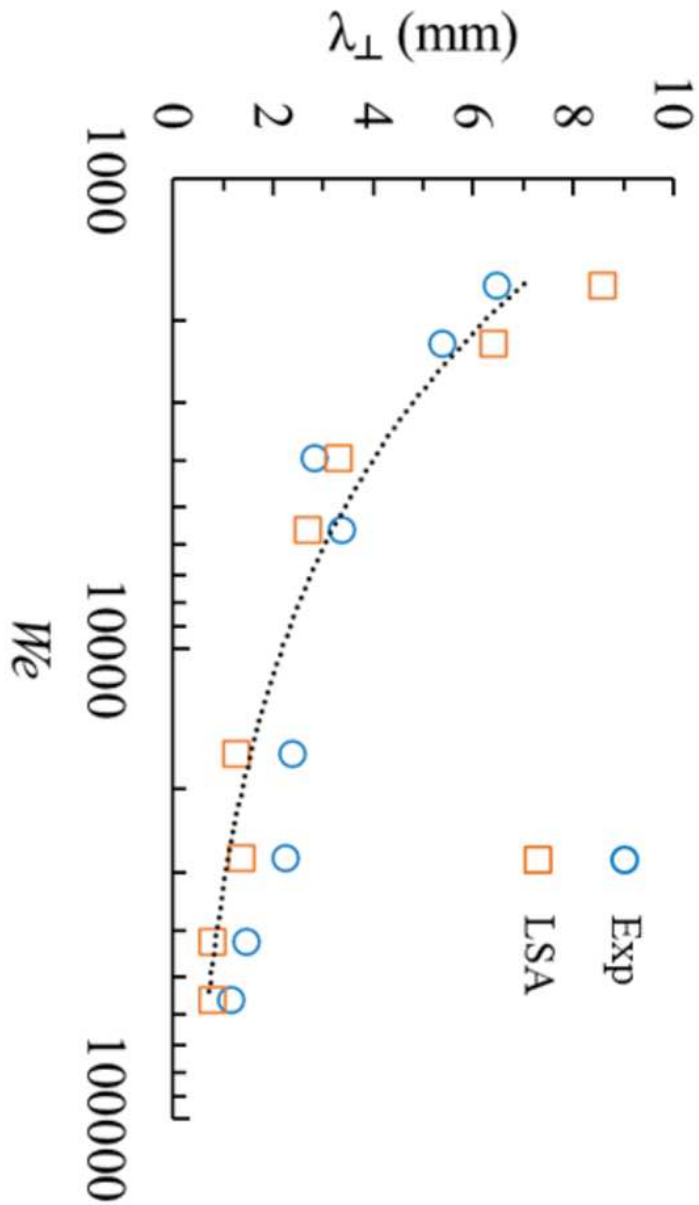

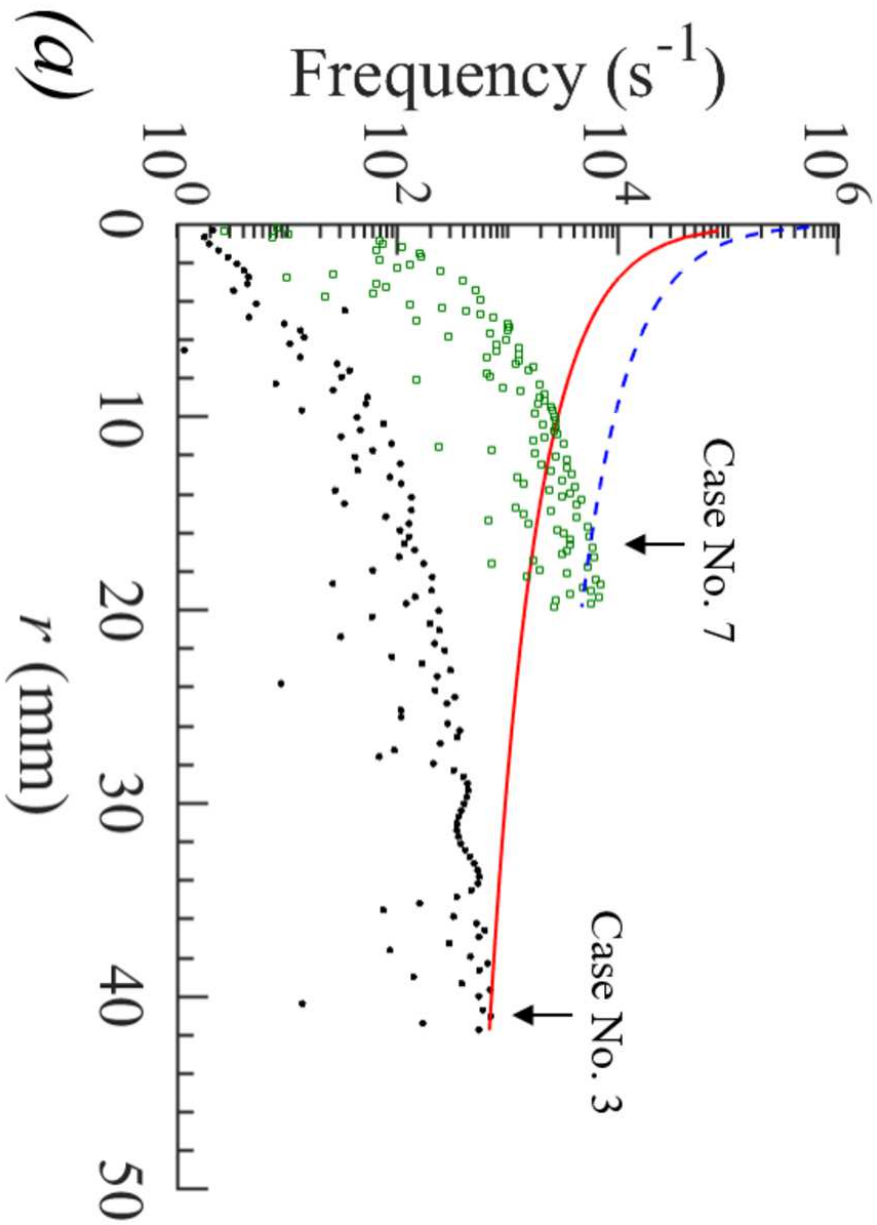

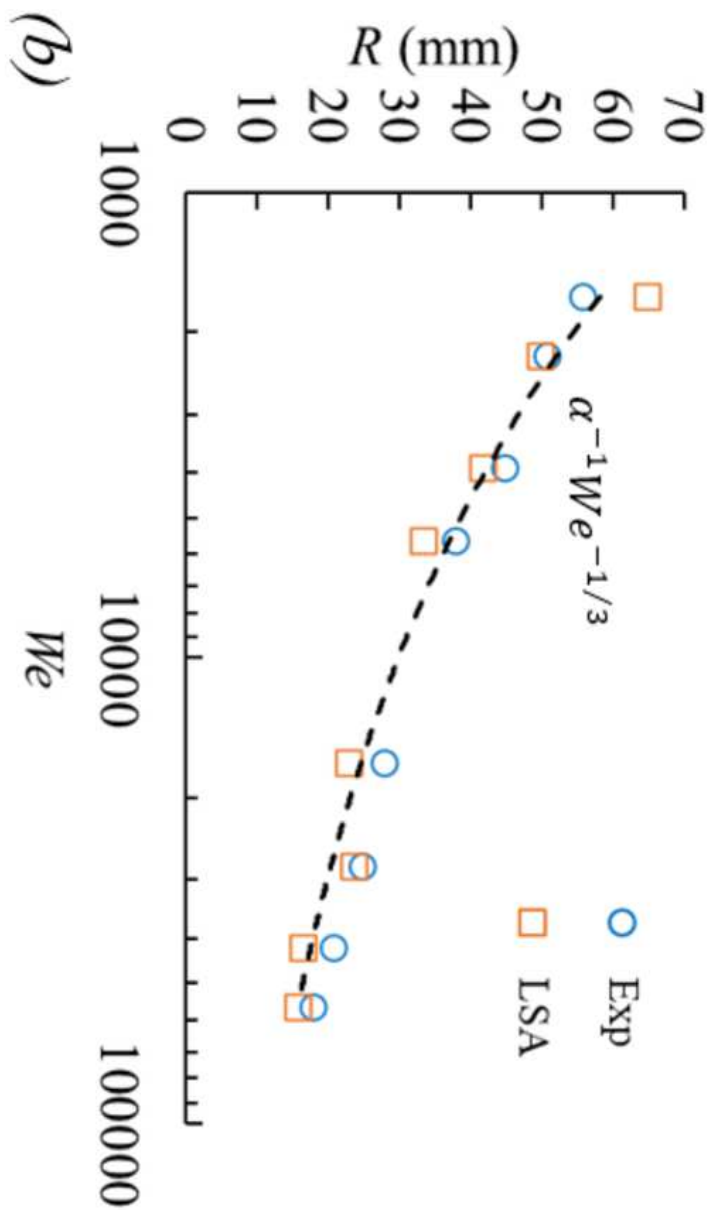

PLEASE CITE THIS ARTICLE AS DOI: 10.1063/5.0063049

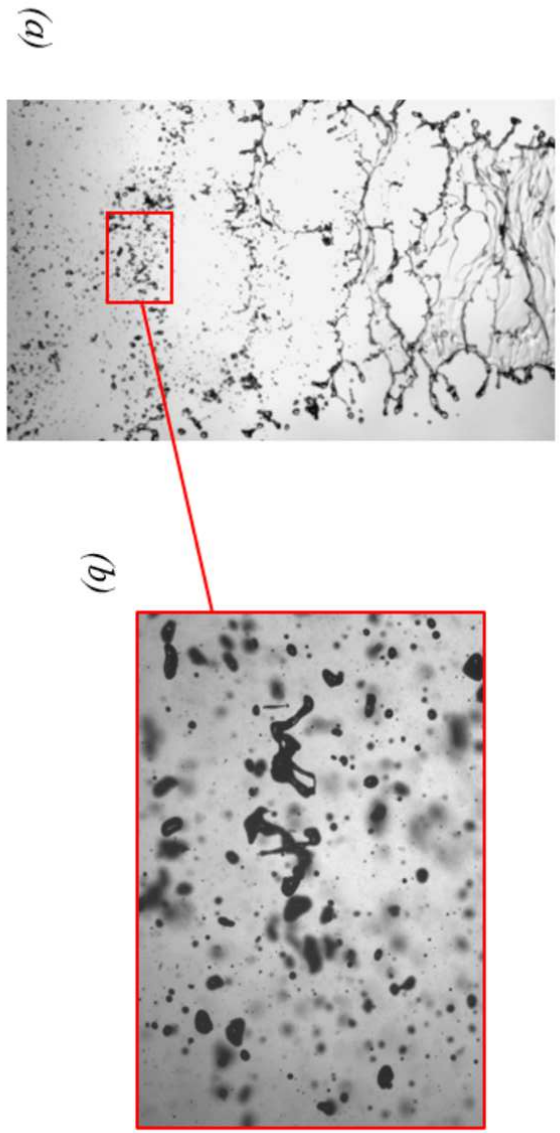

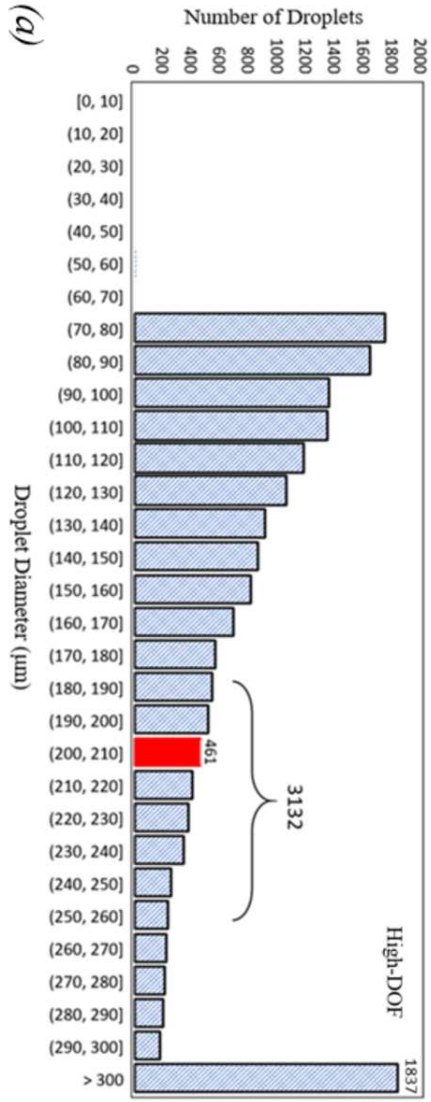

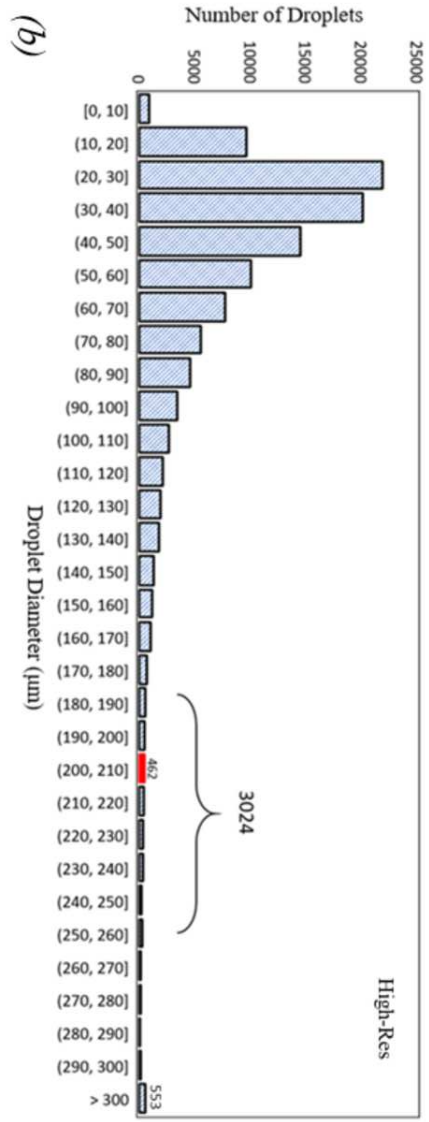

PLEASE CITE THIS ARTICLE AS DOI: 10.1063/5.0063049

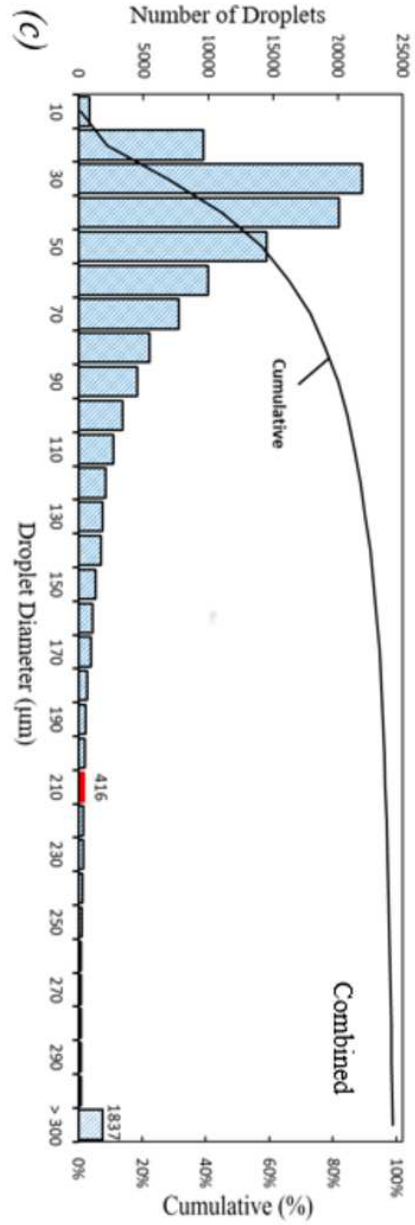

PLEASE CITE THIS ARTICLE AS DOI: 10.1063/5.0063049

(a)

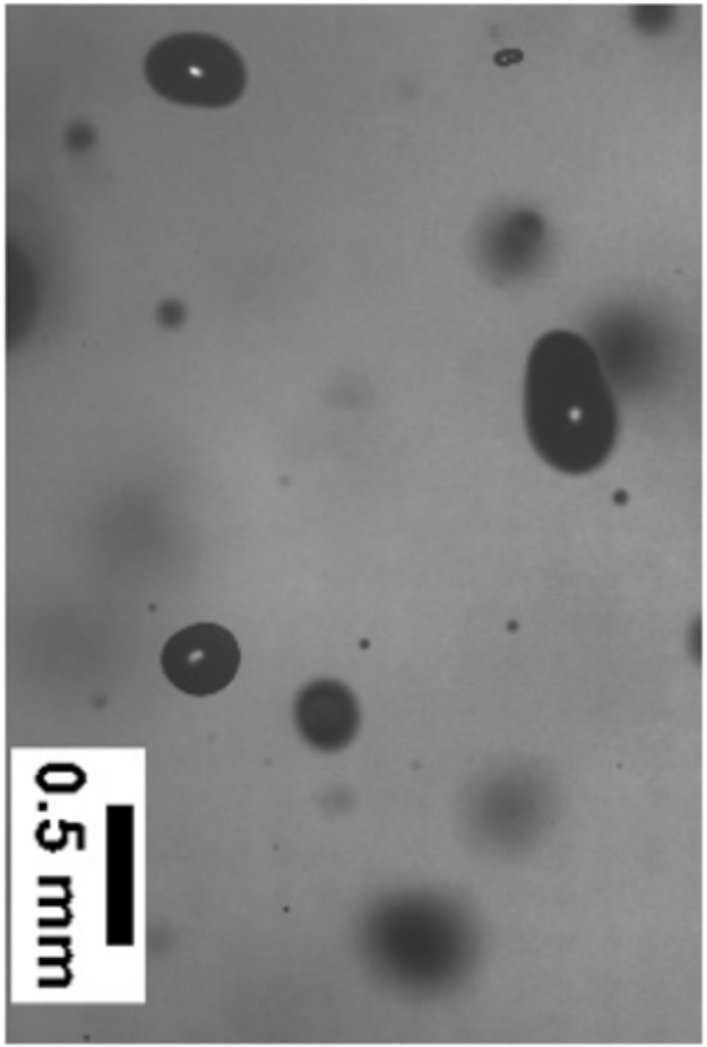

PLEASE CITE THIS ARTICLE AS DOI: 10.1063/5.0063049

(a)